UNIVERSITÀ DEGLI STUDI DI PADOVA

Dipartimento di Fisica e Astronomia "Galileo Galilei"
Master Degree in Physics

Quantum sensing in axion dark matter search

Thesis supervisor
Prof. Caterina Braggio

Candidate
Cesare Mattiroli

Thesis co-supervisor
Dr. Antonello Ortolan

Academic Year 2021/2022

Abstract

Cosmological evidence shows the presence in the universe of more mass than what can be inferred from luminosity measurements. This excess of mass, known as Dark Matter (DM), forms halos around the galaxies. It is still unknown what DM is made of. Axions are hypothetical particles among leading DM candidates. Experimental axion search requires detectors at the ultimate level of sensitivity allowed by quantum mechanics. Haloscopes are detectors employed in axion search made of a resonant cavity immersed in a strong magnetic field. With today's leading technology based on quantum-limited linear amplifiers, the sensitivity is fundamentally limited by vacuum fluctuations of the cavity field and it may take centuries to probe the most plausible parameter space. Such quantum limits can be overcome if microwave photon counting is adopted. The microwave domain detection of individual photons is a challenging task because the photon energy is roughly five orders of magnitude lower than at optical frequencies. Very recently a practical single microwave photon detectors have been introduced in the field of quantum information science. The low dark count rate, tunability, and the continuous operation of this device will be exploited to demonstrate a quantum-enhanced search of axions at the QUAX haloscope.

Contents

Acronyms

ADC Analog to Digital Converter. 33

AWG Arbitrary Waveform Generator. 53, 64

BCS Bardeen–Cooper–Schrieffer. 9

CMB Cosmic Microwave Background. 5

CPW Coplanar Waweguide. 2, 12

cQED circutit Quantum Electrodynamics. 7

DFSZ Dine-Fischler-Srednicki-Zhitnitsky. 6

DM Dark Matter. 1, 5

EDM Electric Dipole Moment. 6

FPGA Field Programmable Gate Array. 53

FPR False Positive Rate. 36

HEMT Hig Electron Mobility Transistor. 39

JPA Josephson Parametric Amplifier. 38

KSVZ Kim-Shifman-Vainshtein-Zakharov. 6

LHe Liquid Helium. 20

LNL Laboratori Nazionali di Legnaro. 22

LO Local Oscillator. 33, 64

pdf probability density function. 60

ROC Receiver Operating Characteristic. 36

SA Spectrum Analyzer. 41, 53, 54, 64

SMPD Single Microwave Photon Detector. 7, 35

SNR Signal to Noise Ratio. 34

SNSPD Superconducting Nanowire Single Photon Detector. 49

SPAD Single-Photon Avalanche Diode. 49

SQL Standard Quantum Limit. 3, 7, 33, 74

SQUID Superconducting Quantum Interference Device. 2, 14, 54

TPR True Positive Rate. 36

TWPA Traveling Wave Parametric Amplifiers. 38

VNA Vector Network Analyzer. 18

1 Introduction

1.1 Dark Matter and Axions

Many cosmological observations points to the presence in the universe of more mass than the one that can be inferred by visible matter. This excess mass is called DM. The most accurate prediction of its abundance obtained from the study of the small Cosmic Microwave Background (CMB) anisotropies, where by DM accounts for 26% of the universe energy density while ordinary matter only for 6%. The remaining 68% is made of what is called vacuum energy[1].
One of the proofs of DM existence comes from is the study of galactic rotation curves which consists in studying stars velocity as a function of the distance r from the center of their galaxy. In a spiral galaxy, the visible mass distribution would imply that at the galaxy periphery stars velocity should decrease as $1/\sqrt{r}$ whereas the experimental curve measured for many galaxies shows a flat behavior at a large distance from the center (Figure 1). This behavior is explained by the presence of dark matter spherical halo around galaxies. The average density of the Milky Way halo measured in a portion of the galaxy that contains the solar system is around 0.45 GeV/cm^3.

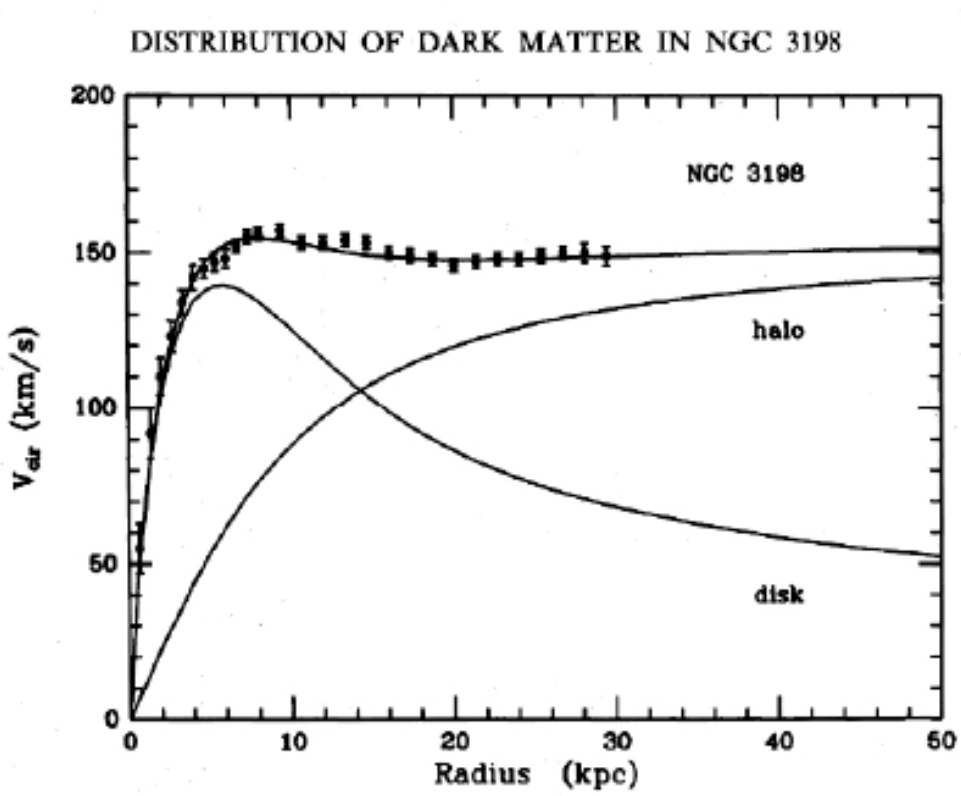

Figure 1: Rotation curve for the NGC 3198 galaxy

Despite strong evidences of its presence,the nature of dark matter in unknown, as indicated by the fact that plausible dark matter particle candidates have masses that span over more than 30 orders of magnitude. The properties that can be inferred from cosmological observations suggest that dark matter candidates should be searched outside the Standard Model of Particle Physics.
One of the major hypotheses was that dark matter is made up of weakly interacting massive particles (WIMPs). In the last 30 years, WIMPs have been extensively searched in collider experiments and underground detectors that excluded their presence in a vast portion of the parameter space. Following to these results, the research interest has now shifted towards lighter candidates with sub-eV mass. Axions are one of the best examples of such light DM candidates. They are the Nambu-Goldstone boson associated with the spontaneous break of the Peccei-Quinn symmetry which was theorized as a

solution to the strong CP problem, i.e. the fact that charge-parity symmetry violations do not appear in strong nuclear interaction. The axion models can be grouped into two main categories, the Kim-Shifman-Vainshtein-Zakharov (KSVZ) and the Dine-Fischler-Srednicki-Zhitnitsky (DFSZ)
For these light DM candidates the wave-like behavior prevails, so experiments that are searching for them do not look for single scattering events but for the presence of some background field. The axion interacts very weakly with the particles in the Standard Model. These interactions can be described with the non-relativistic Hamiltonian [1]

$$\hat{H} = \sqrt{\frac{\epsilon_0}{\mu_0}} g_{a\gamma\gamma} \int a\mathbf{E} \cdot \mathbf{B} dV + g_{aff} \hbar c \nabla a \cdot \hat{\mathbf{S}} + \sqrt{\epsilon_0 (\hbar c)^3} g_{EDM} a \hat{\mathbf{S}} \cdot \mathbf{E} \tag{1.1}$$

where the axion field a is measured in energy units , $g_{a\gamma\gamma}$ is the axion's coupling to photons measured in units of inverse energy, g_{aff} is the axion's coupling to fermionic matter particles, g_{EDM} is the strength of a nuclear Electric Dipole Moment (EDM) induced by the axion, $\mathbf{E}$ and $\mathbf{B}$ are the electric and magnetic fields, $\hat{\mathbf{S}}$ is the direction of the spin of the matter particle in question. Running experiments rely on the axion-photon interaction described by the first term.

1.2 Experimental axion search

The first challenge in experimental axion search is that any axion-related signal would be very small due to the weakness of the interaction. The second challenging aspect is the fact that theoretical models do not give a prediction of the axion mass and the most plausible range spans over several orders of magnitude as shown in Figure 2. For this reason, different technologies are required to cover the whole range and one of the most crucial figures of merit of an axion detector is its scan rate, i.e. the velocity at which it can probe the axion parameter space at a given sensitivity.
Several experiment are searching for axion exploiting the interaction with the electromagnetic (EM) fields. The working principle is based on the conversion of axions into photons in the presence of a magnetic field [2]. The photon energy approximately corresponds to the axion rest energy so the photon frequency is related to the axion mass $h\nu = m_a c^2$. Haloscopes are detectors that have provided the most sensitive searches for axions in our galactic halo. They are suited to explore the frequency range from a few hundreds MHz to several GHz. They are made of a resonant cavity immersed in a strong magnetic field. When the cavity frequency matches the axion mass an increase in the cavity photons population is expected. This would give a slight increase in the noise measured at the cavity output. To detect such a small increase other noise sources such as thermal noise needs to be suppressed, so the system is operated at cryogenic temperature inside a dilution fridge[3]. Among the main Haloscope experiments there are RBF–UF (Rochester-Brookhaven-Fermilab–University of Florida) [4], ADMX (Axion Dark Matter eXperiment) [5], HAYSTAC (Haloscope at Yale Sensitive to Axion CDM) [6], CAPP (Center for Axion and Precision Physics Research) [7] and $\mathrm{QUAX}_{\mathrm{a\gamma}}$ (QUest for AXions) [8].
Axion can be produced in the stars core and helioscopes aim to detect the axion flux that would come from the Sun. They use a dipole magnet directed toward the sun to convert axion into photons. Independently from their mass, axion coming from the sun would have energy of few keV so the corresponding photons are searched with high efficiency x-ray detectors. CAST (CERN Axion Solar Telescope) is an ongoing helioscope experiment at CERN.
In the magnetosphere of neutron stars axions can be converted into photons. Features of this process can be detected with current space or ground telescopes.
The Any Light Particle Search (ALPS)[9] employs a scheme that foresees production axion production in the laboratory. An intense light source emits photons that can be converted into axions in a strong magnetic field, axions can then pass through an optical wall, and a magnetic field on the other side converts axions back into photons that can be detected.
Other experiments search the axion through its coupling with the spin of fermionic particles. For instance, the $\mathrm{QUAX}_{\mathrm{ae}}$ experiment [10] involves a magnetic sample under a magnetic field, the axion interaction

has the effect of an equivalent oscillating rf field that produce spin flips in the sample. Spin flips would subsequently emit radio frequency photons.
The third interaction term in Equation 1.1 is exploited in experiments that employ nuclear magnetic resonance spectroscopy such as CASPEr (Cosmic Axion Spin Precession Experiment)[11].

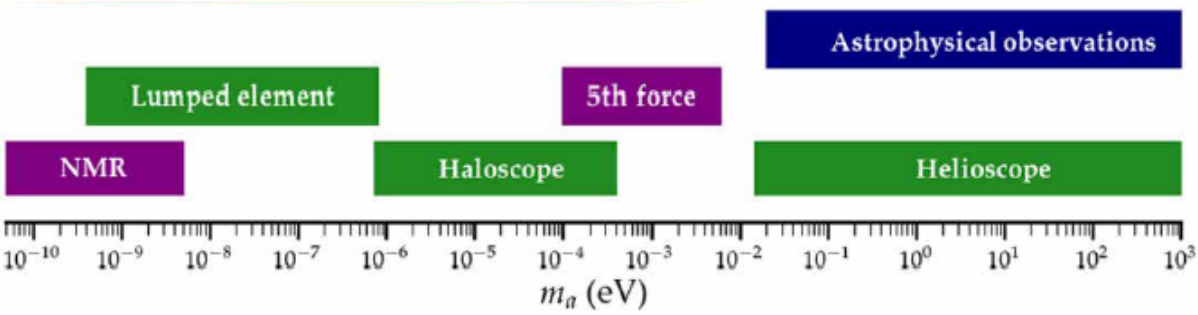

Figure 2: Allowed mass ranges for dark matter axions and different search methods employed. These methods exploit axion coupling with the photon (green) and with the nuclear spins (purple)[12].

1.3 Haloscope readout

In a haloscope experiment, signal is readout with a microwave receiver comprising different amplification stages. The first amplification stage in general determines the noise performance of the receiver thus superconducting parametric amplifiers are employed, which offer the lowest possible added noise set by quantum mechanics when operated at SQL. At high frequncy ($\sim 10\,\mathrm{GHz}$) the power expected from an axion signal is still about three orders of magnitudes lower than the noise power at SQL. To detect such a small signal, the system has to be stabilized for a long enough time so that by averaging the noise power its statistical fluctuations are reduced below the power increment expected from the axion signal. If that can be achieved, however, the integration time required limits the haloscope scan rate, and probing the whole 1-10 GHz range may take thousands of years of experimental live time [13].
The standard quantum limit can be overcome with a bolometric receiver[14]. This approach measures the cavity state in the base of Fock photon number eigenstates. The photon number is not subjected to vacuum fluctuations and the number of background photons can in principle be arbitrarily reduced by cooling the system. At optical frequencies, single photon detection relies on irreversible photoassisted ionization of various natural materials. The energy of a microwave photon is about 5 orders of magnitudes lower making it harder to detect. The methods that have been developed in recent years to achieve single microwave photon detection are based on the application of what can be defined as quantum sensors [15]. A quantum sensor is a system with discrete energy levels that can be initialized into a well-known state and whose state can be read out at least in one base. Many quantum sensing protocols require also the possibility to coherently control the state of the sensor. The interaction with the physical quantity under study influences the sensor temporal evolution so that readout of its state after the interaction gives information about the measured quantity. Superconducting qubits can be applied as quantum sensors for microwave photon detection. The interaction of these device with photons is described in the framework of circutit Quantum Electrodynamics (cQED) [16].

1.4 Quantum-enhanced axion search experiment

A photon counter has been applied in the field of DM search for a detector sensitive to hidden photons demonstrating a sub-SQL noise level [17]. The counter employed in this experiment is based on a superconducting qubit directly coupled to the detector resonant cavity. This requires the qubit to be in close proximity to the cavity, so this scheme can not be applied to haloscope experiments since the magnetic field would compromise the working of the qubit.
A recently introduced Single Microwave Photon Detector (SMPD) [18] capable of detecting photons

travelling on a transmission line (itinerant photons) will be employed for a pilot haloscope experiment to demonstrate a quantum-enhanced search of axions. The SMPD operates in a frequency range of about 100 MHz around the central frequency at 7.33 GHz corresponding to an axion mass $m_a = 25\,\mu$eV. The experiment will employ a NbTi cavity under an intermediate field of a 3 T magnetic field. The experiment objective is to identify the optimal quantum protocol.

1.5 Thesis structure

This thesis deals with important issues to be addressed for the pilot experiment.
section 2 discusses aspects of the main superconducting circuit components employed in the SMPD.
section 3 reports the results of some test performed on the cavity realized for the pilot experiment.
section 4 discusses the power of the signal expected from axions, the limit of linear receivers and the possible advantage of a photon counter.
section 5 gives the basic working principle of a parametric amplifier and report the result of a measurement of the equivalent noise temperature of a the TWPA present in the QUAX apparatus.
section 6 is a recap of some concepts of qubit dynamics and control techniques used for superconducting qubits.
section 7 explains the basic SMPD working principle and aspects related to the experimental setup.
section 8 reports the analysis of dark count data collected with the SMPD and of some preliminary tests performed to define measurement protocol to employ for the haloscope experiment.

2 Superconducting device

2.1 Superconductivity

Superconductivity is a phenomenon observed in many materials that below a critical temperature T_c present zero resistivity to dc currents and magnetic fields are expelled from the material bulk (Meissner effect). These effects can be phenomenologically described in terms of superconducting charge carriers, with number density n_s, that moving in the material without resistance produce a superconducting current density $\mathbf{J}_s$. This description leads to the London equations[19] that combined to the Maxwell equation

$$\begin{aligned} \nabla^2\mathbf{B} &= \frac{1}{\lambda_L^2}\mathbf{B} \\ \nabla^2\mathbf{J}_s &= \frac{1}{\lambda_L^2}\mathbf{J}_s \end{aligned} \tag{2.1}$$

Where $\mathbf{B}$ is the magnetic field and the London penetration depth is $\lambda_L \equiv \sqrt{\frac{m_e}{n_s e^2 \mu_0}}$, with m_e the electron mass, e the electric charge and μ_0 vacuum permeability. From the first London equation one finds that a magnetic field is exponentially suppressed on the length scale λ_L $B(x) = B_0 e^{-x/\lambda_L}$ at the material surface. Similarly, the second equation implies that superconducting currents flow only in a superficial layer of thickness λ_L, typically in the order of tens or hundreds of nm [20].
The Bardeen–Cooper–Schrieffer (BCS) theory shows that the superconducting carriers are made of electron pairs with opposite spins and opposite moments, called Cooper pairs. The pairs forms due to a weak attraction between electrons mediated by lattice phonons. The electrons involved in this process are those within an energy range $k_B T_c$ of the Fermi energy. This range can be used to estimate the momentum spread of the electrons involved

$$k_B T_c = \delta\left(\frac{p^2}{2m_e}\right) = \frac{p}{m_e}\delta p = v_F \delta p \tag{2.2}$$

with v_F the Fermi velocity. The spatial extent of the pairs ξ, also known as the coherence length, is related to the momentum spread according to the Heisenberg uncertainty principle.

$$\xi \delta p \approx \hbar \tag{2.3}$$

So from Equation 2.2

$$\xi = \frac{\hbar v_F}{k_B T_c} \tag{2.4}$$

For the most common superconducting material this length is of some tens of nm.
Each Cooper behaves as a spin zero Boson, so at low-temperature Bose-Einstein condensation occurs and all the pairs are in the lowest energy state described by the wavefunction

$$\psi(\mathbf{x}) = \sqrt{n_s(\mathbf{x})} e^{i\phi(\mathbf{x})} \tag{2.5}$$

The pairs density $n_s = |\psi|^2$ is usually uniform in the bulk of the superconductor and drops at the surface on the length scale given by the the correlation length ξ. $\phi(\mathbf{x})$ is usually referred to as the superconductor phase. Below T_c there is a temperature dependent energy gap $\Delta(T)$ between electrons in the normal conduction state and the one in the condensate state. When the system is kept at temperature T by the contact with a thermal bath the equilibrium state is the one that minimizes the free energy

$$F = U_{\text{int}} - TS \tag{2.6}$$

with U_{int} the system internal energy and S the entropy. When $T < T_c$ the minimum is reached when

part of the electrons condensate into Cooper pairs. The density of residual normal conduction electrons is proportional to the Boltzmann Factor

$$n_n \propto \exp\{-\Delta/k_B T\} \tag{2.7}$$

2.1.1 Flux quantization

In presence of a vector potential $\mathbf{A}$ the current density is given by [21]

$$\mathbf{J}_s = \frac{en_s}{m_e}(\hbar\nabla\phi - 2e\mathbf{A}) \tag{2.8}$$

where n_s and ϕ are as in Equation 2.5 the modulus and the phase of the Cooper pairs wavefunction. Considering a superconducting loop crossed by a magnetic field as shown in Figure 3 and computing the line integral of $\mathbf{J}_s$ over a loop in the bulk of the superconductor where $\mathbf{J}_s = 0$ one finds

$$\oint(\nabla\phi - 2\pi\frac{2e}{h}\mathbf{A})\cdot d\mathbf{l} = \Delta\phi - 2\pi\frac{2e}{h}\Phi_B = 0 \tag{2.9}$$

where Φ_B is the magnetic flux. Since the wavefunction is single-valued $\Delta\phi$ has to be an integer multiple of 2π and therefore φ_B is an integer multiple of the flux quanta $\Phi_0 = \frac{h}{2e} \approx 2.067 \times 10^{-15}$ Wb.

$$\Phi_B = n\Phi_0 \qquad n \in \mathbb{Z} \tag{2.10}$$

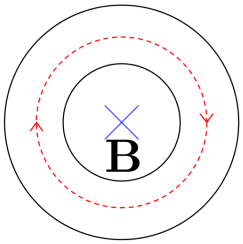

Figure 3: magnetic flux through a superconducting loop

2.1.2 Critical magnetic field

Superconductors are classified into type I and type II.

Type I superconductors are the ones for which $\frac{\lambda_L}{\xi} \leq \frac{1}{\sqrt{2}}$. Under a magnetic field strength $\mathbf{H}$ they behave as perfect diamagnet up to a maximum critical field $\mathbf{H}_c$. Above this field, the superconductivity is destroyed and the material turns to normal conductivity. The reason is that the supercurrents produced to compensate $\mathbf{H}$ and maintain $\mathbf{B} = 0$ inside the material increase the free energy of the superconducting state

$$F_s(H) = F_s(H = 0) + \frac{\mu_0 V H^2}{2} \tag{2.11}$$

where V is the superconductor volume. The critical field is reached when the free energy in the superconducting state reaches the one of the normal conductor.

Type II superconductors have $\frac{\lambda_L}{\xi} > \frac{1}{\sqrt{2}}$. Under a magnetic field strength $\mathbf{H}$ they have negative surface energy associated with the boundary between a superconducting region and a normal conducting region. For this reason above a lower critical field H_{c1}, the superconductor turns into a mixed phase in which it breaks up into finely divided normal and superconducting zones arranged in a periodic lattice, as shown in Figure 4.The field penetrates into the material through the normal conducting cores. Each core is surrounded by a vortex of superconducting current. To minimize the total free energy, the boundary

area tends to a maximum. Since the magnetic flux through a superconducting loop is quantized, the maximum area is reached when each vortex brings one flux quanta $\phi_0 = \frac{h}{2e}$.
When the material is in the mixed state (Figure 4) it has zero resistance to dc currents and a small resistance to ac currents. Above an upper critical field H_{c2} the vortex density becomes so high that normal cores starts to overlap and the superconductivity is completely lost[20].

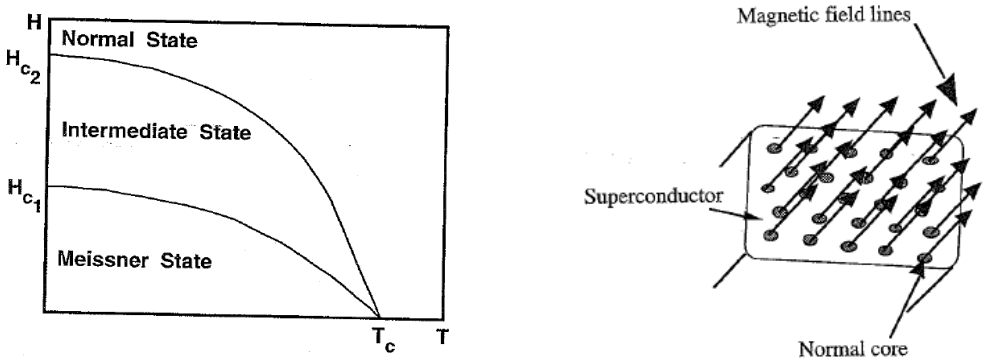

Figure 4: On the left: Phase diagram for a type II superconductor. On the right: Array of flux vortices that enters a type II superconductor in the mixed phase. Each vortex brings a single flux quanta. The cores are in the normal conduction state but the region between the cores remains superconducting. The separation of the vortices is a few thousand nanometers. [19]

Table 1 reports the critical fields for some materials commonly employed for superconductive cavities. The upper critical field of type II superconductors is generally higher than the critical field for type I materials.

Table 1: Critical temperature and upper critical field at zero temperature of some materials employed for superconducting cavities. For alloys the critical temperature and critical fields depends on the composition of the particular sample.

	Pb	Nb	NbTi	Nb_3Sn
T_c [K]	7.19	9.25	~ 10	~ 18.00
Type	I	II	II	II
$\mu_0 H_c$ [T]	0.08			
$\mu_0 H_{c2}$ [T]		0.27	$\gtrsim 10$	$\gtrsim 25$
ref.	[19][22]	[20]	[23]	[20]

2.2 Resistance to rf currents

For temperature below T_c the current flow in a superconductor can be described in terms of two fluids, one made of the Cooper pairs and the other made of normal electrons. DC currents are carried only by Cooper pairs and flow with zero resistance. In this flow, all the pairs move in the same direction and with the same velocity. Under an rf field, the inertia of the electron pairs comes into play. The supercurrent can not immediately respond to the field oscillations for this reason an oscillating electric field penetrates a surface layer and starts accelerating normal electrons introducing dissipations. The electric field is induced by the time-varying magnetic field that penetrates at the surface so

$$E \propto \frac{dB}{dt} \propto \omega B \tag{2.12}$$

where ω is the signal angular frequency. since the the normal electron current density is proportional to the field and to the density of normal electrons $j_n \propto n_n E$ and the dissipated power P_c is proportional to the product $J_n E$ then

$$P_c \propto n_n \omega^2 B^2 \tag{2.13}$$

The surface resistance can be defined in terms of the dissipated power per unit surface area

$$\frac{dP_c}{ds} = \frac{1}{2\mu_0^2} R_s B^2 \tag{2.14}$$

Equation 2.14,2.13 and 2.7 then gives

$$R_s = A_s \omega^2 \exp\left\{ -\frac{\Delta(0)}{k_B T} \right\} \tag{2.15}$$

with A_s a proportionality constant, and this approximation is valid for $T < T_c/2$ where the energy gap $\Delta(T)$ is close to its asymptotic value $\Delta(0)$. Thus the surface resistance has an exponential dependence from the temperature and increases with the square of the current frequency.

2.3 Josephson effect

When two superconductors are separated a thin barrier Cooper pairs can tunnel through it so a superconducting current can flow across the barrier. The system can be described with a two component wavefunction [21]

$$\mathbf{\Psi} = \begin{pmatrix} \sqrt{n_{s1}} e^{i\phi_1} \\ \sqrt{n_{s2}} e^{i\phi_2} \end{pmatrix} \tag{2.16}$$

where components 1 and 2 refer to the wavefunction on the two sides of the barrier. The time evolution is governed by the Hamiltonian

$$\hat{H} = \begin{pmatrix} e\frac{V}{2} & K \\ K & e\frac{V}{2} \end{pmatrix} \tag{2.17}$$

Where V is the voltage difference across the junction ad K is a constant that accounts for the tunneling of the pairs. From the Schrödinger equation and using the approximation $n_1 \approx n_2 \approx n_0$ one finds the Josephson equations for the current I and the voltage V across the junction

$$\begin{aligned} I &= I_c \sin(\phi) \\ V &= \frac{\Phi_0}{2\pi} \frac{d\phi}{dt} \end{aligned} \tag{2.18}$$

Where $\phi \equiv \phi_2 - \phi_1$ and $I_c = \frac{2Ken_{s0}}{\hbar}$ is the maximum current that can flow through the junction without resistance and is called the junction critical current. From the Josephson equations it can be seen that a Josephson junction behaves as a nonlinear inductor

$$V = \frac{\Phi_0}{2\pi I_c \cos(\phi)} \frac{dI}{dt} \equiv L_J \frac{dI}{dt} \tag{2.19}$$

Real Josephson junctions are made of an oxide layer between two superconductors, thus the present also an intrinsic capacitance C_J.

2.4 Superconducting circuits

Superconducting circuits works with ac currents at GHz frequency. They are fabricated with lithographic and etching techniques from a deposition of superconducting material on an insulating substrate.

2.4.1 CPW resonators

CPW resonators are made of a central superconducting line of length l and width w, isolated by a gap of width s from the ground plate Figure 5. w and s are usually of few μm, l is of some mm. The resonator is usually capacitively coupled to transmission lines or other circuit elements.

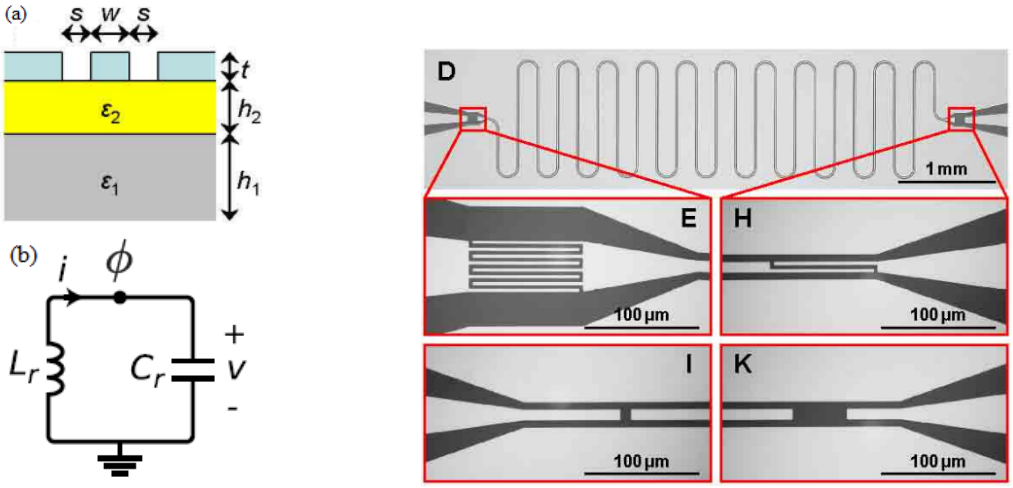

Figure 5: (a) CPW cross section. A superconducting layer of thickness t is patterned to create a central superconducting line of width s separated by gaps of width w from the grounded plate. An oxide layer (yellow) isolates the circuit from the substrate. (b) Lumped element equivalent circuit. (D) Optical microscope image of a CPW resonator. (E,F,G,H) Optical microscope image of different types of capacitors used to couple the resonator to a transmission line. [24] [25]

The resonance frequency of the fundamental mode is determined by the resonator geometry and by the choice of the materials [24]

$$\nu_0 = \frac{v_{ph}}{2l} \tag{2.20}$$

Where $v_{ph} = \sqrt{L_l C_l}$ is the phase velocity and L_l, C_l are the inductance and capacitance per unit length. For superconductors the inductance is the sum of the geometrical inductance and of the kinetic inductance due to Cooper pairs inertia. For some devices the latter contribution is much smaller than the geometrical one and the inductance and capacitance are given by [24]

$$\begin{aligned} L_l &= \frac{\mu_0}{4}\frac{K(k_0')}{K(k_0)} \\ C_l &= 4\epsilon_0\epsilon_{\text{eff}}\frac{K(k_0)}{K(k_0')} \end{aligned} \tag{2.21}$$

where ϵ_{eff} is the the effective permittivity that depends on the substrate. K denotes the complete elliptic integral of the first kind

$$K(x) \equiv \int_0^{\frac{\pi}{2}} \frac{d\theta}{\sqrt{1 - x^2\sin^2(\theta)}} \tag{2.22}$$

And the two arguments of K are $k_0 = w/(w+2s)$, $k_0' = \sqrt{1-k_0^2}$.
The system can be usefully described in terms of an equivalent lumped element LC circuit as shown in Figure 5 (b). This system behaves as a harmonic oscillator in which the energy oscillates between the electric field in the capacitor and the magnetic field in the inductor. The quantum counterpart of the normalized charge in the capacitor $n = \frac{Q}{2e}$ and of the normalized magnetic flux in the inductor $\phi = \frac{\Phi_B}{\Phi_0}$ are two operators $\hat{n}$ and $\hat{\phi}$ with the commutation relation $\left[\hat{\phi}, \hat{n}\right] = i$. So the system Hamiltonian is the one of a quantum harmonic oscillator

$$\hat{H} = 4E_C\hat{n}^2 + E_L\hat{\phi}^2 \tag{2.23}$$

with $E_C \equiv \frac{e^2}{2C}$ and $E_L \equiv \frac{1}{L}\left(\frac{\Phi_0}{2\pi}\right)^2$

2.4.2 SQUID

A SQUID is made of a superconducting loop with two Josephson junctions as shown in Figure 6.

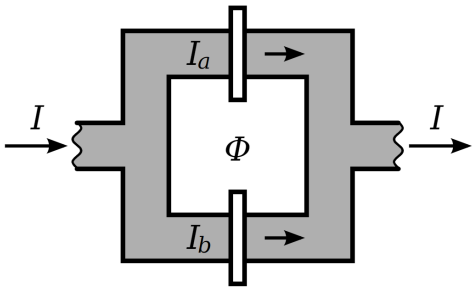

Figure 6: A SQUID is made of a superconducting loop with two Josephson junctions in parallel. The inductance of the SQUID depends on the magnetic field threading the loop.

The flux quantization (Equation 2.10) becomes in this case

$$\phi_a - \phi_b + 2\pi\frac{\Phi_B}{\Phi_0} = 2\pi n \qquad n \in \mathbb{Z} \tag{2.24}$$

Where a,b label the two junctions and Φ_B is the total magnetic flux accounts for externally applied magnetic field and for the flux generated by geometric self inductance of the loop. Considering for simplicity a simmetric SQUID $I_{ca} = I_{cb} = I_c$ the current flowing trhough the loop is found to be [26]

$$I = I_c\sin(\phi_a) + I_c\sin(\phi_b) = 2I_c\cos\left(\pi\frac{\Phi_B}{\Phi_0}\right)\sin(\phi) \tag{2.25}$$

where $\phi \equiv (\phi_a + \phi_b)/2$. This equation shows that the SQUID loop behaves as a single Josephson junction with a critical current that depends on the magnetic flux through the loop. For this reason one of the main applications of SQUIDs is for measurement of weak magnetic fields.
An advantage of the SQUID is that its inductance can be tuned by changing the externally applied flux. When the current is small compared to the critical one I_c and the flux due to self inductance is negligible compared to external one Φ_e, the squid inductance can be written as

$$L_s = \frac{\Phi_0}{2\pi I_c\left|\cos\left(\frac{\Phi_e\pi}{\Phi_0}\right)\right|} \tag{2.26}$$

When a SQUID is inserted in a CPW resonator it can be used to tune the resonant frequency [27]

$$\nu = \frac{\nu_b}{1 + L_s/L_t} \tag{2.27}$$

with L_t the resonator total inductance.

2.4.3 Transmon qubit

A transmon qubit is made of a Josephson junction parallel to a capacitor as shown in Figure 7. The energy in the capacitor is given by

$$E_{\text{capacitor}} = \frac{1}{2C_{tot}}Q^2 = 4E_C n^2 \tag{2.28}$$

where the total capacitance $C_{tot} = C_s + C_J$ is the sum of the shunt capacitance and of the intrinsic junction capacitance. The energy of the junction inductance can be calculated as

$$E_{\text{inductor}} = \int_0^t V(t)I(t)dt = \int_0^t \frac{\Phi_0}{2\pi}\frac{d\phi}{dt}I_c\sin(\phi)dt = -\frac{\Phi_0 I_c}{2\pi}\cos(\phi) \tag{2.29}$$

Similarly to the case of CPW resonators this system can be quantized and is described by the Hamiltonian [25]

$$\hat{H} = 4E_C\hat{n}^2 - E_J\cos(\hat{\phi}) \tag{2.30}$$

Where $E_J = I_c\Phi_0/2\pi$ is called the Josephson energy. Transmon qubits are usually designed such that $E_C \ll E_J$.

The Hamiltonian of Equation 2.30 is the one of an anharmonic oscillator. Indeed the first term can be seen as a kinetic energy term while the second as potential energy that has a cosine profile instead the parabolic one of a harmonic oscillator. Thanks to the anharmonicity the Hamiltonian eigenstates are not equally spaced in energy. So the transition energy $\hbar\omega_{01}$ from ground $|0\rangle$ to first excited $|1\rangle$ state is different from the one for the transition to higher excitation states (see Figure 7). This is crucial for using the system as a qubit, as it possible to control the system with pulses at the angular frequency ω_{01} avoiding transitions to higher states. The system can then be described as an effective two level system with the Hamiltonian

$$\hat{H}_{\text{qubit}} = -\hbar\omega_{01}\frac{\hat{\sigma}_z}{2} \tag{2.31}$$

with $\hat{\sigma}_z$ the Pauli-z operator

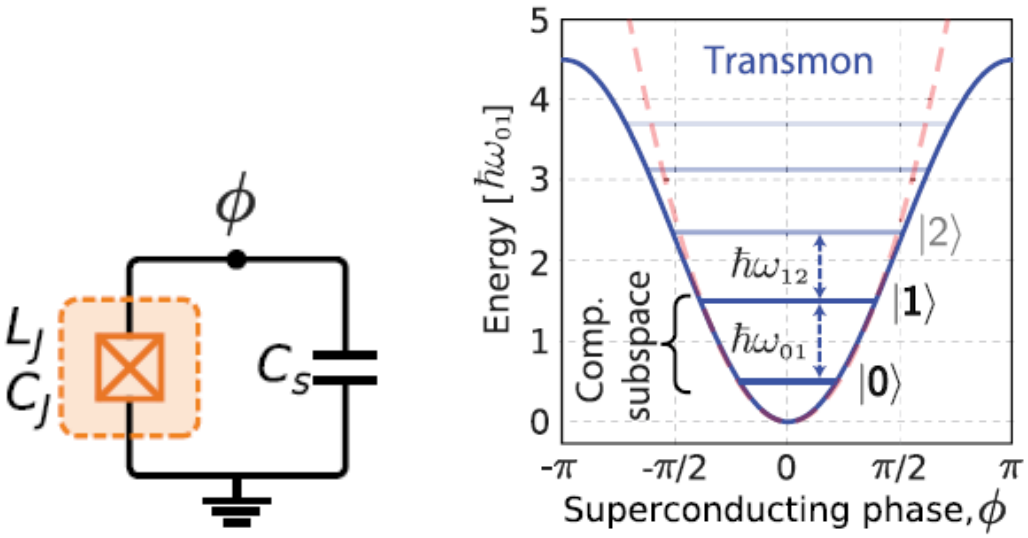

Figure 7: On the left: Transmon qubit circuit. The orange box represents a Josephson junction with inductance L_J and capacitance C_J. On the right: The transmon anharmonic potential yields non-equidistant energy levels. This allows to isolate the two lowest energy levels $|0\rangle$ and $|1\rangle$ that constitute the two-dimensional qubit subspace.[21]

3 Microwave Cavity

3.1 Cavity Fundamentals

The description of electromagnetic field in a resonant cavity start from the solution of Maxwell equations in a certain volume with given boundary conditions given by metallic walls. The wave equation in vacuum gives

$$\left(\nabla^2 - \frac{1}{c^2}\frac{\partial^2}{\partial t^2}\right)\begin{pmatrix}\mathbf{E}\\ \mathbf{B}\end{pmatrix} = 0 \tag{3.1}$$

Considering a waveguide with a constant cross section and perfect conducting walls, Shown in Figure 8, the boundary conditions are

$$\mathbf{E}\cdot\hat{n} = 0 \qquad \mathbf{B}\times\hat{n} = 0 \tag{3.2}$$

with $\hat{n}$ the normal versor to the boundary surface.
In cylindrical coordinates z, ρ, ϕ, wave solutions travelling along the z-axis are written as

$$\mathbf{E} = \mathbf{E}(\rho,\phi)e^{i(kz-2\pi\nu t)} \tag{3.3}$$

$$\mathbf{B} = \mathbf{B}(\rho,\phi)e^{i(kz-2\pi\nu t)} \tag{3.4}$$

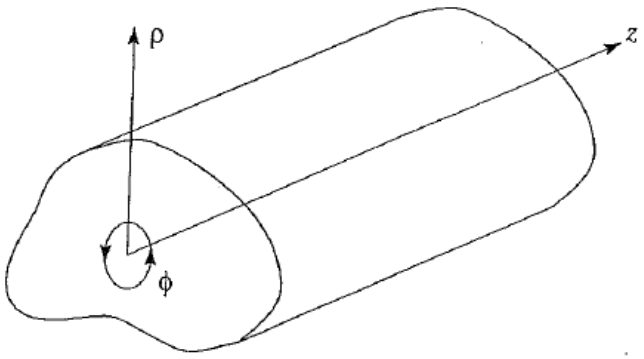

Figure 8: constant cross section waveguide [19] .

The wave equation then takes the form of the eigenvalue equation

$$\left[\nabla_\perp^2 + \frac{(2\pi\nu)^2}{c^2} - k^2\right]\begin{pmatrix}\mathbf{E}\\ \mathbf{B}\end{pmatrix} = 0 \tag{3.5}$$

The solutions of Equation 3.5 form an orthogonal set with respect to the scalar product

$$\langle \mathbf{E}_2, \mathbf{B}_2 | \mathbf{E}_1, \mathbf{B}_1\rangle = \frac{1}{2}\left(\int d^3\mathbf{x}\epsilon_0\epsilon(\mathbf{x})\mathbf{E}_2^*\cdot\mathbf{E}_1 + \int d^3\mathbf{x}\frac{1}{\mu_0}\mathbf{B}_2^*\cdot\mathbf{B}_1\right) \tag{3.6}$$

with $\epsilon(\mathbf{x})$ the space-dependent relative dielectric constant. The solutions are called Transverse Magnetic (TM) if $B_z = 0$ or Transverse Electric (TE) if $E_z = 0$.
Taking for instance a TM solution, the transverse fields can be expressed as a function of E_z.

$$\begin{aligned}\mathbf{E}_\perp &= \frac{ik}{\gamma^2}\nabla_\perp E_z \qquad \gamma^2 \equiv \frac{(2\pi\nu)^2}{c^2} - k^2\\ \mathbf{B}_\perp &= \frac{2\pi\nu\epsilon_0\mu_0}{k}\hat{z}\times\mathbf{E}_\perp\end{aligned} \tag{3.7}$$

To obtain the field in cavity we consider two perfect conductors in the planes $z = 0$ and $z = d$. The solutions are standing waves that for a TM mode can be expressed as

$$E_z = \psi(\rho,\phi)\cos\left(\frac{\pi l}{d}z\right) \qquad l = 0,1,2,... \tag{3.8}$$

And Equation 3.5 can be rewritten as

$$(\nabla_\perp^2 - \gamma^2)\psi(\rho,\phi) = 0 \tag{3.9}$$

For a cylindrical geometry, a set of solutions that are labelled TM_{mnl} is found, with integer indices m, n and l related to the number of nodes along the directions $\hat{\phi}$ $\hat{\rho}$ and $\hat{z}$. The solutions are written in terms of the Bessel functions $J_m(\rho)$ as [19]

$$E_z^{(mnl)} = E_0\cos\left(\frac{l\pi z}{d}\right)J_m\left(\frac{u_{mn}\rho}{R}\right)\cos(m\phi) \tag{3.10}$$

$$\nu_{nml} = \frac{c}{2\pi}\sqrt{\left(\frac{u_{mn}}{R}\right)^2 + \left(\frac{l\pi}{d}\right)^2} \tag{3.11}$$

where R is the radius of the cylinder and u_{mn} is the n-th zero of the Bessel function J_m.
For a real cavity whose geometry differs from the perfect cylinder, solutions that can be thought of as perturbations of the TM_{mnp} modes and that are therefore indicated with the same nomenclature. In most cases, it is hard to find analytically the solutions but they can be numerically computed. A software capable of performing such computation is Ansys HFSS [28].
Not every cavity mode is axion-sensitive, indeed as discussed in section 4, for a haloscope with an axial magnetic field, the power of the axion signal is proportional to the form factor : [29]

$$C_{nml} \equiv \frac{\left|\int d^3\mathbf{x}\mathbf{E}_{nml}\cdot\hat{\mathbf{z}}\right|^2}{V\int d^3\mathbf{x}\epsilon(\mathbf{x})\left|\mathbf{E}_{nml}\right|^2} \leq 1 \tag{3.12}$$

with V the cavity volume. The form factor vanishes for TE modes and is a factor of order 1 for the TM_{010} mode (Figure 12) which is the one usually employed in haloscope experiments.
An important parameter that characterizes losses in a resonator is the quality factor Q that is defined as

$$Q \equiv \frac{2\pi\nu_0 U}{P_c} \tag{3.13}$$

with U the energy stored in the resonator, ν_0 the resonant frequency and P_c the power dissipated via Joule heating. The total energy in the cavity is given by the volume integral

$$U = \frac{1}{2}\epsilon_0\int_V |\mathbf{E}|^2 d^3x = \frac{1}{2\mu_0}\int_V |\mathbf{B}|^2 d^3x \tag{3.14}$$

while the dissipated power is given by

$$P_c = \frac{1}{2\mu_0^2}R_s\int_S |\mathbf{B}|^2 d^2x \tag{3.15}$$

So the quality factor can be written as

$$Q = \frac{1}{R_s}\frac{2\pi\nu_0\mu_0\int_V |\mathbf{B}|^2 d^3x}{\int_S |\mathbf{B}|^2 d^2x} \equiv \frac{G}{R_s} \tag{3.16}$$

where G is called geometry constant.

3.1.1 Cavity testing

Tho evaluate the key parameters, quality factor Q and resonant frequency ν_0, the cavity is tested according to the the scheme shown in Figure 9. The cavity is coupled to a pair of antennas. The coupling parameter

β is defined as the ratio of the power extracted by the antenna P_e to the one internally dissipated by the cavity P_c.

$$\beta \equiv \frac{P_e}{P_c} \tag{3.17}$$

The scheme generally used to test a cavity uses two ports. The power waves $a_{\nu,i}$ traveling into and $b_{\nu,i}$ traveling out of a port are defined as [30]:

$$a_i = \frac{V_{\omega,i} + Z_0 I_{\omega,i}}{2\sqrt{Z_0}} \qquad b_i = \frac{V_{\omega,i} - Z_0 I_{\omega,i}}{2\sqrt{Z_0}} \tag{3.18}$$

$V_{\nu,i}$ and $I_{\nu,i}$ are the Fourier components, at frequency ν, of the voltage and current in the port i. Z_0 is an arbitrary reference impedance, generally set to $Z_0 = 50\ \Omega$ that gives the wave the dimension of $\sqrt{power}$. The relation between the waves going into the resonator and the ones coming out is determined by the scattering matrix of the resonator S.

$$\begin{pmatrix} b_{\omega,1} \\ b_{\omega,2} \end{pmatrix} = \begin{pmatrix} S_{11} & S_{12} \\ S_{21} & S_{22} \end{pmatrix} \begin{pmatrix} a_{\omega,1} \\ a_{\omega,2} \end{pmatrix} \tag{3.19}$$

A two ports cavity resonator is well described by an equivalent lumped element circuit shown in Figure 9 The elements of the equivalent circuit are related to cavity characteristics as follows:

- resonance $\nu_0 = \frac{1}{2\pi\sqrt{CL}}$
- Unloaded quality factor $Q = \frac{1}{R}\sqrt{\frac{L}{C}}$
- couplings $\beta_i = \frac{R_{ei}}{R}\ i = 1, 2$

The scattering matrix of the equivalent circuit can be written as in [31].

$$S = \frac{1}{1 + \beta_1 + \beta_2 + 2iQ\delta} \times \begin{pmatrix} 1 - \beta_1 + \beta_2 + 2iQ\delta & \sqrt{\beta_1\beta_2} \\ \sqrt{\beta_1\beta_2} & 1 + \beta_1 - \beta_2 + 2iQ\delta \end{pmatrix} \tag{3.20}$$

with

$$\delta \equiv \frac{\nu - \nu_0}{\nu_0} \tag{3.21}$$

The scattering matrix is measured using a two-port Vector Network Analyzer (VNA), an instrument that measures the amplitude and the phase of the reflected and transmitted signal.
The loaded quality factor is defined as

$$Q_L \equiv \frac{2\pi\nu_0 U}{P_c + P_{e1} + P_{e2}} \tag{3.22}$$

and it is related to the unloaded quality factor by

$$\frac{1}{Q_L} = \frac{1}{Q}(1 + \beta_1 + \beta_2) = \frac{1}{Q} + \frac{1}{Q_1} + \frac{1}{Q_2} \tag{3.23}$$

with

$$Q_i \equiv \frac{2\pi\nu_0 U}{P_{ei}} = \frac{Q}{\beta_i} \tag{3.24}$$

The power transfer between the two ports has a Lorentzian profile, as shown in Figure 16. The maximum at the resonance frequency ν_0. The upper (ν_u) and lower (ν_l) cut-off frequencies are defined as the frequencies at which the power transfer is half the maximum

$$\left| \frac{S_{12}(\nu)}{S_{12}(\nu_0)} \right|^2 = \frac{1}{2} \tag{3.25}$$

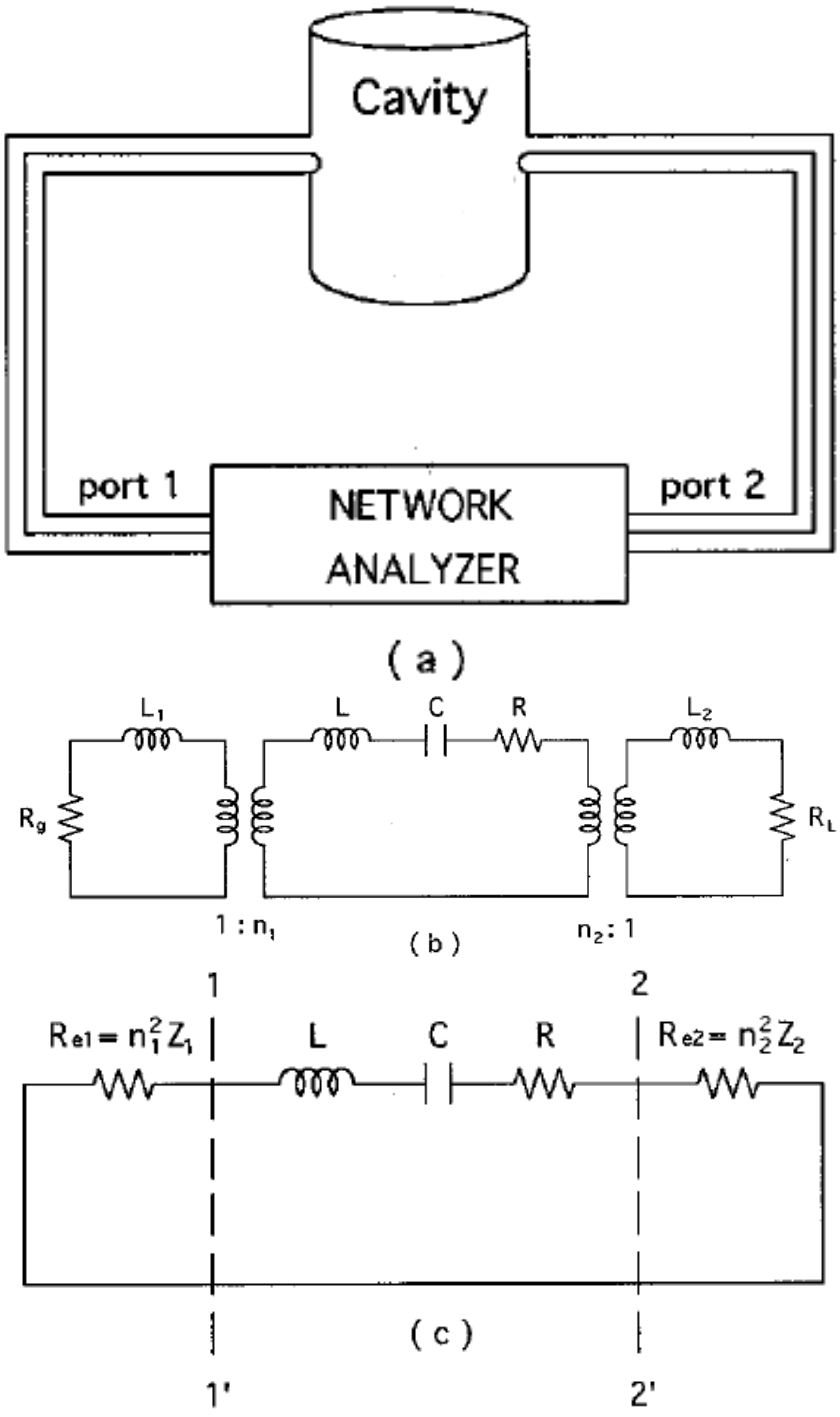

Figure 9: (a) The measurement system, (b) equivalent circuit of a loop coupled cavity, (c) equivalent circuit referred to the middle loop [31].

From Equation 3.20 one can see that this two frequencies are symmetric with respect to ν_0 and that

$$Q_L = \frac{\nu_0}{\nu_u - \nu_l} = \frac{\nu_0}{\Delta\nu} \tag{3.26}$$

This expresses the relation between the quality factor and the cavity linewidth $\Delta\nu$. The coupling of a resonator to a transmission line is often expressed also in terms of the coupling rate defined as

$$\kappa_i \equiv \frac{2\pi\nu_0}{Q_i} \tag{3.27}$$

And the total linewidth is then expressed as

$$\Delta\nu = \Delta\nu_c + \kappa_1/2\pi + \kappa_2/2\pi \tag{3.28}$$

with $\Delta\nu_c$ the unloaded quality factor.

3.2 High Q in multitesla fields

For a haloscope experiment, it is desirable to have a high-Q cavity since that would improve the signal-to-noise ratio enhancing sensitivity and scan rate [32]. Pure niobium Superconducting cavities have a small surface resistance at microwave frequency and are capable of reaching Q values $> 2 \times 10^{11}$ [33]. However, the magnetic field required in an haloscope $B_0 \sim 10\,\mathrm{T}$ is well above the niobium critical field (Table 1). State of the art haloscope experiments have typically operates with copper cavities [5][6]. Studies have shown that improvements can be obtained by employing coatings done with superconducting alloys such as NbTi, Nb_3Sn, and YBCO [34] [35] [36]. These alloys are type II superconductors with high upper critical field and even under multitesla field provide a smaller surface resistance than copper. The cavity that will be employed for the pilot experiment is a copper cavity with a NbTi coating deposited via magnetron sputtering. A copper cavity at the frequency of interest is about $Q \approx 2 \times 10^4$. As detailed in subsection 3.4 at Liquid Helium (LHe) temperature, under 3 T field our cavity shows a quality factor of $Q \approx 4 \times 10^5$ largely exceeding that of a copper cavity. We can expect further improvements when the cavity will be held at mK temperature.
High quality factors can also be obtained in cavities that exploit higher-order modes that allow for probing heavier axions (higher frequency) without reducing the cavity volume. This is important as the axion signal is proportional to the detector volume. The main disadvantage of higher order modes is that they have a form factor much lower than that of the fundamental mode. Indeed these modes present multiple lobes in which the field is oriented in opposite directions, so some of these lobes give a negative contribution to the integral at the numerator in Equation 3.12. Proposals to employ these modes for haloscope cavities are based on the suppression of the negative contributions by inserting in the cavity dielectric shells that reduce the field amplitude in the opposite lobes [37][38].

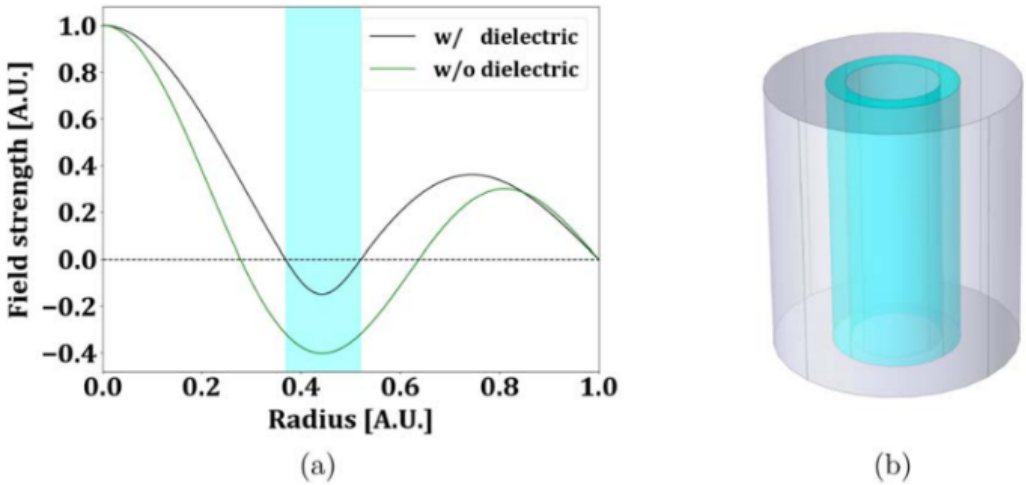

Figure 10: (a) The radial profile of the axial component of the TM030 mode axial electric field. The two curve shows the profile with (back) or without (green) the dielectric medium (cyan). (b) Dielectric shell to implement the effect in a cylindrical pill-box cavity.[37]

3.3 Cavity design and FEM (finite Element Simulation) simulation

An essential tool for cavity design are simulation software such as Ansys HFSS [39]. Ansys HFSS is a full-wave frequency-domain three-dimensional electromagnetic field solver which uses the finite element method to solve Maxwell's equations. There are two main types of solutions that can be calculated. The eigenmode solver calculates the natural resonances of the cavity based upon geometry, materials, and boundary conditions. It calculates modal frequencies, unloaded quality factors, and electromagnetic field profiles. The driven modal solution uses one or more ports to excite the cavity structure. It can be applied to predict transmission and reflection coefficients and study how to achieve critical coupling to a cavity mode.
The cavity that will be employed for the pilot experiment has a cylindrical body closed by two conical end caps. Its dimensions are summarized in Table 2, referring to resonator tested in this thesis and designed for the first generation SMPD. A new cavity has been designed since a new generation SMPD with improved performance and a slightly different working range $(7.28 - 7.38)$ GHz has now been realized. The new cavity has the same geometry but with a radius reduced to $r_{cyl} = 15.82$ mm . The cavity is carved out of a copper cylinder cut into two semi-cells along a longitudinal plane. A NbTi coating is deposited on the walls of the cylindrical body and in the first 2 mm of the cones (see Figure 11).

Table 2: Cavity geometrical dimensions

Cylinder radius r_{cyl}	16.6 mm
Cylinder height h_{cyl}	125 mm
Cones height h_{con}	10 mm
Tuning rod radius r_{tun}	1 mm
T. rod distance from cavity axis	5 mm
T. rod travel range	4.8 mm

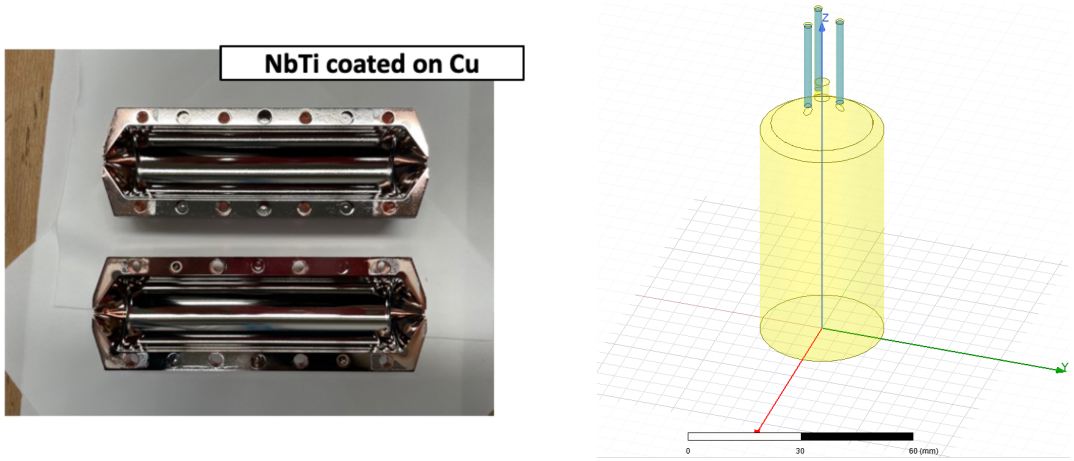

Figure 11: On the right: Copper cavity with NbTi deposition. The cavity is made of two semi-cells closed together. On the left: Tuning system made of 3 cylindrical sapphire rods (blue part). The rods can be inserted into the cavity and by adjusting the penetration the resonant frequency can be tuned. The plot shows only half of the cavity.

The mode of interest is the TM010 shown in Figure 12, as obtained by applying the eigenmode solver. In this mode, the electric field oscillates along the cavity axis and is maximum in the center. The magnetic field lies on transverse planes with field lines that turn around the cavity axis. With the dimentions in Table 2 FEM analysis gives $\nu_{010} = 7.07476$ GHz, due to numerical approximation usually the measured differ by about 1%. In the simulation we can treat the NbTi coated walls as perfect conductor and assume that the main loss channel is due to the copper end cups. This assumption is supported by the value of the quality factor measured in the real cavity.

3.3.1 Cavity frequency tuning

As the axion mass is unknown the cavity frequency needs to be varied across the largest possible frequency range. A commonly used tuning method employs a dielectric tuning rod that can be moved at different positions inside the cavity perturbing the field distribution of the cavity mode and its resonant frequency. The tuning system in our cavity is made of three cylindrical sapphire rods, disposed as shown in Figure 11, whose position can be vertically adjusted by a piezoelectric cryogenic motor that have a nominal maximum travel range of 4.8 mm [40].
Simulations enable us to study how the rods penetration Δz affect the resonance frequency shift $\delta\nu_{010}$, the quality factor Q, and the mode form factor C_{010} as shown in Figure 13. The tuning mechanism should be limited to the region highlighted in red in the figure since for $\Delta z \gtrsim 12\,\text{mm}$, the form factor quickly drops at low values. With a travel range of about 5 mm the cavity can be tuned of about 5 MHz. The quality factor is decreased by the insertion of the tuning bars, this effect is not directly due to losses on the sapphire, indeed at low temperature, the sapphire dielectric loss tangent is smaller than 10^{-7} [41]. The reductions of Q and C_{010} are both related to the fact that the TM_{010} is distorted by the presence of the rods the region with the higher field amplitude is concentrated in the end cap cone containing the rods. Figure 14 shows this effect in the case where the rods are completely inserted into the cavity. The form factor is reduced in this situation because the volume integral at the numerator in Equation 3.12 is decreased while the one at the denumerator is increased by the high sapphire dielectric constant. The quality factor is reduced because the cone caps are not covered by the NbTi coating so dissipations are increased.

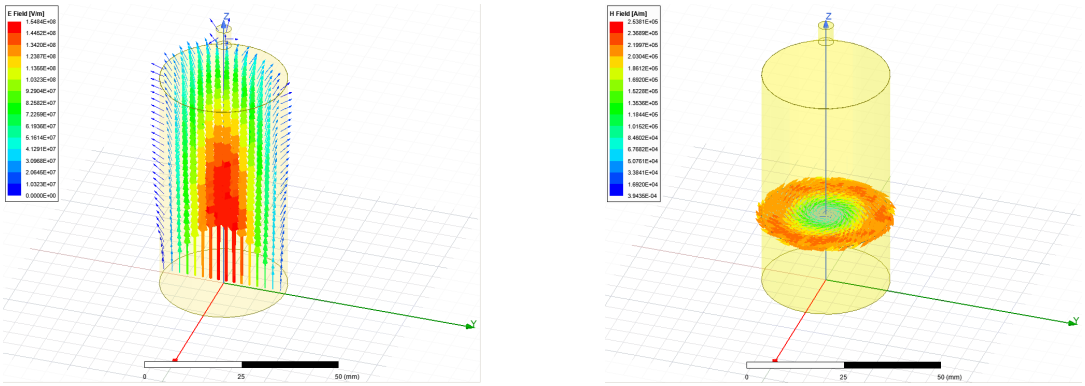

Figure 12: On the left: Electric field of the TM010 mode on a longitudinal plane. On the right: magnetic field of the TM010 mode on a transverse plane. To evaluate the mode quantities such as the resonant frequency we can exploit the TM mode with respect to the central cavity plane and simulate only half of the cavity volume saving computational time. This symmetry is broken by the fact that the tuning rods are placed only at one end of the cavity, so for a correct evaluation of the mode form factor under the effect of the rods, it is required to simulate the whole cavity.

3.4 Experimental cavity tests

3.4.1 Test at $B = 0\,\text{T}$

In a first test, performed at Laboratori Nazionali di Legnaro (LNL), we measured the scattering parameters of the NbTi cavity at LHe temperature. The cavity was enclosed in a chamber inserted in a LHe dewar. The chamber was filled with He gas at 500 mbar pressure at room temperature that decreased to about 50 mbar after system cooling. The temperature of the cavity was monitored a sensor attached to the the cavity support. We probe the cavity using two antennas connected at the two ends of the cavity and connected via coaxial transmission lines to a Vector Network Analyzer (VNA). The antennas consist of a 0.3 mm-long prolongation of the central conductor of the coaxial cables to achieve a coupling $\beta \ll 1$ in superconducting regime. So the loaded quality factor is close to the unloaded one.
During the cooling we use the VNA measure the cavity frequency ν and quality factor Q at different

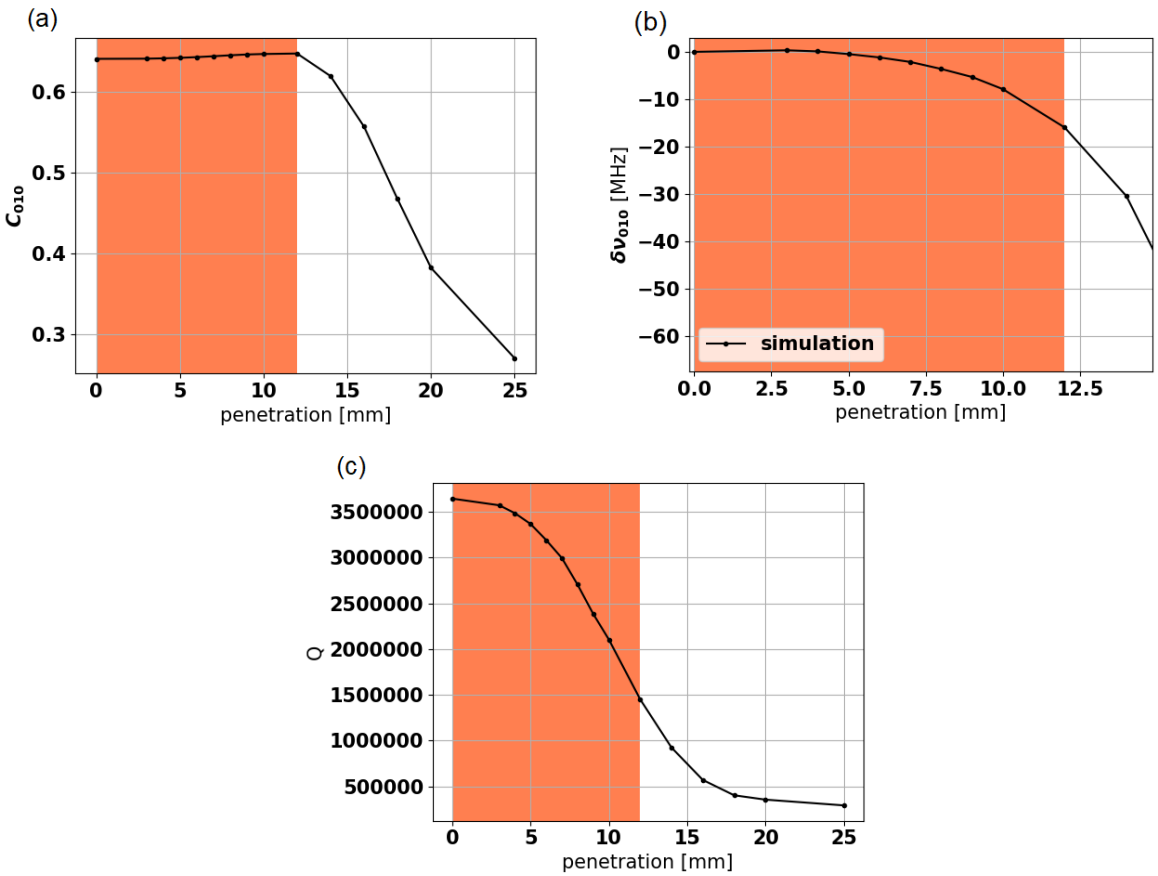

Figure 13: (a) Form factor vs tuning rods penetration. After penetration of about 12 mm the form factor is quickly degraded, so the tuning system should be used in the region highlighted in red. (b) frequency tuning vs rods penetration. With a travel range of about 5 mm the cavity frequency can be tuned of about 5 MHz. (c) Quality factor vs rods penetration. The quality factor decreases when the tuning rods are inserted. The increased dissipation is not related to the losses on the sapphire but to the fact that the mode gets modified in such a way that increases the field amplitude at the copper surface in the cone.

temperatures down to a minimum temperature of 4.4 K. Below NbTi critical temperature, we observe an increase of almost 2 orders of magnitude in the quality factor as shown in Figure 15 reaching about 3×10^6. We expect that the resonant frequency increases due to thermal contractions. Indeed, the resonant frequency is inversely proportional to the cavity radius (Equation 3.11). For a small variation of the cavity radius, the relation can be linearized

$$\nu_0 = \overline{\nu}_0(1 - \alpha_{Cu}T) \tag{3.29}$$

With $\alpha_{Cu} = 1.6 \times 10^{-5}$ K^{-1} the Copper linear expansion coefficient [42]. The fit in Figure 15 gives $\overline{\nu}_0 = 7.0018 \pm 0.0002$ GHz and shows that this is a good approximation for $T > 150$ K. At low temperature α_{Cu} is no longer constant[43].

The measured scattering parameters are shown in Figure 16. We can observe some distortion of the reflection coefficient S_{22} and that, despite beeing a reciprocal system, there is a small systematic difference between S_{12} and S_{21}. Fitting the data with Equation 3.20, the quality factor and the coupling coefficients can be estimated. For fitting purposes, it is convenient to rewrite the reflections and transmission coefficients as

$$S_{jj} = c_j \frac{1 - 2Q_L/Q_j + 2iQ_L\delta}{1 + 2iQ_L\delta} \tag{3.30}$$

$$S_{ij} = a_{ij} \frac{2Q_L}{1 + 2iQ_L\delta} \tag{3.31}$$

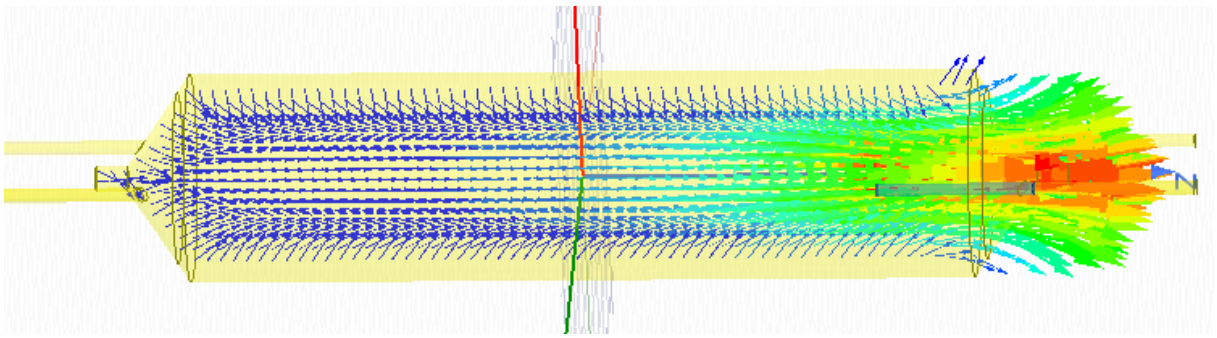

Figure 14: Mode distortion when the tuning rods are completely inserted into the cavity. The field is concentrated in the cone containing the rods, this leads to a reduction of the form factor and to increased dissipations.

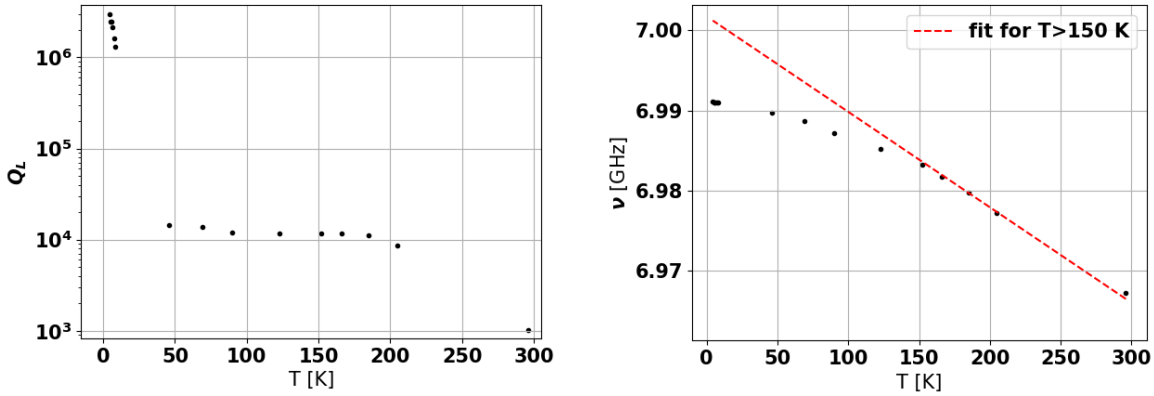

Figure 15: On the left: Loaded Quality factor vs temperature. There is a steep increase in the quality factor around the critical temperature $T_c = 9.2$ K at which NbTi become superconductive. On the right: shift of the resonant frequency due to thermal contractions.

and use as fitting parameters Q_L, Q_j and the proportionality constants a, c introduced to account for the attenuation due to the transmission lines.

Table 3: Parameters estimated from the fit of scattering parameters measurements.

S11	ν_0 [GHz]	Q_L	Q_1	$\beta_1 \approx Q_L/Q_1$
	6.991153 ± 0.000001	$3.037 \times 10^6 \pm 8 \times 10^3$	$5.58 \times 10^7 \pm 1 \times 10^5$	0.0544 ± 0.0002
S22	ν_0 [GHz]	Q_L	Q_2	$\beta_2 \approx Q_L/Q_2$
	6.991154 ± 0.000001	$3.04 \times 10^6 \pm 4 \times 10^4$	$5.67 \times 10^7 \pm 5 \times 10^5$	0.0536 ± 0.0002
S12	ν_0 [GHz]		Q_L	
	6.991153 ± 0.000001		$3.053 \times 10^6 \pm 1 \times 10^3$	
S21	ν_0 [GHz]		Q_L	
	6.991153 ± 0.000001		$3.060 \times 10^6 \pm 1 \times 10^3$	

From the results of the fits, reported in Table 3, we can see that the two antennas are indeed under-coupled and so the loaded quality factor is close to the unloaded one. The quality factor results above 3×10^6. This value is within a 20% difference from the one find in simulation, showing that indeed the major contribution to the losses comes from the copper cones.

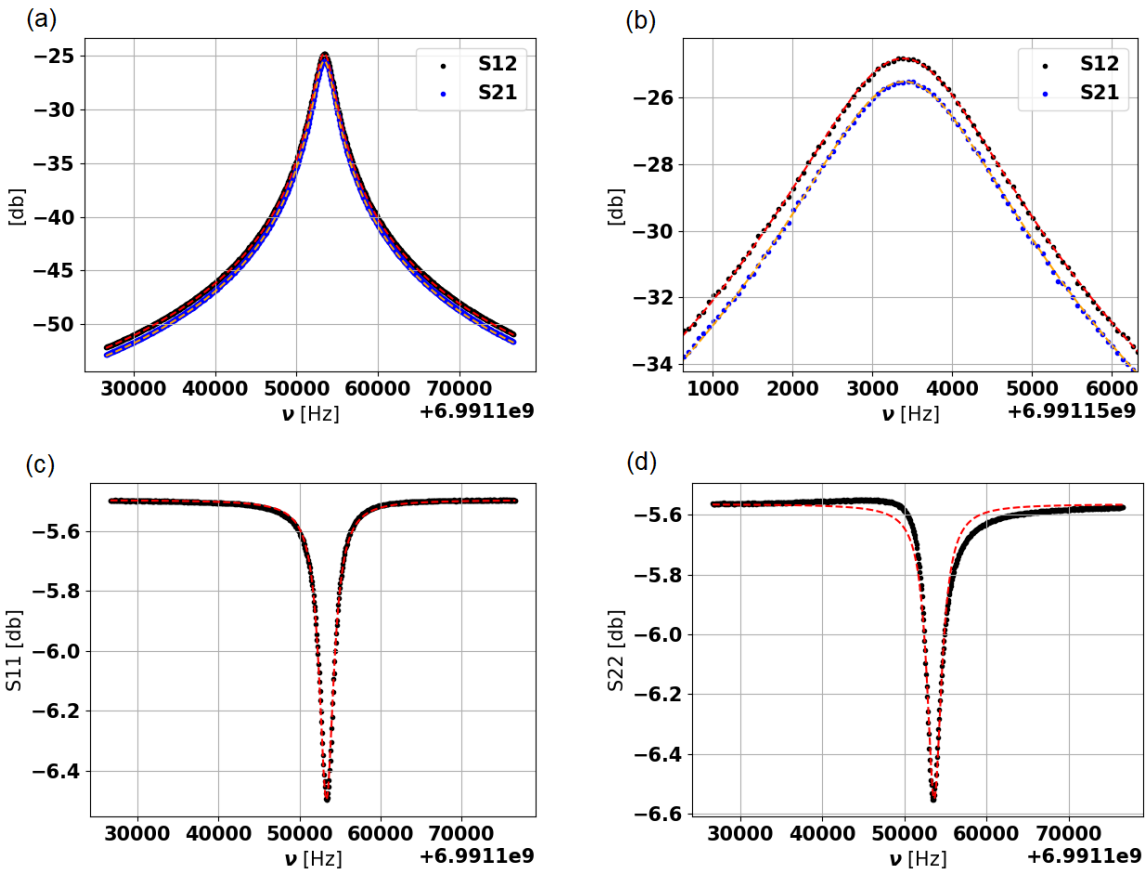

Figure 16: VNA measurements of the scattering parameters. (a) Transmission coefficients $|S_{12}|$ and $|S_{21}|$. (b) zoom around the resonance peak of the plot in (a). (c) and (d) reflection coefficients S_{11} and S_{22}.

3.4.2 Test under magnetic field

In a second set of measurements, performed at the laboratory led by U. Gambardella in Fisciano (Salerno), we tested the cavity immersed in an external magnetic field directed along the cavity axis. The cavity was cooled using a flow cryostat, allowing to cool the system down to 3.5 K The temperature of the He flow is controlled with a thermostat and the values reported in the following refer to the value set on this thermostat. A pump excracts the He gas from the chamber and the pressure is kept at about 600 mbar. The cavity is inserted in the bore of a solenoid magnet capable of producing maximum fields above 10 T. From tabulated values of the field profile, we can estimate that the magnitude of the field varies by about 40 % for displacement along the field axis of the order of the cavity length $\sim$ 15 cm, while it has negligible variations for displacements from the magnet axis in the radial direction of the order of the cavity radius. The field values reported in the following refer to the nominal one set on the control modulus of the solenoid current, which correspond to the field in the center of the magnet.
For data acquisition, we started from the zero-field configuration at the temperature of 4 K and we performed a temperature scan increasing it until the NbTi critical temperature. After a scan, we cooled down again the cavity to the minimum temperature and increase the magnetic field before performing the following temperature scan. Note that when the B field has been ramped up, we can not go back to the zero-field field configuration since some current would remain in the solenoid generating a residual field in the order of 100 Gauss. For each measurement point, we took three acquisitions of the S21 parameter and we use the standard deviation between the three to estimate uncertainties in the measured values. We observed a dependence of the resonant frequency on the temperature as shown in Figure 18, this provides us a means to evaluate the thermalization of the cavity at the temperature of the He flow. Indeed, when we change the temperature we can see a drift of the resonance peak and wait until it stabilizes around the new value.

Figure 17 shows how the loaded quality factor changes with respect to temperature and to the applied magnetic field.

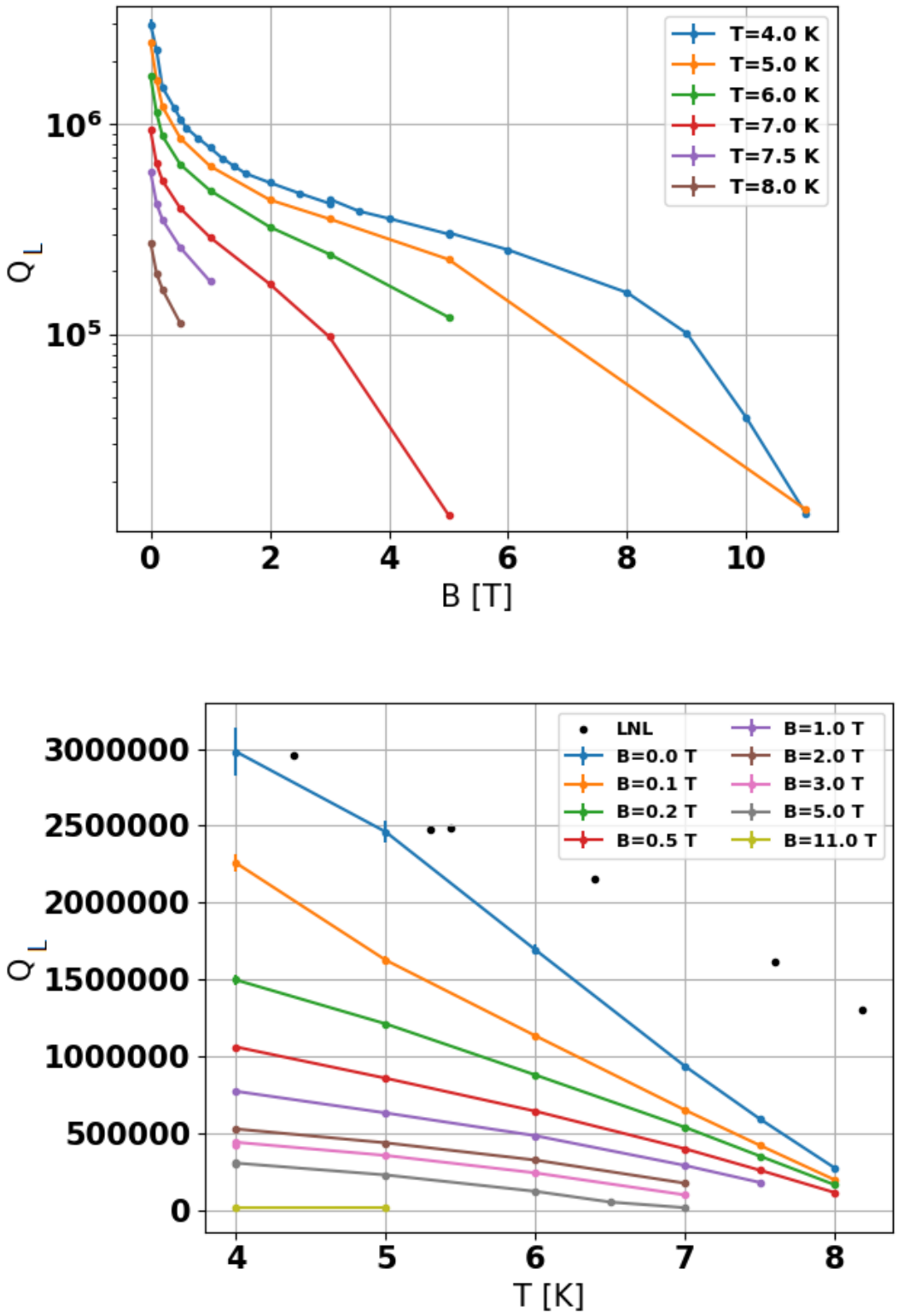

Figure 17: Top: Loaded quality factor vs applied magnetic field at different temperatures. Bottom: Loaded quality factor vs temperature under different applied magnetic fields. Black dots are the values measured at LNL without applied field.

The field that will be used in the pilot experiment is of 3 T, under this field at 4 K the loaded quality

factor is about 4×10^5. At 11 T we measure a loaded quality factor of about 1.5×10^4, comparable with the value measured above T_c, showing that the coating has completely turned to normal conductivity. Indeed under this field we do not see changes in the quality factor increasing the temperature from 4 to 5 K. In the range of temperatures we probed, the quality factor increases approximately linearly reducing the temperature, so we expect a further improvement of Q going to mK temperatures. From Figure 17 we can a faster decrease of the quality factor when the temperature increase respect to what observed in the test at LNL. However in the first test the data were taken during the transient cooldown without a temperature feedback control system, so the temperature values are less reliable than in this second test. Figure 18 shows the effect of temperature changes on the resonance frequency.

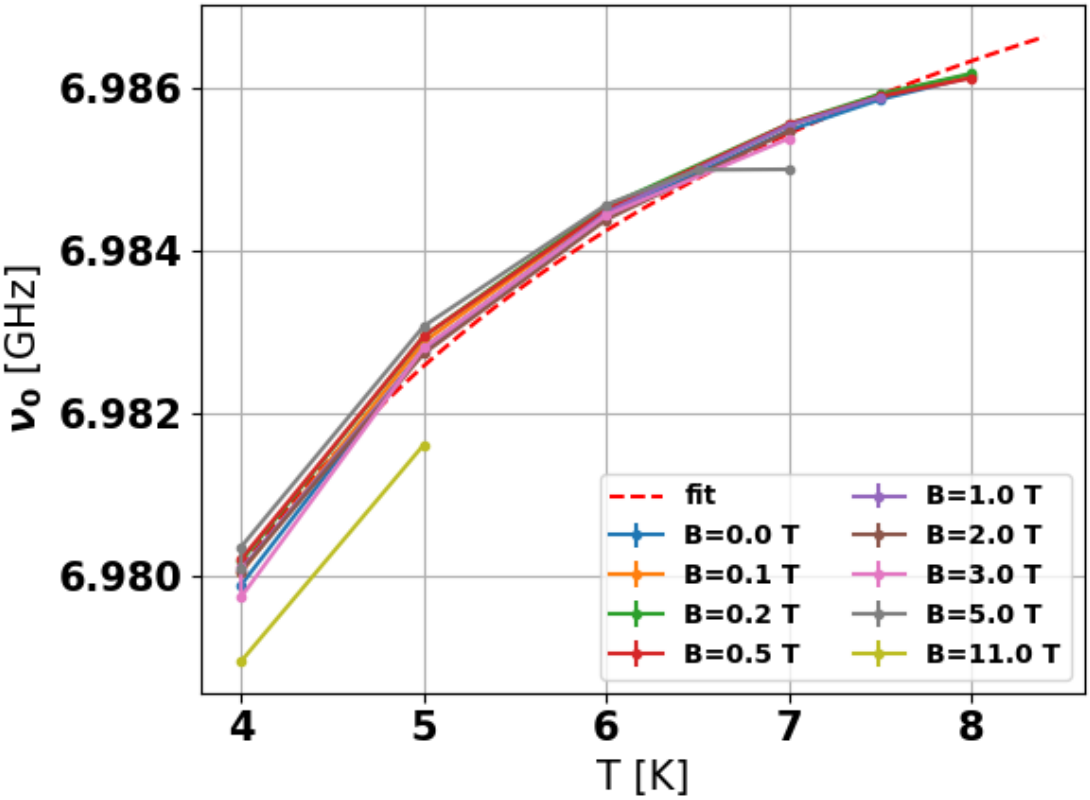

Figure 18: Frequency shift due to temperature variation. The fit is done on the data for B=0 T with a profile given by Clausius-Mossotti equation at constant pressure.

The dependence of the resonant frequency on the cavity temperature is similar under all applied fields. The value measured at zero applied field ad $T = 4$ K is $\nu_0 = 6.98556 \pm 0.00004$ GHz which is about 6 MHz lower than the value measured in the test at LNL laboratory. These effects can be related to the polarizability of the He inside the cavity. For a linear homogeneous and isotropic medium, the dielectric constant ϵ can be calculated with the Clausius-Mossotti equation [44].

$$\frac{\epsilon - \epsilon_0}{\epsilon + 2\epsilon_0} = \frac{4\pi N_A \alpha \rho_m}{3M} \tag{3.32}$$

with ϵ_0 the vacuum dielectric constant, N_A the Avogrado's number, α the polarizability, ρ_m the mass density and M the molecular mass. For a diluted gas the refractive index n can be approximated as

$$n \approx \sqrt{1 + \frac{3\alpha P}{k_B T}} \tag{3.33}$$

with P the gas pressure and k_B the Boltzmann constant. The resonance frequency of the cavity is inversely proportional to the index of refraction of the He inside it. Assuming that the pressure remained

constant in all measurements we can try to fit the dependence of ν_0 on T with a curve of the kind

$$\nu = \frac{A}{\sqrt{1 + \frac{B}{T}}} \tag{3.34}$$

Figure 18 shows that this curve has a trend similar to the data. Computing the He polarizability from the B coefficient obtained from the fit and for a pressure $P = 600$ mbar we find $\alpha_{He} \approx 1.1 \times 10^{-24}$ cm^3 while the actual value is $\alpha_{He} = 0.859 \times 10^{-24}$ cm^3 [45]. The difference can be explained by the uncertainty in the measurement of the pressure. The ratio between the resonant frequency measured at the lowest temperature without applied field in the first (ν_1) and second (ν_2) test is $\nu_1/\nu_2 \approx 1.0008$ while the one predicted by Equation 3.34 using the correct value of the He polarizability is $\sqrt{1 + \frac{3\alpha P_2}{k_B T_2}}/\sqrt{1 + \frac{3\alpha P_1}{k_B T_1}} \approx 1.0013$.

4 Axion signal

The aim of a haloscope is to exploit the axion electromagnetic interaction to produce a detectable microwave signal. The process for which a haloscope can detect axions is the inverse Primakoff effect. This effect is described by the Feynman diagram in Figure 19. In this process, an axion interacts with the magnetic field inside the cavity producing a photon at frequency $\nu_a = \frac{m_a c^2}{h}$.

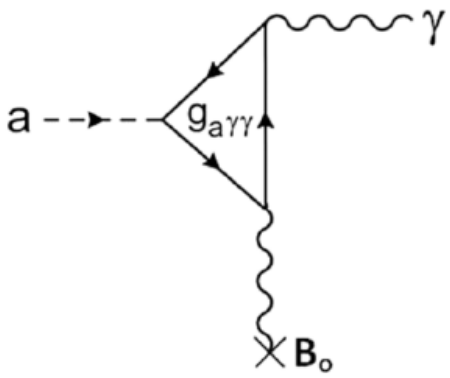

Figure 19: Inverse Primakoff effect

Experimental search however can not look for single scattering events but for the effect of the presence of the axion field that due to the high occupation number can be described as a classical field. The presence of the axion field a gives a modification of Gauss' law and Ampère's law of Maxwell's equations [12]

$$\begin{aligned} \nabla \cdot \mathbf{E} &= \rho - g_{a\gamma\gamma} \nabla a \cdot \mathbf{B} \\ \nabla \times \mathbf{B} - \frac{\partial \mathbf{E}}{\partial t} &= \mathbf{J} + g_{a\gamma\gamma} \left(\frac{\partial a}{\partial t} \mathbf{B} + \nabla a \times \mathbf{E} \right) \end{aligned} \tag{4.1}$$

Where ρ and $\mathbf{J}$ are the usual charge and current densities. The spatial coherence length of the axion field is inversely proportional to the axion mass and in general much larger than the detector size. Therefore one can assume $\nabla a \approx 0$ and that the only contribution comes from the time derivative of the axion field. The axion coherence time τ_a is instead shorter than any typical measurement time $\tau > \tau_a \approx 100\,\mu$s. So the axion signal results in incoherent electric field fluctuations indistinguishable from noise fluctuations. The signature of the signal is thus an increment of the power at the output of the cavity with respect to the one expected from other noise sources. From the modified Maxwell's equations, one can derive an expression for the axion signal's power expected in haloscopes experiments [6]. Assuming that the cavity resonant frequency corresponds to the axion frequency, the expected deposited power is given by [32] [36]

$$P_{a\gamma\gamma} = \left(g_\gamma^2 \frac{\alpha^2 \hbar^3 c^3 \rho_a}{\pi^2 \Lambda^4} \right) \times \left(\frac{\beta}{1+\beta} 2\pi \nu_c \frac{B_0^2}{\mu_0} V C_{nml} \frac{Q_L Q_a}{Q_a + Q_L} \right) \tag{4.2}$$

For easier readability, the quantities appearing in the equation are summarized in Table 4. Table 5 reports the expected axion signal power calculated for the experimental parameters in the pilot experiment and for the ones prospected for the QUAX experiment.
The constant g_γ is related to the coupling $g_{a\gamma\gamma}$ by

$$g_\gamma = \frac{g_{a\gamma\gamma}}{m_a c^2} \frac{\pi \Lambda^2}{\alpha} \tag{4.3}$$

The axion signal has a line shape reflective of the axion kinetic energy distribution. Assuming that dark matter obeys the standard halo model the velocity of axions follow a Maxwell-Boltzmann distribution. The signal line shape is then given by [46].

Table 4: Quantities appearing in Equation 4.2

g_γ	-0.97 (KSVZ) 0.36 (DSFZ)	ν_c	cavity frequency
α	fine structure constant	B_0	applied magnetic field
$\hbar$	Plank's constant	μ_0	vacuum permeability
c	speed of light	V	cavity volume
ρ_a	$0.45\,\mathrm{GeV/cm^3}$	C_{nml}	form factor
Λ	78 MeV	Q_L	loaded quality factor
β	antenna coupling	Q_a	10^6

$$g(\nu) = \frac{2}{\sqrt{\pi}}\sqrt{\nu-\nu_a}\left(\frac{3}{\nu_a\frac{c^2}{\langle v^2\rangle}}\right)^{3/2} e^{\frac{-3(\nu-\nu_a)c^2}{\nu_a\langle v^2\rangle}} \tag{4.4}$$

Where $\langle v^2\rangle = 270\,\mathrm{km/s}$ is the rms velocity of the dark matter halo[47]. The axion quality factor, given by the ratio of $\nu_a$over the signal linewidth is $Q_a = \frac{\nu_a}{\Delta\nu_a} \approx \frac{c^2}{\langle v^2\rangle} \approx 10^6$. A good choice for haloscope search would be to have a cavity quality factor comparable to the one of the axion. Indeed for $\Delta\nu_c < \Delta\nu_a$ not the whole signal is captured while for $\Delta\nu_c > \Delta\nu_a$ increases the noise in the measurement without increasing the signal power [6]. However, has been shown that an higher quality factor $Q > Q_a$ can improve the scan rate [32]. Despite the realization of high Q haloscope cavities, a narrowband receiver would open some other experimental challeges. Indeed the experiments conducted so far relied on the inequality $\Delta\nu_c \ll \Delta\nu_a$ to compute the reference noise baseline [48] [46].

Table 5: Expected axion signal power for the experimental parameters in the pilot experiment and for the ones prospected for the QUAX experiment. For the QUAX experiment here are considered the simulated parameters for a cavity that employs both dielectric elements to increase the form factor for the TM_030 and an Nb_3Sn superconducting coating.

	ν_c GHz	Q	β	B T	V cm^3	C_{nml}	$P_{a\gamma\gamma}\,10^{-24}$W	Γ_{sig} Hz
pilot exp.	7.3	4×10^5	1	3 T	113	0.64	0.95 (KSWZ)	0.2
							0.13 (DFSZ)	0.02
QUAX	10.48	1×10^6	1	14 T	1150	0.47	439 (KSWZ)	63
							60 (DFSZ)	8.7

4.1 Model for the axion cavity coupling

On a volume with the typical size of a resonant cavity and on the time scale of the cavity coherence time the axion field can be considered as a classical homogeneous field oscillating at $\omega_a = \frac{m_a c^2}{\hbar}$.

$$a \approx a_0\cos(\omega_a t+\phi_a) = \frac{\sqrt{2\rho_a\hbar^3c^3}}{\hbar\omega_a}\cos(\omega_a t+\phi_a) \equiv \frac{\sqrt{\hbar}}{2}(A_0e^{i\omega_a t}+A_0^*e^{-i\omega_a t}) \tag{4.5}$$

From a quantum mechanical point of view the electric field in the cavity is described by the operator

$$\hat{\mathbf{E}} = i\sum_k\sqrt{\frac{\hbar\omega_k}{2}}\left[\hat{a}_k\mathbf{U}_k e^{-i\omega_k t}-\hat{a}_k^\dagger\mathbf{U}_k^* e^{i\omega_k t}\right] \tag{4.6}$$

where k is an index that labels the cavity modes, $\mathbf{U}_k$ are the electric field solutions of the eigenvalue Equation 3.5 and $\hat{a}_k$,$\hat{a}_k^\dagger$ are the annihilation and creation operators for the photon Fock state. When the cavity is cooled down to mK temperature all the cavity modes are in a thermal state with a low occupation number that can be approximated as the vacuum state $|0\rangle$. Indeed the density matrix of a thermal state is given by

$$\hat{\rho}_T = \frac{1}{Z}\sum_n e^{-\frac{\hbar\omega}{k_B T}} |n\rangle\langle n| \qquad Z = \frac{1}{1-e^{-\frac{\hbar\omega}{k_B T}}} \tag{4.7}$$

and the probability of finding the system not in the vacuum state for $\omega/2\pi \approx 7\,\text{GHz}$ and $T \approx 10\,\text{mK}$ is

$$P(n>0) = 1 - \langle 0|\hat{\rho}_T|0\rangle = e^{-\frac{\hbar\omega}{k_B T}} \approx 2\times 10^{-15} \tag{4.8}$$

A quantum state can be graphically schematize as an ellipse in a phasor diagram that represents on its axis the two quadrature operators $\hat{X}_1 = \frac{1}{2}(\hat{a}+\hat{a}^\dagger)$, $\hat{X}_2 = \frac{1}{2i}(\hat{a}-\hat{a}^\dagger)$. The center of the ellipse have as coordinates the expected value of the two quadratures $(\langle\hat{X}_1\rangle, \langle\hat{X}_2\rangle)$. The lenght of the ellipse axis is given by the fluctuations of the two quadratures $|\Delta\hat{X}_j| = \sqrt{\langle\hat{X}_j^2\rangle - \langle\hat{X}_j\rangle^2}$, or of a combination of the two in the case the ellipse is rotated with respect to the diagram axis. As a consequence of the Heisenberg uncertainty principle the area of the ellipse can not be below $A_{min} = \frac{\pi}{4}$. The vacuum state correspond in this diagram to a circle with radius $\frac{1}{2}$. The effect of the axion field is to displace the state of the mode at the axion frequency from vacuum to a choerent state with low occupation number. Since the the phase relation between the axion field and the electromagnetic field remain constant only within the cavity coherence time $\tau_{cav} = \frac{1}{\Delta\nu_{cav}}$ the direction of the displacement randomly changes quickly and the net result is to enlarge the uncertainty ellipse of the vacuum state. The increase in the quadrature fluctuations are the noise added by the axion signal.

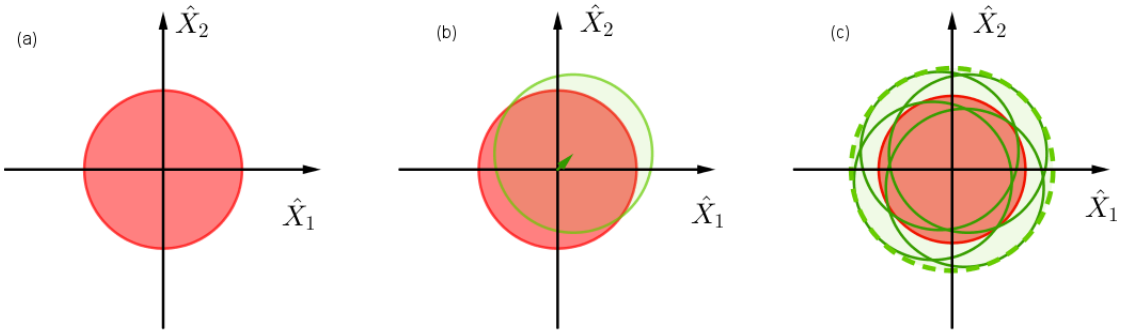

Figure 20: Pictorial view of the effect of the axion field in the phasor diagram in the cavity rotating frame. (a) The vacuum state is a state of minimal uncertainty equally distributed on the two quadratures. (b) The axion field acts displacing the vacuum state. (c) The phase of the axion field changes randomly on the time scale of the axion coherence time $\tau_a \approx 100\mu$s so that the displacement direction has quick random jumps. The net effect is thus to increase the quadrature fluctuations with respect to one in vacuum state.

As a result of the displacement the probability of measuring the cavity field in the one photon state $|1\rangle$ increases. The interaction Hamiltonian between axion and electromagnetic fields is given by the first term in Equation 1.1.

$$\hat{H}_I = \sqrt{\frac{\epsilon_0}{\mu_0}}\int d^3\mathbf{x} a\mathbf{E}\cdot\hat{B} \tag{4.9}$$

Considering the applied magnetic field $\mathbf{B} = B_0\hat{\mathbf{z}}$ the $|0\rangle \to |1\rangle$ transition probability can be evaluated from the Fermi golden rule [49]

$$\begin{aligned} P &\approx \left|\frac{1}{\hbar}\langle 0|\int_0^t \hat{H}_I dt'|1\rangle\right|^2 \\ &\approx g_{a\gamma\gamma}^2 \frac{\rho_a c^3}{\omega_a^2}\frac{B_0^2}{\mu_0}\sum_k \omega_k \left|\int d\mathbf{x}\epsilon_0 \mathbf{U}_k^*\cdot\hat{\mathbf{z}}\right|^2 \frac{\sin^2[(\omega_k-\omega_a)t/2]}{4[(\omega_k-\omega_a)/2]^2} \end{aligned} \tag{4.10}$$

For t large enough $\sin^2[(\omega_k-\omega_a)t/2]/[(\omega_k-\omega_a)/2]^2 \approx 2\pi t\delta(\omega_k-\omega_a)$. The functions $\mathbf{U}_k$ are normalized

according to the scalar product defined in Equation 3.6 so

$$\left| \int d\mathbf{x} \epsilon_0 \mathbf{U}_k^* \cdot \hat{\mathbf{z}} \right|^2 = V \frac{\left| \int d\mathbf{x} \epsilon_0 \mathbf{U}_k^* \cdot \hat{\mathbf{z}} \right|^2}{V \int d\mathbf{x} \epsilon_0 \epsilon(\mathbf{x}) |\mathbf{U}_k|^2} = V C_k \tag{4.11}$$

with C_k the form factor of the mode k. The sum over the modes can be approximated with an integral weighted on the mode density $\mathcal{D}(\omega)$

$$\sum_k C_k \omega_k \delta(\omega_k - \omega_a) \approx \int d\omega \mathcal{D}(\omega) C_\omega \omega \delta(\omega_k - \omega_a) \approx C_{\omega_a} \frac{1}{\Delta\omega_{cav}} \omega_a = C_{\omega_a} Q_L \tag{4.12}$$

The transition rate is $R = \frac{dP}{dt}$ and the corresponding power transmitted to the antenna is $P_{a\gamma\gamma} = \frac{\beta}{1+\beta} \hbar \omega_a R$, the resulting expression is analogues to the one in Equation 4.2

$$P_{a\gamma\gamma} = g_{a\gamma\gamma}^2 \rho_a \hbar c^3 \frac{\beta}{1+\beta} \frac{B_0^2}{\mu_0} V C_{\omega_a} Q_L \tag{4.13}$$

Describing the evolution of the system in the Heisenberg picture we can consider the state fixed in the initial vacuum state and study the evolution of the annihilation operator $\hat{a}$ of the mode at frequency ω_a. The Hamiltonian of the system is

$$\begin{aligned} &\hat{H} = \hat{H}_0 + \hat{H}_I \\ &= \hbar \omega_a \left(\hat{a}^\dagger \hat{a} + \frac{1}{2} \right) + i\hbar g \hat{a} \left(A_0 e^{i\omega_a t} + A_0^* e^{-i\omega_a t} \right) + i\hbar g^* \hat{a}^\dagger \left(A_0 e^{i\omega_a t} + A_0^* e^{-i\omega_a t} \right) \\ &g \equiv \sqrt{\frac{\epsilon_0 \omega_a}{4\mu_0}} \int d^3\mathbf{x} \mathbf{U} \cdot \mathbf{z} \hat{B}_0 \end{aligned} \tag{4.14}$$

where A_0 is defined from Equation 4.5. The Heisenberg-Langevin equation is then [13]

$$\begin{aligned} \frac{d\hat{a}}{dt} &= \frac{i}{\hbar} \left[\hat{H}_0, \hat{a} \right] + \frac{i}{\hbar} \left[\hat{H}_I, \hat{a} \right] - \frac{\kappa}{2} \hat{a} \\ &= -i\omega \hat{a} + g^* \left(A_0 e^{i\omega_a t} + A_0^* e^{-i\omega_a t} \right) \hat{\mathbf{1}} - \frac{\kappa}{2} \hat{a} \end{aligned} \tag{4.15}$$

with κ the total cavity decay rate accounting for losses and decay through the measurement port, $\hat{\mathbf{1}}$ the identity operator. The equation is more easily solved in the cavity rotating frame, that means by doing the change of variable $\hat{a}' = \hat{a} e^{i\omega_a t}$

$$\frac{d\hat{a}'}{dt} = \cancel{g^* A_0 e^{2i\omega_a t}} + g^* A_0^* \hat{\mathbf{1}} - \frac{\kappa}{2} \hat{a}' \tag{4.16}$$

The rotating wave approximation consist of neglecting the fast oscillating terms. The steady state solution $\frac{d\hat{a}'}{dt} = 0$ gives

$$\hat{a}' = \frac{2g^*}{\kappa} A_0^* \hat{\mathbf{1}} \tag{4.17}$$

As mentioned above the effect of the axion field is to bring the system from the vacuum state to a one with non null expected number of photons

$$\langle \hat{N} \rangle = \langle \hat{a}'^\dagger \hat{a}' \rangle = \frac{4|g|^2}{\kappa^2} |A_0|^2 \tag{4.18}$$

4.2 Linear amplifier and power receiver

The cavity oscillating field induces currents in the antenna producing a signal that propagates through the transmission line connected to it. A classical narrow-band signal $V(t)$ can be described be decomposed

in the sum of two slowly varying functions $X_1(t)$ and $X_2(t)$ modulated at the carrier frequency.

$$V(t) = X_1(t)\cos(2\pi\nu t) + X_2(t)\sin(2\pi\nu t) \tag{4.19}$$

where the time scale on which X_1 and X_2 vary is given by the reciprocal of the signal bandwidth $t = \frac{1}{\Delta\nu}$. In the most commonly used haloscope scheme, this signal is amplified by a linear amplification chain. The amplified signal is demodulated by mixing it with a Local Oscillator (LO) in an IQ mixer that separates the two quadratures. The two demodulated quadratures are digitized with an Analog to Digital Converter (ADC) and Fourier transformed to compute the power spectrum of the signal. Many spectra are averaged to reduce fluctuations [48].

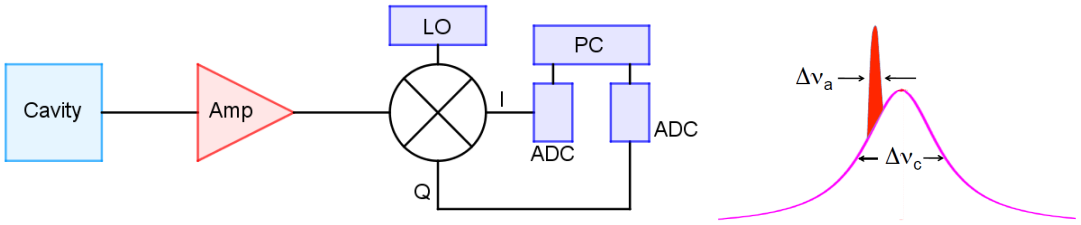

Figure 21: Principal components of the heterodyne detection scheme. The signal is amplified and divided into its two quadratures with an I Q mixer. The I and Q signals are digitaized ad Fourier transformed to compute the signal spectrum. The axion signal is searched as an excess power in a portion of the spectrum.

The amplification chain adds noise to the measurement. The added noise is generally stated by referring it to the amplifier input which means treating the system as if the amplifier was noiseless and a noise source increases the noise level at the input of the amplifier. The amplification is usually performed with more than one amplification stage, however, the noise performance of the amplification chain mainly depends on the first amplifier. Indeed the noise added in later stages is amplified only by a portion of the chain and is thus generally negligible with respect to the one added in the first stage. The voltage noise fluctuations at the output of a haloscope readout line have a Gaussian distribution as would be in the case of Johnson thermal noise produced by a load at a finite temperature. So, noise power is usually expressed in terms of an equivalent noise temperature T_{sys}. This is defined by ideally substituting the system with a fictitious load at temperature T_{sys} and that the noise produced by this load is amplified by an ideal noiseless amplification chain with the same gain as the real one. The noise power produced by the load in a bandwidth $\Delta\nu$ is [1] [50]

$$P_N = k_B T_{sys} \Delta\nu \tag{4.20}$$

The quantum mechanical treatment of the signal usually consist in promoting the the two quadratures to operators $\hat{X}_1$ and $\hat{X}_2$ with the commutation relation $\left[\hat{X}_1, \hat{X}_2\right] = \frac{i}{2}$ that behaves as position and momentum of a quantum harmonic oscillator. The state of this oscillator is strongly related to the one of cavity field. When the system is at temperature T the equivalent noise temperature is

$$k_B T_{sys} = h\nu \left(\frac{1}{e^{h\nu/k_B T} - 1} + \frac{1}{2} + N_a \right) \tag{4.21}$$

The first term in the parenthesis is the average number of blackbody photons unit bandwidth and for T at the mK level gives a negligible contribution. The $\frac{1}{2}$ term comes from vacuum fluctuations of the cavity field and N_a accounts for the amplifier added noise. The SQL implies that $k_B T_{sys} \geq h\nu$ [51] (see Appendix A). At this limit the noise power in an axion bandwidth is $P_{NSQL} \sim 3 \times 10^{-20}$ W this is about three orders of magnitude greater than the excess power expected from the axion. This means that in

[1] This expression is in principle correct only in the Rayleigh–Jeans approximation $K_B T \gg h\nu$. However, since the equivalent load is just an ideal model this expression can be used to define the noise equivalent temperature also at the SQL where $k_B T_{sys} = h\nu$.

order to detect an axion signal the noise power needs to be measured with an uncertainty smaller than a part in a thousand.
The power measured from a single spectrum has a χ^2 distribution, however since many spectra are averaged the distribution can be approximated as Gaussian [48]. The standard deviation of the distribution of the power measured in an axion linewidth is given by [6]

$$\delta P_N = k_B T_{sys} \sqrt{\frac{\Delta\nu_a}{\tau}} \tag{4.22}$$

Whit τ the total integration time. The Signal to Noise Ratio (SNR) Σ is then given by the Dicke radiometer equation

$$\Sigma = \frac{P_{sig}}{k_B T_{sys}} \sqrt{\frac{\tau}{\Delta\nu_a}} \tag{4.23}$$

A long integration time allows to improve the SNR, however, the long term stability of the system sets a limit on the maximum integration time. Indeed any experimental system on sufficiently long time scales is subjected to drifts in some of its parameters that in this case brings to fluctuation of the average noise power in the long term. Thus Equation 4.22 is valid only up to a certain maximum integration time. During a measurement the whole cavity bandwidth $\Delta\nu_c = \Delta\nu_a \frac{Q_a}{Q_L}$is simultaneously probed, so from Equation 4.23 the scan rate R for a given sensitivity and a given SNR can be estimated to be

$$R \equiv \frac{d\nu}{dt} \approx \frac{\Delta\nu_c}{\tau} = \frac{Q_a}{Q_L} \frac{P_{a\gamma\gamma}^2}{k_B^2 T_{sys}^2 \Sigma^2} = \frac{g_{a\gamma\gamma}^4 \rho_a^2 \hbar^2 c^6}{k_B^2 T_{sys}^2 \Sigma^2} \frac{\beta^2}{(1+\beta)^2} \frac{B_0^4}{\mu_0^2} V^2 C_{nml}^2 \frac{Q_L Q_a^3}{(Q_L + Q_a)^2} \tag{4.24}$$

From Equation 4.2 one finds that the signal power is maximized for a critically coupled antenna $\beta = 1$, the highest scan rate is instead achieved for $\beta = 2$. Overcoming the antenna has indeed the effect of lowering the loaded quality factor, on one hand reducing the signal but on the other increasing the cavity resonance so that a wider range is simultaneously probed.

4.3 Beyond standard quantum limit

4.3.1 Squeezing

A strategy that has been employed to circumvent the SQL is to prepare the cavity field in a squeezed vacuum state. In a squeezed vacuum the fluctuations in one of the two field quadrature are reduced and the one in the other is enhanced as a consequence of the Heisenberg uncertainty principle. Since an axion-like signal increases evenly the fluctuations in the two quadratures, the squeezed one will present an improved signal to noise ratio. The benefit of this strategy is that it allows to overcouple the antenna to the measurement port without losing sensitivity. Increasing the coupling enlarges the cavity resonance so that a wider bandwidth is simultaneously probed enhancing the scan rate. A scan rate improvement of a factor 2.12 ± 0.08 was demonstrated by applying this method in [13].

4.3.2 Photon counter

A photon counter would overcome the limit switching from the measurement of the two quadratures $\hat{X}_1$, $\hat{X}_2$ to the one of the photon number operator $\hat{N}$. The information about the signal phase is lost in the measurement so the uncertainty of the photon number can be reduced without a fundamental limit. Indeed, the average thermal population of the cavity mode is give by

$$\overline{n}(T) = \frac{1}{e^{h\nu/k_B T} - 1} \underset{k_B T \ll h\nu}{\sim} e^{-\frac{h\nu}{k_B T}} \tag{4.25}$$

So it can in principle be arbitrarily reduced by lowering the temperature. The effect of an axion signal

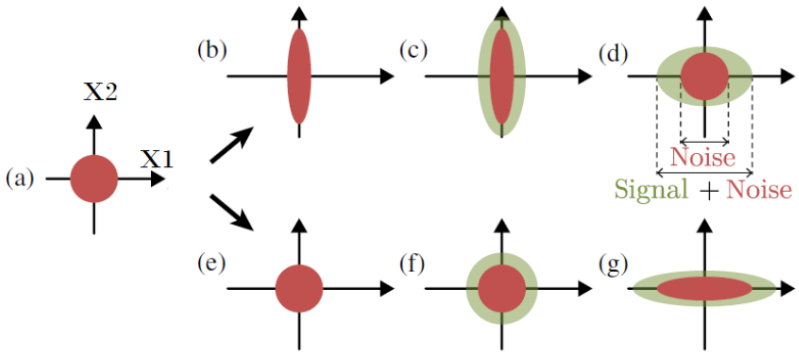

Figure 22: In the squeezed state fluctuations in the $\hat{X}_1$ quadrature are reduced and the one in the $\hat{X}_2$ are enhanced. The axion signal increases evenly the fluctuations in both quadratures. After amplification, the signal to noise ratio in the $\hat{X}_1$ quadrature is improved with respect to what would be obtained without squeezing [13]

would be in this case to increase the photon counting rate by

$$\Gamma_{sig} = P_{a\gamma\gamma}/h\nu_a \tag{4.26}$$

An ideal photon counter can bring an exponential improvement of the scan rate with respect to the one achievable with a linear amplifier at the SQL [14]

$$\frac{R_{\text{counter}}}{R_{\text{SQL}}} \approx \frac{Q_L}{Q_a} e^{\frac{h\nu}{k_B T}} \tag{4.27}$$

At $\nu = 7\,\text{GHz}$ for instance an improvement in scan rate of a factor 1000 would be achieved by cooling the system at $T = 40\,\text{mK}$. This theoretically unlimited advantage in scan rate is the main motivation for the research of an implementation of such a scheme for haloscope readout. A photon counter doesn't have the spectral resolution needed to reconstruct the signal spectrum. For this reason, photon counters can not an exclusive alternative to linear amplifiers but the two technologies need parallel development. Any possible photon counting device will have a finite detection efficiency η and dark count rate Γ_{dc} which is the photon counting rate when there is no signal applied to the counter. These are the two most important parameters setting the level of improvement that can be achieved. Dark count processes usually have Poissonian statistics. The uncertainty in the number of dark counts collected in an integration time τ can be estimated as

$$\delta N_{dc} = \sqrt{\Gamma_{dc}\tau} \tag{4.28}$$

This contribution in general prevails over the uncertainty due to thermal photons and intrinsic shot noise of the axion signal. The SNR can be written in this case

$$\Sigma = \frac{\eta\Gamma_{sig}\tau}{\sqrt{\Gamma_{dc}\tau}} = \eta\Gamma_{sig}\sqrt{\frac{\tau}{\Gamma_{dc}}} \tag{4.29}$$

and the relative scan rate

$$R_{\text{counter}} = \frac{\Delta\nu_c}{\tau} = \frac{\Delta\nu_c \eta^2 P_{a\gamma\gamma}^2}{h^2\nu^2\Sigma^2\Gamma_{dc}} \tag{4.30}$$

For a given cavity than the ratio between the scan rate achievable with a counter over the one of linear amplification is

$$\frac{R_{\text{counter}}}{R_{\text{lin}}} = \left(\frac{k_B T_{sys}}{h\nu}\right)^2 \frac{\eta^2\Delta\nu_a}{\Gamma_{dc}} \tag{4.31}$$

The SMPD that will be employed in the pilot experiment have an efficiency $\eta \approx 0.4$ and dark count rate

$\Gamma_{dc} \approx 100\,\text{Hz}$ so Equation 4.31 gives a potential improvement of a factor 11 with respect to the SQL scan rate.

4.4 ROC curve

A tool used to evaluate the goodness of a detector is its Receiver Operating Characteristic (ROC). The ROC curve consists in plotting the probability of correctly identifying a signal True Positive Rate (TPR) against the probability of false detections False Positive Rate (FPR). These probabilities are generally a function of a threshold value used to discriminate the presence or absence of the signal.
For the case of linear amplification, the quantity used for discrimination is the power P measured with the heterodyne technique. Here we consider the optimal case in which the cavity bandwidth is comparable to the one of the axion $\Delta\nu_c \approx \Delta\nu_a$, the receiver has no calibration uncertainties and the reference noise level is known so that a discrimination threshold can be set directly on the value of the measured power P. P to has a Gaussian distribution with standard deviation given by Equation 4.22, the presence of a signal shifts the average of the distribution by P_{sig}.

$$\begin{cases} P \sim \mathcal{N}(P_N, \delta P_N) & \text{if there is no signal} \\ P \sim \mathcal{N}(P_N + P_{sig}, \delta P_N) & \text{if there is signal} \end{cases} \tag{4.32}$$

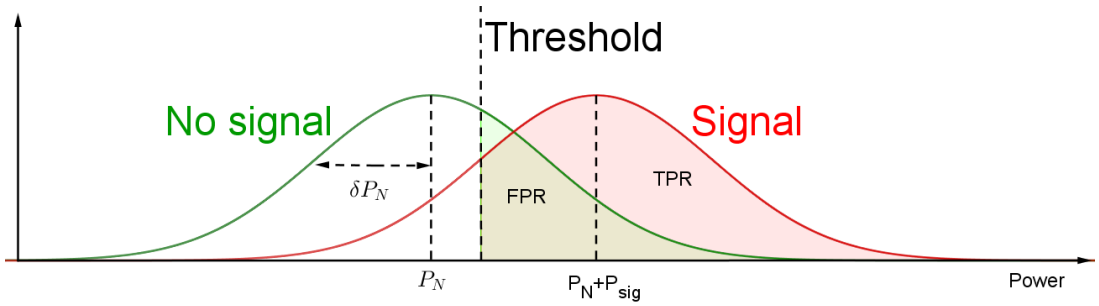

Figure 23: Distribution of the measured power in presence or absence of asignal.

Setting the threshold level to $P_{th} = P_N + t\delta P_N$, with $t \in (-\infty, +\infty)$, the ROC curve is given by

$$\begin{cases} TPR_{lin} = \frac{1}{2} - \frac{1}{2}\text{erf}\left(\frac{t\delta P_N - P_{sig}}{\sqrt{2}\delta P_N}\right) \\ FPR_{lin} = \frac{1}{2} - \frac{1}{2}\text{erf}\left(\frac{t}{\sqrt{2}}\right) \end{cases} \tag{4.33}$$

at the SQL $\delta P_N = k_B T_{sys}\sqrt{\frac{\Delta\nu}{\tau}} = h\nu\sqrt{\frac{\Delta\nu}{\tau}}$.
For a photon counter, the noise is given by the count rate in absence of any signal called the dark count rate Γ_{dc}. The number of dark counts collected in a time interval τ typically follows a Poissonian statistic. The presence of a signal can be detected by setting a threshold on the number of collected counts. For a large enough average number of counts, $\overline{n} = \tau\Gamma_{dc}$ the Poisson distribution is well approximated by a gaussian distribution with average $\overline{n}$ and standard deviation $\sqrt{\overline{n}}$. The threshold level can be chosen as $N_{th} = \Gamma_{dc}\tau + t\sqrt{\Gamma_{dc}\tau}$, $t \in (-\infty, +\infty)$. Considering also a finite detector efficiency η, the ROC curve is given by

$$\begin{cases} TPR_{count} = \frac{1}{2} - \frac{1}{2}\text{erf}\left(\frac{t\sqrt{\Gamma_{dc}\tau} - \eta P_{sig}\tau/h\nu}{\sqrt{2}\sqrt{\Gamma_{dc}\tau}}\right) \\ FPR_{count} = \frac{1}{2} - \frac{1}{2}\text{erf}\left(\frac{t}{\sqrt{2}}\right) \end{cases} \tag{4.34}$$

Figure 24 compares the curves given in Equation 4.33 and Equation 4.34 for a signal power $P_{sig}/h\nu = 7.5\,\text{Hz}$ and acquisition time $\tau = 150\,\text{s}$. The ROC of linear amplifiers is computed at the SQL and assuming

a cavity linewidth equal to the one of the axion $\Delta\nu = \Delta\nu_a$. The ROC for the counter is computed using $\Gamma_{dc} = 100\,\text{Hz}$ and $\eta = 0.4$ that are typical values for the photon detector presented in section 8.

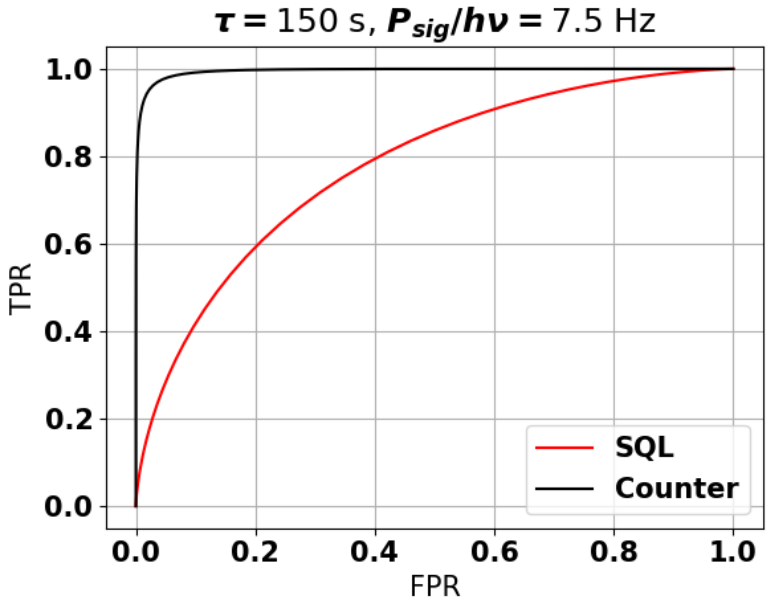

Figure 24: ROC curve computed according to a Gaussian distribution of the noise power and of the dark counts. The ROC for the linear amplifiers is computed at the SQL and assuming a cavity linewidth equal to the one of the axion $\Delta\nu = \Delta\nu_a$. The ROC for the counter is computed using $\Gamma_{dc} = 100\,\text{Hz}$ and $\eta = 0.4$ that are typical values for the photon detector presented in section 8.

The time tags collected with a photon counter give information on the arrival time of every single photon, this may bring some additional information with respect to a bear evaluation of the total number of collected counts. To capture this information we may apply a detection criterion based on the Kumar-Caroll index [52].

$$d_{kc} \equiv \frac{|\langle \Delta t \rangle_0 - \langle \Delta t \rangle_1|}{\sqrt{\frac{1}{2}[\sigma^2(\langle \Delta t \rangle_0) + \sigma^2(\langle \Delta t \rangle_1)]}} \tag{4.35}$$

Where $\langle \Delta t \rangle_1$ and $\langle \Delta t \rangle_0$ are the averages waiting times between clicks calculated respectively in a sample under test and in a reference sample with no signal, and σ^2 indicates the variance of these estimations. A discrimination threshold can be set on the value of this index. Since we are looking for an increase in the rate, the waiting time decreases in presence of a signal. So we may remove the modulus from the definition so that only events with $\langle \Delta t \rangle_1 < \langle \Delta t \rangle_0$ will be flagged. We tested this detection strategy in subsubsection 8.3.1, the index is highly correlated to the number of counts so it does not bring much additional information and it gives a ROC curve equivalent to the criteria based on the number of counts.

5 Superconducting Parametric amplifiers

Parametric amplification consists of the amplification of an oscillation with a periodic modulation of some oscillator parameter. The most famous example is the oscillation of a person on a swing that modulates its moment of inertia with respect to the pivot point, by changing position. In the case of microwave amplifiers, the modulated parameter is usually the value of some inductor. The amplifies with the best performance in terms of added noise are Josephson Parametric Amplifier (JPA) and Traveling Wave Parametric Amplifiers (TWPA). JPAs are based on Josephson junctions embedded in a microwave resonator. They can SQL added noise, however due to their resonant nature they have limited bandwidth. TWPAs consist of non-resonant nonlinear transmission lines and can reach amplification bandwidth up to a few GHz [53]. The nonlinearity can be achieved by embedding an array of Josephson junctions or loops containing Josephson junctions, in a transmission line [54]. Other devices achieve the required nonlinearity exploiting kinetic inductance in superconducting materials[55]. Figure 25 schematize a nonlinear transmission line.

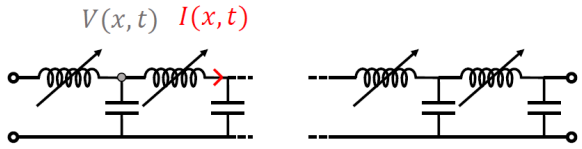

Figure 25: Scheme of a transmission line with modulable inductance.

The wave equation for the current propagating through the line is

$$\frac{\partial^2 I}{\partial x^2} - \frac{\partial}{\partial t}\left(L_l(I) C_l \frac{\partial I}{\partial t}\right) = 0 \tag{5.1}$$

Where C_l is the capacitance per unit length and $L_l(I)$ is the current dependent inductance per unit length

$$L_l(I) = L_0[1 + \epsilon I + \zeta I^2 + O(I^3)] \tag{5.2}$$

For a dispersive transmission line, L_0 and C_l depend on the frequency of the wave. In the three-wave mixing process a pump tone, with angular frequency ω_p is used to modulate the inductance and amplify a signal at ω_s. As a byproduct of the amplification, an idler signal is produced with $\omega_i = \omega_p - \omega_s$. For this process is sufficient to consider the first order non linearity and one can look for a solution of the kind

$$\begin{aligned} &I(x,t) = I_p(x)e^{i(k_p x - \omega_p t)} + I_s(x)e^{i(k_s x - \omega_s t)} + I_i(x)e^{i(k_i x - \omega_i t)} + \text{c.c.} \\ &k_j = \omega_j \sqrt{L_0(\omega_j) C_l(\omega_j)} \qquad j \in \{p, s, i\} \end{aligned} \tag{5.3}$$

where $I_j(x)$ are slowly varying functions such that $\left|\frac{d^2 I_j}{dx^2}\right| \ll \left|\frac{dI_j}{dx}\right|$ Substituting this expression in Equation 5.1 and collecting separately terms at the three different angular frequencies one finds

$$\begin{aligned} \frac{dI_p}{dx} &= \frac{i\epsilon k_p}{2} I_s I_i e^{i\Delta k x} \\ \frac{dI_s}{dx} &= \frac{i\epsilon k_s}{2} I_p I_i^* e^{-i\Delta k x} \\ \frac{dI_i}{dx} &= \frac{i\epsilon k_i}{2} I_p I_s^* e^{-i\Delta k x} \end{aligned} \tag{5.4}$$

where $\Delta k \equiv k_s + k_i - k_p$. Considering that the power transported by each wave is proportional to the square modulus of the complex representation of the current $P_j \propto |I_j|^2$, from Equation 5.4 one can derive

the Manley-Rowe relation[56].

$$\frac{d}{dx}\left(\frac{P_s}{\hbar\omega_s}\right) = \frac{d}{dx}\left(\frac{P_i}{\hbar\omega_i}\right) = -\frac{d}{dx}\left(\frac{P_p}{\hbar\omega_p}\right) \tag{5.5}$$

This relation gives a clear intuition of how the system can be described quantum mechanically as a flux of pump photons that decay into photos photos at signal and idler frequency. If the pump tone is strong one can assume that it is not depleted during the amplification. As shown in Appendix B in this approximation the complex amplitude of the signal current is given by

$$I_s = \sqrt{k_s} I_{s0} \left(\frac{g + \frac{i\Delta k}{2}}{2g} e^{gx} + \frac{g - \frac{i\Delta k}{2}}{2g} e^{-gx} \right) e^{-i\frac{i\Delta k}{2}x} \tag{5.6}$$

where $g \equiv \sqrt{|K| - \frac{\Delta k^2}{4}}$ and $K \equiv \frac{i\epsilon\sqrt{k_i k_s} I_p}{2}$. As shown in Figure 26 if $\Delta k < 2|K| = \epsilon |I_p| \sqrt{k_s k_i}$ then $|I_s|$ is exponentially amplified and the gain is maximum for $\Delta k = 0$. If instead $\Delta k > 2|K|$, g becomes imaginary and I_s starts to oscillate. The condition $\Delta k = 0$ is called perfect phase matching. Higher order nonlinearity enables the 4 wave mixing process in which two pump photons are converted into a signal and an idler photon $2\omega_p = \omega_s + \omega_i$. Both in 3 wave mixing and 4 waves mixing TWPAs the phase matching condition required is usually achieved with careful engineering of the dispersion relation. A phase matching mechanism based on reversed Kerr effect was demonstrated in [54], this mechanism has the advantage of avoiding gaps in the transmission spectra and reducing gain ripples. This type of amplifier is the one currently employed for the first amplification stage in the QUAX setup.

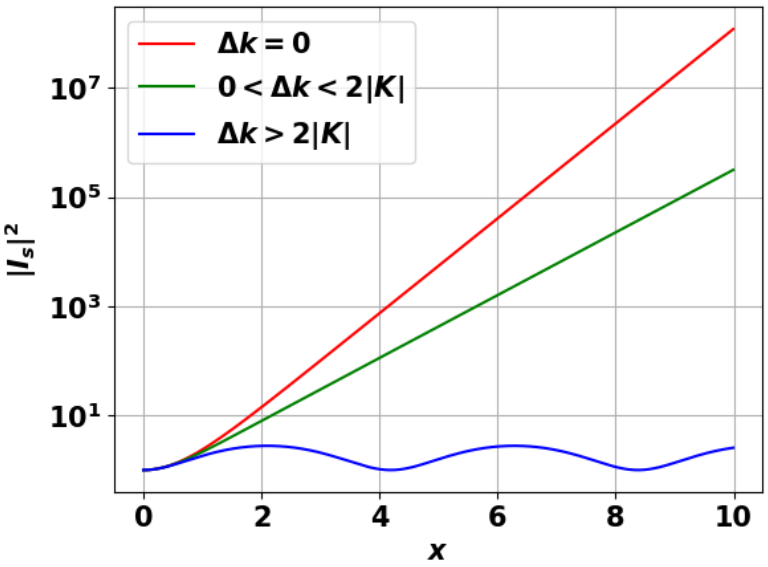

Figure 26: Amplification gain for different values of wavevector mismatch.

5.1 Equivalent noise temperature measurement

We performed a measurement of the equivalent noise temperature T_{sys} of the amplification chain present at the moment in the haloscope setup at LNL. Figure 27 shows the low-temperature electronics of the setup. The cavity in this setup resonates at $\nu_c \sim 10.35\,\text{GHz}$. Line L1 is connected to an antenna weakly coupled to the cavity. The signals injected through line L3 are directed with a circulator to the movable antenna used to pick up the signal from the cavity. The same circulator directs the signals coming from the cavity to readout line L4. The first amplification stage is performed by a 4 wave mixing TWPA, the signals are further amplified with a cryogenic Hig Electron Mobility Transistor (HEMT) and with a room temperature HEMT (not shown in the figure). The pump tone is provided through line L3 and reaches

the TWPA after reflecting on the cavity. The measurement of T_{sys} proceeds as described in [8] and is referred to the point A1 on the antenna where the three lines joins.

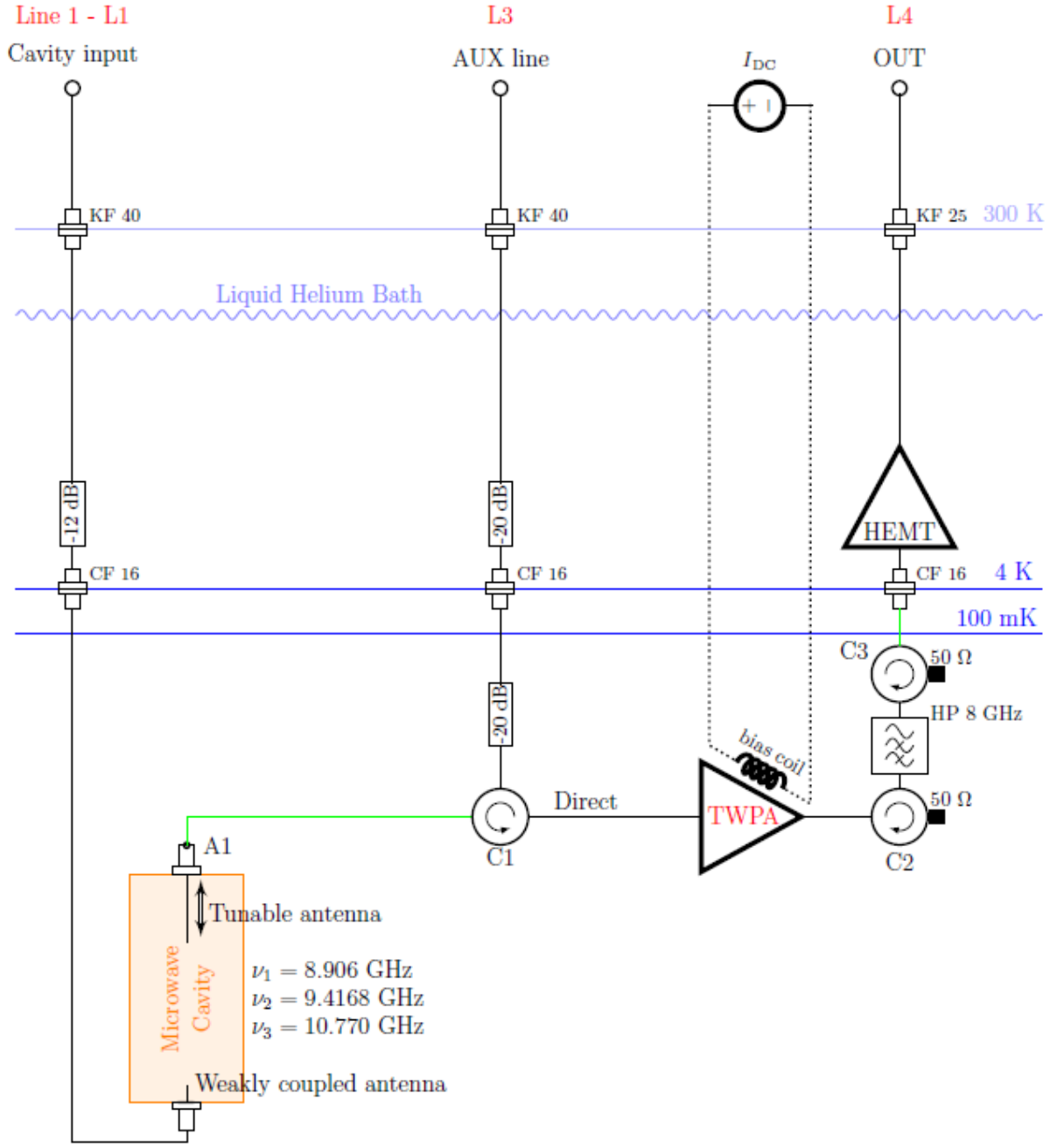

Figure 27: Layout of cryogenic apparatus. Green cables are superconducting (NbTi). The point A1 is the reference point for the measurement of the system noise temperature. The tunable antenna is almost critically coupled to the cavity [8].

Calling P1 the point at the input of line L1, P3 the one at the input of line L3 and P4 the point at the end of line L4 after all the amplification stages, the measurement consist in the acquisition of the following three transmission power spectra:

- S41: From P1 to P4.
- S13: From P3 to P1.
- S43: From P3 to P4.

The first two measurement are performed at the cavity resonant frequency. To go from P3 to P4 the signal has to reflect on the cavity so S43 is measured twice at the frequencies $\nu_c \pm \delta\nu$, with $\delta\nu = 200\,\text{kHz}$

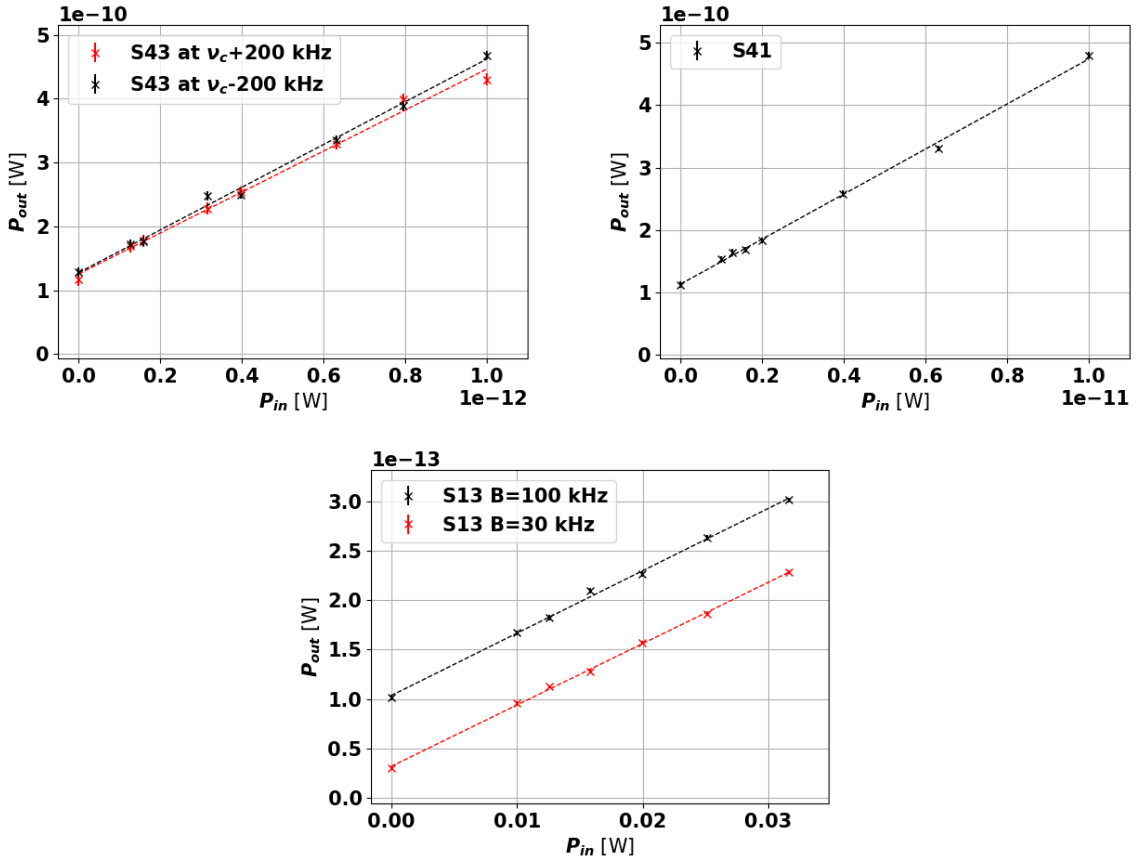

Figure 28: P_i vs P_o in the three transmission measurements. Top left S43, top right S43, bottom S31. The transmission S31 was measured once with a resolution bandwidth of 100 kHz and another with 30 kHz. Both measurements gives similar values for G_{13}.

and the computed quantities are then averaged between the two measurements. The frequency dependent line gains are defined as

- $g_1(\nu)$: from the point P1 to antenna A1 - bidirectional
- $g_3(\nu)$: from the point P3 to antenna A1 - bidirectional
- $g_4(\nu)$: from antenna A1 to the point P4 (Complete de- tection chain)

A pure tone of power P_i is injected on one of the lines by a calibrated signal generator and the output power P_o is measured with a Spectrum Analyzer (SA). P_i and P_o are related by

$$P_o^{xy} = P_n + P_i G_{xy} \quad xy \in \{41, 13, 43\} \tag{5.7}$$

where $G_{xy} = g_x \times g_y$ and P_n is the noise power that can be expressed as

$$P_n = g_4 k_B T_{sys} B \tag{5.8}$$

Where B is the resolution bandwidth of the SA when measuring the output power from P4. A linear fit of P_o vs P_i along the three different path provides estimations of $G_{xy} \quad xy \in \{41, 13, 43\}$ from which we can compute g_1, g_3,g_4. The noise power P_n is evaluated as the power measured by the SA at point P4 when there is no input signal. Figure 28 shows the fits of the measurements and the results are reported in Table 6. The SQL noise temperature for $\nu = 10.35\,\text{GHz}$ is $T_{SQL} = 0.5\,\text{K}$ thus the noise temperature of our amplification line is about 4 times the value at SQL.

Table 6: Parameters estimated from the fits. G_{43} is the average valued over the two measurements at $\nu_c \pm \delta\nu$, G_{41} is averaged over the two measurements with different resolution bandwidth.

G_{41}	36±1	g_1	$(8.3 \pm 0.1) \times 10^{-7}$
G_{13}	$(6.2 \pm 0.1) \times 10^{-12}$	g_3	$(7.5 \pm 0.1) \times 10^{-6}$
G_{43}	(327 ± 6)	g_4	$(4.35 \pm 0.06) \times 10^{7}$
P_n^{43}	$(1.22 \pm 0.07) \times 10^{-10}\,\mathrm{W}$	P_n^{41}	$(1.12 \pm 0.05) \times 10^{-10}\,\mathrm{W}$
T_{sys}^{43}	$2.0 \pm 0.1\,\mathrm{K}$	T_{sys}^{41}	$1.9 \pm 0.1\,\mathrm{K}$

6 Qubit dynamics and control

6.1 Bloch sphere

The state of a qubit is conveniently represented as a vector in the Bloch sphere. This representation start from the fact that the density matrix $\hat{\rho}$ of a two-level system can be written as

$$\hat{\rho} = \frac{1}{2}(\hat{\mathbf{1}} + R_x\hat{\sigma}_x + R_y\hat{\sigma}_y + R_z\hat{\sigma}_z) \tag{6.1}$$

where $\hat{\mathbf{1}}$ is the 2×2 identity matrix and $\hat{\sigma}_{x,y,z}$ are the Pauli matricies. $\mathbf{R}$ is the Bloch vector and it satisfies $|\mathbf{R}|^2 = R_x^2 + R_y^2 + R_z^2 \leq 1$, where the equal sign holds if and only if the state is pure. So there is a one-to-one relation between qubit states and the vectors in the unitary radius sphere. The points where the surface of the sphere intersects the axis x y and z corresponds to the eigenstates of $\hat{\sigma}_x$ $\hat{\sigma}_y$ and $\hat{\sigma}_z$.

6.2 Non unitary evolution

The temporal evolution of a quantum subsystem in contact with the environment is in general non unitary. The most general linear differential equation for the density matrix that preserve its proprieties is the Lindblad master equation [21]

$$\frac{d\hat{\rho}}{dt} = -\frac{i}{\hbar}\left[\hat{H}, \hat{\rho}\right] + \sum_a 2\hat{L}_a\hat{\rho}\hat{L}_a^\dagger + \hat{L}_a^\dagger\hat{L}_a\hat{\rho} + \hat{\rho}\hat{L}_a^\dagger\hat{L}_a \tag{6.2}$$

where $\hat{H}$ is the hermitian subsystem Hamiltonian and $\hat{L}_a$ are arbitrary operators that describe the interaction with the environment. For a qubit with unperturbed Hamiltonian $\hat{H} = -\hbar\omega\hat{\sigma}_z/2$ the first term gives a precession of the Bloch vector around the z axis and is generally removed moving to the qubit rotating frame, that means by studying the evolution $\hat{\rho}_I = e^{i\hat{H}t/\hbar}\hat{\rho}e^{-i\hat{H}t\hbar}$.
The Lindblad operators that describe the noise a qubit is usually subjected to are

$$\begin{aligned}
\hat{L}_1 = \hat{L}_1^\dagger &= \sqrt{\Gamma_\phi}\hat{\sigma}_+\hat{\sigma}_- = \sqrt{\Gamma_\phi}\begin{pmatrix} 1 & 0 \\ 0 & 0 \end{pmatrix} \\
\hat{L}_2 &= \sqrt{\Gamma_1/2}\hat{\sigma}_- = \sqrt{\Gamma_1/2}\begin{pmatrix} 0 & 0 \\ 1 & 0 \end{pmatrix} \\
\hat{L}_3 &= \sqrt{\Gamma_1/2}\hat{\sigma}_+ = \sqrt{\Gamma_1/2}\begin{pmatrix} 0 & 1 \\ 0 & 0 \end{pmatrix}
\end{aligned} \tag{6.3}$$

where Γ_ϕ is the pure dephasing rate and Γ_1 is the energy relaxation rate. The first is responsible for pure dephasing of the state, this noise is usually called longitudinal noise since $\hat{L}_1$ is diagonal, this noise causes fluctuations of the qubit frequency. As pictorially represented in Figure 29 (c), its effect is to add uncertainty on the angular position of the Bloch vector in the transverse (xy) plane.The other two are responsible for the transverse noise wich consist in the energy exchanges between the qubit and the environment. The effect of this noise is relaxation of the qubit state along the longitudinal (z) axis as shown in Figure 29 (b). The solution of the Lindblad master equation accounting for all three operators is then

$$\hat{\rho}(t) = \begin{pmatrix} \overline{\rho_{00}} + (\rho_{00}(0) - \overline{\rho_{00}})e^{-\Gamma_1 t} & \rho_{01}(0)e^{-(\Gamma_1/2+\Gamma_\phi)t} \\ \rho_{10}(0)e^{-(\Gamma_1/2+\Gamma_\phi)t} & \overline{\rho_{11}} + (\rho_{11}(0) - \overline{\rho_{11}})e^{-\Gamma_1 t} \end{pmatrix} \tag{6.4}$$

where $\overline{\rho_{00}}$ and $\overline{\rho_{11}}$ are the values in the stationary state solution and $\rho_{i,j}(0)$ are the initial conditions. The longitudinal relaxation time is $T_1 \equiv \frac{1}{\Gamma_1}$, while the transverse relaxation time gets a contribution both from pure dephasing and from energy relaxation $T_2 \equiv \frac{1}{\Gamma_2} \equiv \frac{1}{\Gamma_\phi + \Gamma_1/2}$.

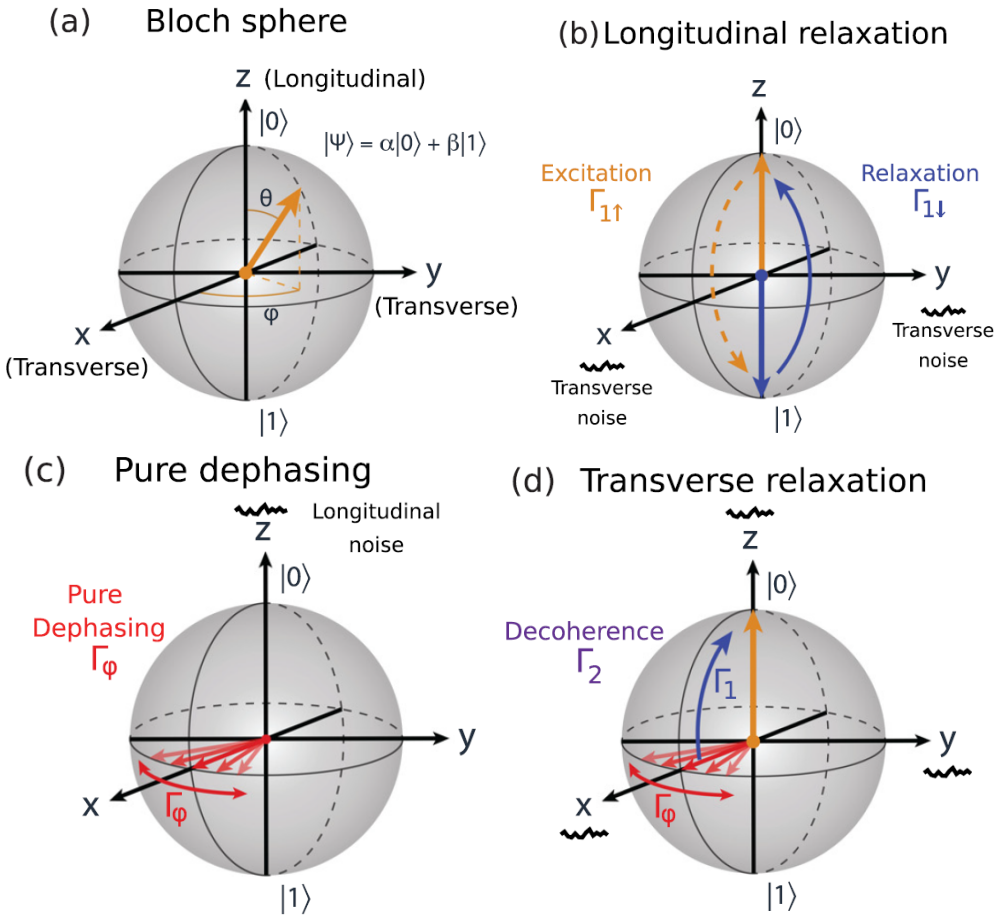

Figure 29: (a) Block sphere representation of a qubit state. The longitudinal axis refers to the z-axis, and the transverse plane refers to the xy-plane. (b) The exchange of energy between the qubit and the environment brings to excitations or relaxations of the qubit. The result is that the longitudinal component of the Bloch vector evolves toward its value in the equilibrium state. (c) Longitudinal noise is responsible for stochastic fluctuations of the transverse component of the Bloch vector. (d) The decoherence rate $\Gamma_2 = \Gamma_\phi + \Gamma_1/2$ at which decay the off-diagonal component of the density matrix gets a contribution both from pure dephasing and energy relaxation. [25]

6.3 Rabi oscillations

Applying a periodic perturbation $\hat{H}_1 = \hbar\eta\cos(\omega t)\hat{\sigma}_x$ with angular frequency close to the qubit frequency ω_q, $\omega - \omega_q \equiv \delta \ll \omega$, the Bloch vector starts to rotate with angular frequency η around an axis that slowly rotates in the xy plane with angular frequency δ. Considering for simplicity the case in which the qubit undergoes no dissipation, the evolution equation

$$\frac{d\hat{\rho}}{dt} = \frac{1}{i\hbar}\left[\hat{H}_0 + \hat{H}_1, \hat{\rho}\right] = \frac{1}{i}\left[-\omega_q\frac{\hat{\sigma}_z}{2} + \eta\cos(\omega t)\hat{\sigma}_x, \hat{\rho}\right] \tag{6.5}$$

can be expressed in terms of the Bloch vector as

$$\frac{d\mathbf{R}}{dt} = \begin{pmatrix} 0 & -\omega_q/2 & 0 \\ -\omega_q/2 & 0 & -2\eta\cos(\omega t) \\ 0 & 2\eta\cos(\omega t) & 0 \end{pmatrix}\mathbf{R} \equiv \mathbf{M}\mathbf{R} \tag{6.6}$$

Moving to the qubit rotating frame $\mathbf{R}_I = \mathbf{U}(t)\mathbf{R}$, with

$$\mathbf{U}(t) = \begin{pmatrix} \cos(\omega_q t) & \sin(\omega_q t) & 0 \\ -\sin(\omega_q t) & \cos(\omega_q t) & 0 \\ 0 & 0 & 1 \end{pmatrix} \tag{6.7}$$

Equation 6.6 becomes

$$\frac{d\mathbf{R}_I}{dt} = \mathbf{M}_I \mathbf{R}_I$$
$$\mathbf{M}_I = \begin{pmatrix} 0 & 0 & \eta[\sin(2\omega_q+\delta)t - \sin\delta t] \\ 0 & 0 & -\eta[\cos(2\omega_q+\delta)t - \cos\delta t] \\ -\eta[\sin(2\omega_q+\delta)t - \sin\delta t] & \eta[\cos(2\omega_q+\delta)t - \cos\delta t] & 0 \end{pmatrix} \tag{6.8}$$

In the rotating wave approximation the fast rotating terms at frequency $2\omega_q + \delta$ can be neglected and the equation become

$$\frac{d\mathbf{R}_I}{dt} \approx \mathbf{Y}(t) \times \mathbf{R}_I \qquad \mathbf{Y}(t) = -\eta \begin{pmatrix} \cos(\delta t) \\ \sin(\delta t) \\ 0 \end{pmatrix} \tag{6.9}$$

This equation describes the rotation of the vector $\mathbf{R}_I$ with angular velocity $\mathbf{Y}$. The vector $\mathbf{Y}$ slowly rotates in the xy plane with angular frequency δ. Equivalently, the evolution can be seen in the rotating frame at the perturbation frequency ω as the rotation of the Bloch vector with angular velocity $\mathbf{Y}' = (\eta, 0, \delta)^T$ that is the combination of a rotation around the x-axis at frequency η and a rotation around the z-axis at frequency δ.

For a superconducting qubit, the perturbation $\hat{H}_1$ can be obtained by applying a tone at frequency ω to the qubit. To rotate the qubit state by an angle α along a meridian a pulse is applied with amplitude $\hbar\eta$ and duration τ_p such that $\eta\tau_p = \alpha$. The most commonly used pulses are the ones for which $\alpha = \pi$ and $\alpha = \pi/2$. The first inverts of the qubit state while the latter brings the qubit to a superposition state. For fast operation, one wants to minimize the pulse duration, however short pulses at high intensity can produce unwanted excitation of higher modes of the circuit.

6.4 Ramsey interferometry

The Ramsey sequence is used to measure the qubit decoherence time T_2. In this sequence the qubit is initialized in the ground state $|0\rangle$. A $\pi/2$ pulse brings the state on the Bloch sphere equator. The $\pi/2$ pulse frequency is slightly detuned by $\delta = \omega - \omega_q$ from the qubit frequency so that, in the pulse rotating frame, the Bloch vector rotates around the z axis. After a waiting time τ a second $\pi/2$ pulse is applied and the qubit state is measured after the pulse. Due to the Bloch vector rotation the probability of measuring the qubit in the excited state oscillates with angular frequency δ as shown in Figure 30. Indeed for instance after a time $\tau = \pi/\delta$ the vector has rotated half of the equator and the second $\pi/2$ pulse brings it back to ground state, wile after a time $\tau = 2\pi/\delta$ the vector completes a full rotation and the second $\pi/2$ pulse brings it to the excited state. As discussed in subsection 6.2 one of the effects of noise is to progressively add uncertainty on the angular position of the Bloch vector. So the probability oscillations are damped on the time scale of the coherence time T_2^*.

$$p(\tau) = Ae^{-(\tau/T_2^*)^n}(\cos(\delta\tau + \phi)) + B \tag{6.10}$$

Where the $*$ indicates that the Ramsey experiment is sensitive to "inhomogeneous broadening." That is, it is highly sensitive to quasistatic, low-frequency fluctuations that are constant within experimental trial, but vary from trial to trial.[25] Moreover if coherent noise processes take place, as for instance slow drifts in the qubit frequency the exponent n can be greater than 1 [57].

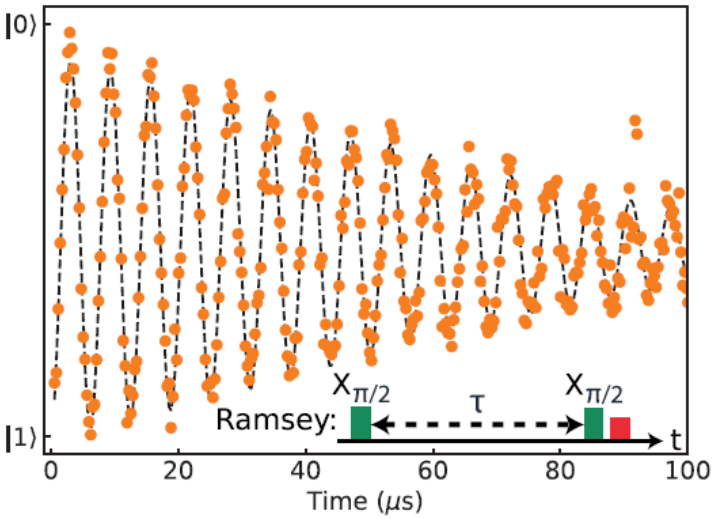

Figure 30: Ramsey sequence. The qubit is inizialided in the ground state $|0\rangle$. A $\pi/2$ brings the state to the equator of the Bloch sphere. After a time τ is applied a second $\pi/2$ pulse is applied and the qubit state is measured after the pulse. Varying the time delay τ the probability of measuring the excited state oscillates at the detuning frequency $\delta = \omega - \omega_q$ and the oscillation is exponentially damped on the decoherence time T_2^*. [25]

6.5 Dispersive coupling

When a transmon qubit is placed in proximity to a resonator, the charges of one element can influence those of the other through a coupling capacitor. The general Hamiltonian describing the interaction between a superconducting qubit and a single-mode microwave field can be written as [16] [2]

$$\frac{\hat{H}}{\hbar} = \omega_r \left(\hat{a}^\dagger \hat{a} + \frac{1}{2}\right) + \frac{\omega_q}{2}\hat{\sigma}_z + g_z \hat{\sigma}_z(\hat{a} + \hat{a}^\dagger) + g_x(\hat{\sigma}_+ + \hat{\sigma}_-)(\hat{a} + \hat{a}^\dagger) \tag{6.11}$$

Where $\hat{a}$ and $\hat{a}^\dagger$ are the annihilation and creation operators of the resonator mode at frequency ω_r, g_x and g_z are the transverse and longitudinal coupling strength respectively. When the photon energy is not to much different from the qubit transition energy $|\Delta_{qr}| \equiv |\omega_q - \omega_r| \ll (\omega_q + \omega_r)$ we can neglect the terms $\hat{\sigma}_z(\hat{a} + \hat{a}^\dagger)$, $\hat{\sigma}_+\hat{a}^\dagger$ and $\hat{\sigma}_-\hat{a}$ that do not conserve the number of excitations. We then obtain the simplified Jaynes–Cummings Hamiltonian

$$\frac{\hat{H}_{\mathrm{JC}}}{\hbar} = \omega_r \left(\hat{a}^\dagger \hat{a} + \frac{1}{2}\right) + \frac{\omega_q}{2}\hat{\sigma}_z + \frac{\Omega_0}{2}(\hat{a}\hat{\sigma}_+ + \hat{a}^\dagger\hat{\sigma}_-) \tag{6.12}$$

with $\Omega_0 = 2g_x$. This Hamiltonian leads to a Hybridization of the resonator and qubit modes, meaning that its eigenstates are given by the entangled states

$$\begin{aligned} |+, n\rangle &= \cos\left(\frac{\theta_n}{2}\right)|1\rangle\,|n\rangle + \sin\left(\frac{\theta_n}{2}\right)|0\rangle\,|n+1\rangle \\ |-, n\rangle &= -\sin\left(\frac{\theta_n}{2}\right)|1\rangle\,|n\rangle + \cos\left(\frac{\theta_n}{2}\right)|0\rangle\,|n+1\rangle \end{aligned} \tag{6.13}$$

with $\tan(\theta_n) = \frac{\Omega_0\sqrt{n+1}}{\Delta_{qr}}$. These states are called dressed states and correspond to the eigeinvalues

$$\frac{E_n^\pm}{\hbar} = \omega_r\left(n + \frac{1}{2}\right) \pm \frac{\Delta_{qr}}{2}\sqrt{1 + \frac{4\chi(n+1)}{\Delta_{qr}}} \tag{6.14}$$

Where $\chi \equiv \frac{\Omega_0^2}{4\Delta_{qr}}$ is called the dispersive coupling coefficient. Figure 31 graphically compares this new

[2] Contrary to the previous paragraphs, here the qubit Hamiltonian has $+\hat{\sigma}_z$ instead of $-\hat{\sigma}_z$ to follow the most used convention. The only difference is to switch the order in which the states $|0\rangle$ and $|1\rangle$ are taken in the matrix representation

energy levels and the one of the unperturbed Hamiltonian eigenstate. In the dispersive regime $|\Delta_{qr}| \gg \Omega_0$ there is no resonant photon excange between the qubit and the resonator and the dressed states tend to the unperturbed ones

$$\begin{aligned} |+,n\rangle &\underset{\theta_n \sim 0^+}{\sim} |1\rangle\,|n\rangle \\ |-,n\rangle &\underset{\theta_n \sim 0^+}{\sim} |0\rangle\,|n+1\rangle \end{aligned} \tag{6.15}$$

In this regime the qubit transition frequency becomes $(E_n^+ - E_n^-)/\hbar = \omega_q + 2n\chi + \chi$ showing Stark shift $(2n\chi)$ due to the photons in the resonator and a Lamb shift (χ) due to the vacuum fluctuations in the resonator. Similarly the resonator frequency became dependent on the qubit state $(E_{n+1}^{\pm} - E_n^{\pm})/\hbar = \omega_r \pm \chi$. Indeed, in the dispersive regime the Hamiltonian of Equation 6.11 can be effectively written as

$$\frac{\hat{H}}{\hbar} = \omega_r \left(\hat{a}^\dagger \hat{a} + \chi \hat{\sigma}_z\right) + (\omega_q + \chi)\frac{\hat{\sigma}_z}{2} \tag{6.16}$$

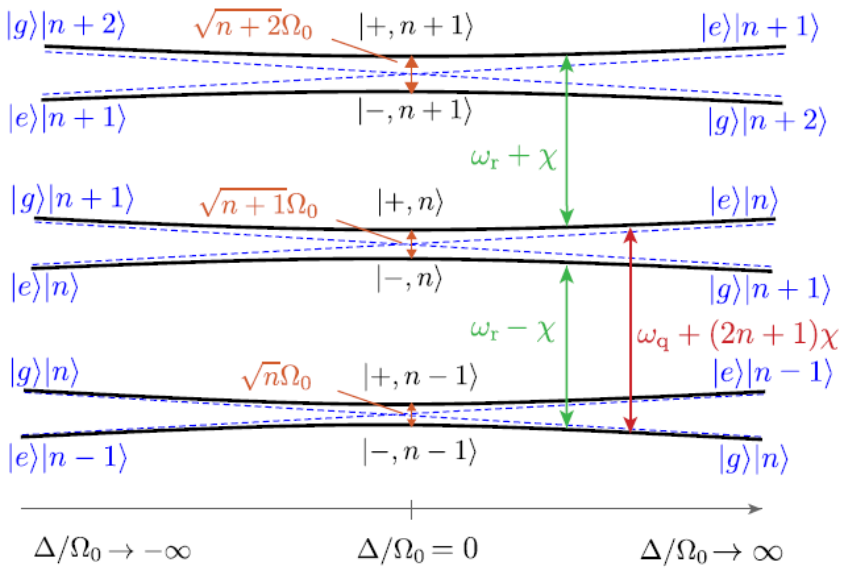

Figure 31: Energy levels of the dressed states (black) and of unperturbed Hamiltonian eigenstates (blue) vs Δ_{qr}/Ω_0. The qubit (red) experiences a Stark shift $2n\chi$ due to the photons in the resonator and a Lamb shift χ due to the vacuum fluctuations in the resonator. The effective resonator frequency (green) is $\omega_r \pm \chi$. [16]

6.6 Dispersive readout

The dispersive coupling to a resonator provides a useful method to measure a superconducting qubit in the $\{|0\rangle, |1\rangle\}$ base. Indeed, as shown in Figure 32, thanks to the dispersive resonator frequency shift the qubit state can be determined from the resonator reflection coefficient. When the system is designed such that $2\chi = \Delta\omega_r$, at the frequency intermediate to the two possible resonances, there is a π phase difference in the reflection coefficient depending on the qubit state. So, a heterodyne measurement of the reflected signal allows distinguishing the two states by putting a threshold in the phasor diagram as shown in Figure 33.

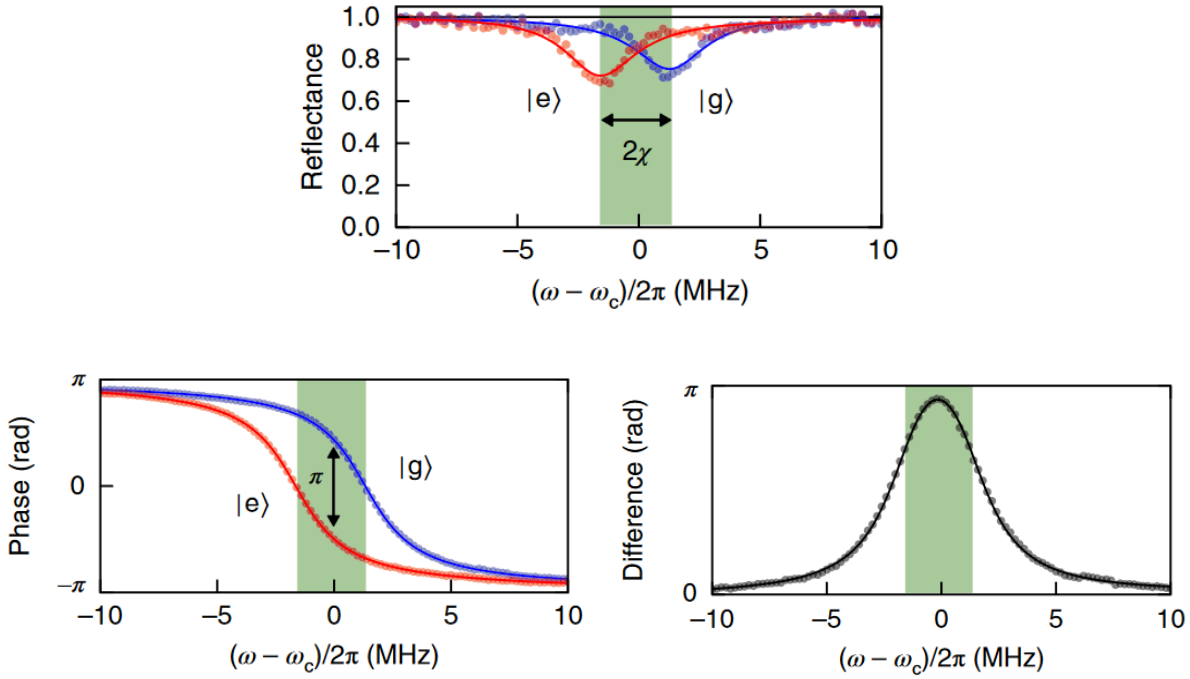

Figure 32: Resonator reflection measurements when the qubit is in the ground $|0\rangle$ or excited $|1\rangle$ state [58].

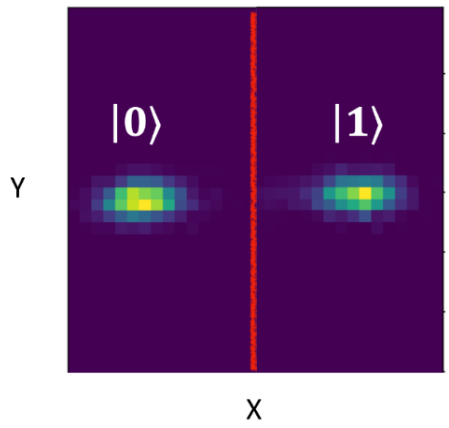

Figure 33: Phasor diagram of the signal reflected on the resonator in the cases in which the qubit is in the ground or excited state. A threshold in the diagram allows distinguishing the two states.

7 Single Microwave Photon Detector (SMPD)

7.1 Detection of confined ad itinerant photons

At optical and infrared frequencies different types of single photons detectors such as Single-Photon Avalanche Diode (SPAD) and Superconducting Nanowire Single Photon Detector (SNSPD) are already commercially available. The photon energy at microwave frequency is roughly five orders of magnitude lower than that of an optical photon, so its detection needs substantially different methods. Single microwave photon detectors mainly exist only as experimental prototypes. A distinction has to be made on the detection of photons which are excitations of a standing-wave resonator mode (confined photons) or of a traveling-wave transmission line mode (itinerant photons). The basic idea for measuring microwave photons in a resonator is to let them interact with a real or artificial[3] atom and then make a measurement on the atom. The detection of confined photons in a 3D resonator was first realized with Rydberg atoms passing through the cavity [59]. Confined photons can also be detected if the resonator is dispersively coupled to a qubit exploiting the qubit frequency shift dependent on the resonator occupation number (see subsection 6.5). A photon detector of this kind has been employed in a dark matter experiment sensitive to hidden photons [17].
Itinerant photons can be detected with a qubit embedded into a resonant cavity thanks to a proper design of the qubit-cavity coupling ad of the cavity resonance. When the qubit is prepared in a superposition state $|+\rangle = \frac{|0\rangle+|1\rangle}{\sqrt{2}}$ an itinerant photon that reflects on the cavity induce a phase flip that brings the qubit to the state $|-\rangle = \frac{|0\rangle-|1\rangle}{\sqrt{2}}$ [58].
Another itinerant photons counter scheme is based on a current biased Josephson junction. Under a bias current $I < I_c$ the the evolution of the junction phase difference ϕ can be described as the one of a 1D particle moving in the washboard potential [21]

$$U(\phi, I) = -\frac{I_c \Phi_0}{2\pi}\cos(\phi) - \frac{I\Phi_0}{2\pi}\phi \tag{7.1}$$

As shown in Figure 34 there are states in which the phase difference is confined in one of the local minima and a state in which the phase increases freely moving down the potential. A microwave photon in a transmission line coupled to the junction can trigger a transition from the confined to the unconfined state. From the Josephson equation $V \propto \frac{d\phi}{dt}$ we see that in the unconfined state there is a finite voltage across the junction which can be measured revealing the transition.
Other possible photon detection schemes are described in [16]. Since most of the microwave photon counter methods are based on superconducting circuits only the ones able to detect itinerant photons can be applied for haloscope experiments since they need to be shielded from the magnetic field in the haloscope cavity. The SMPD that will be used for the pilot experiment is described in subsection 7.2.

7.2 Transmon-based SMPD

The group Quantronics in 2020 demonstrated quantum nondemolition detection of single microwave itinerant photons with a transmon based superconducting circuit[18]. Figure 35 shows the scheme and the working principle of the SMPD. The detector is made of two resonators, called buffer and waste, coupled to a transmon qubit. The buffer and waste resonators are strongly coupled to transmission lines at rate κ_b and κ_w respectively. The buffer line brings the itinerant photons to the detector that are converted into a qubit excitation through a nonlinear process. The qubit state can be measured with a dispersive readout as detailed in subsection 6.6, revealing the presence of the incoming photon. The detection process is thus made possible by the Josephson junction nonlinearity under the effect of a pump tone applied to the qubit with a frequency ω_p that satisfies the frequency matching condition

$$\omega_p = \overline{\omega}_q + \omega_w^e - \omega_b^g \tag{7.2}$$

[3] i.e. a superconducting qubit

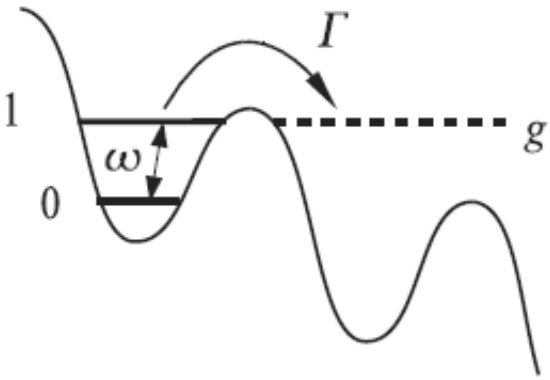

Figure 34: Washboard potential of a current biased Josephson junction. The junction phase difference can be confined in a local minimum or increase moving down the potential. A microwave photon can induce a transition between the two regimes. In the unconfined state, there is a finite measurable voltage across the junction. [16]

with $\overline{\omega}_q$ the qubit frequency under the pump effect, which is slightly shifted from the one of the unperturbed qubit. As discussed in subsection 6.6 the buffer and waste resonant frequencies depend on the qubit state, ω_b^g and ω_w^e denotes the buffer and waste frequencies when the qubit is respectively in the ground or in the excited state. Under these conditions the system is well described by the effective Hamiltonian

$$\frac{\hat{H}_{\text{eff}}}{\hbar} = g\hat{b}\hat{w}^\dagger\hat{\sigma}_+ + g^*\hat{b}^\dagger\hat{w}\hat{\sigma}_- \tag{7.3}$$

where $\hat{b}$ and $\hat{w}$ are the annihilation operators of the buffer and waste mode respectively, and $\hat{\sigma}_\pm$ are the qubit rising and lowering operators. The process rate is $g = \xi_p\sqrt{\chi_{qw}\chi_{qb}}$ where ξ_p is the amplitude of the pump tone expressed in units of the square root of the number of photons, while χ_{qb} and χ_{qw} are the dispersive couplings of the buffer and waste to the qubit, respectively.

The first term in Equation 7.3 $g\hat{b}\hat{w}^\dagger\hat{\sigma}_+$ describes the detection process in which a photon in the buffer is converted into an excitation of the qubit and of a photon in the waste mode. This process is made irreversible through the engineering of the system dissipations as represented in Figure 35 (b). The waste coupling to its transmission line is designed to be $\kappa_w \gg |g|$, so that the photon in the waste is dissipated much faster than the rate of the reverse process $g^*\hat{b}^\dagger\hat{w}\hat{\sigma}_-$ allowing to store the qubit excitation. Indeed, when treating the evolution of the buffer-qubit subsystem, it can be shown that the effect of the coupling with the waste is to add to the Lindblad master equation the loss operator $\hat{L} = \sqrt{\kappa_{nl}}\hat{b}\hat{\sigma}_+$, with $\kappa_{nl} = 4|g|^2/\kappa_w$ [18]. This operator is nonlocal since it involves operators from two different modes and nonlinear since it contains the product of the operators. The effect of this operation is an evolution of the qubit toward its excited state conditioned to the presence of a photon in the buffer.

The reverse process described by the second term in Equation 7.3 provides a useful way for resetting the qubit to the ground state. Indeed, by applying a coherent tone to the waste the qubit excitation combines with waste photons bringing the qubit back to the ground state and releasing a photon in the buffer as represented in Figure 35 (c).

Table 7 show the parameters of the device reported in [18]

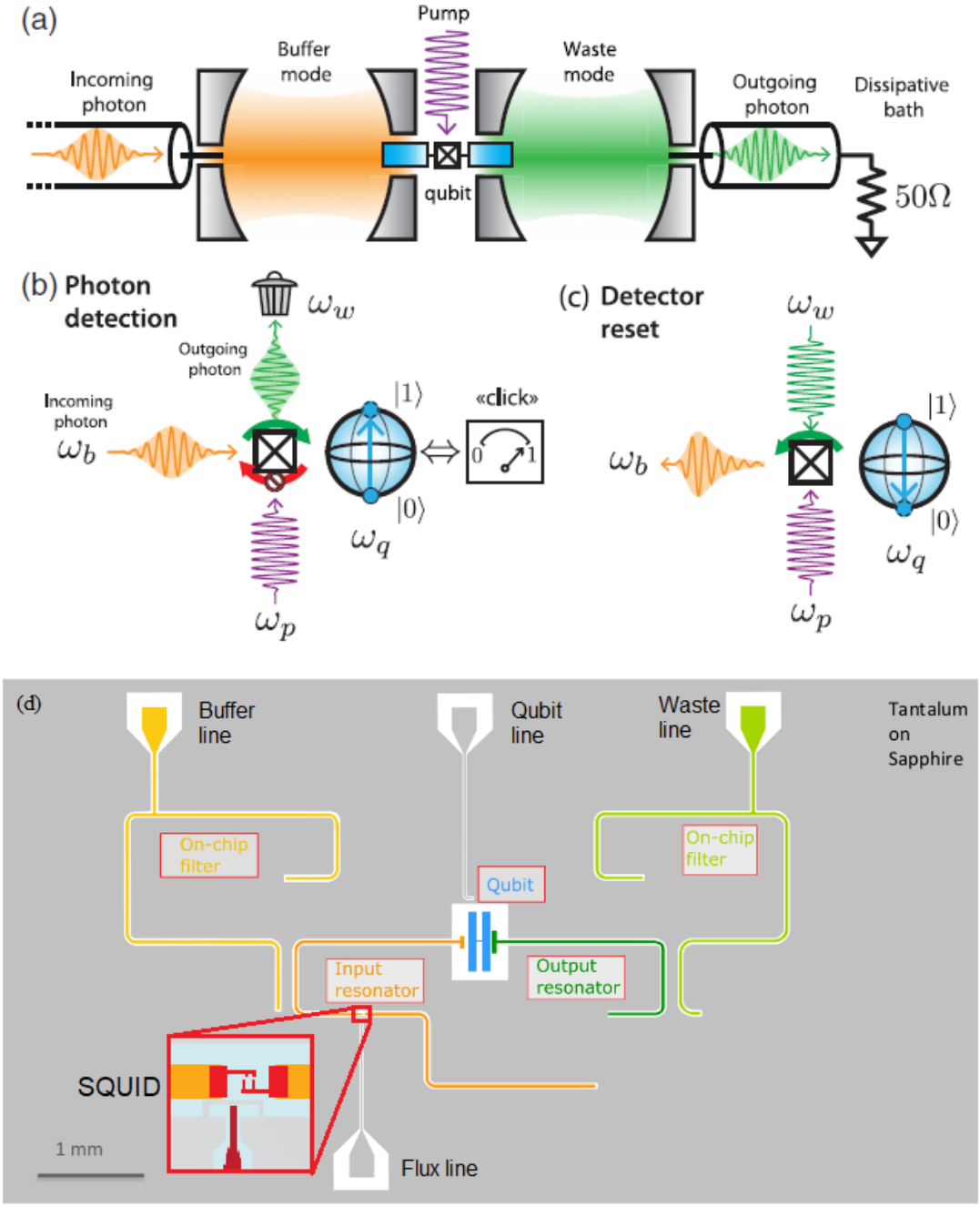

Figure 35: (a) SMPD Schematic. Two resonators, buffer and waste, are coupled to a transmon qubit. The buffer is coupled to a transmission line that on which propagates the itinerant photons that have to be detected. The waste resonator is coupled to a transmission line that allows for quickly dissipating excitations of the waste mode. A pump tone is applied to the qubit. (b) Photon detection principle. The presence of the pump enables a nonlinear process that can convert a photon in the buffer into a qubit excitation and a photon in the waste. The waste photon is dissipated through the waste line so that the reverse process is inhibited and the detection becomes irreversible. A readout of the qubit state reveals if a photon was detected. (c) The qubit can be rest to the ground state using the reverse nonlinear process. A coherent tone is applied to the waste resonator so the qubit excitation can combine with waste photons ad be released as a photon in the buffer. (d) SMPD circuit layout. The circuit is realized with a Tantalum deposition on a Sapphire substrate. The buffer and the waste are coupled to the respective transmission lines through other two resonators that act as filters. The purpose of these filters is to allow a strong coupling with the lines without degradation of the qubit relaxation time T_1. A SQUID loop inserted into the buffer resonator allows to tune the device[18].

Table 7: Parameters of the device reported in [18]. The one that will be used for the pilot experiment is a new version of the device so its parameters are different but these can be taken as some reference value.

Qubit		Waste mode		Buffer mode	
$\omega_q/2\pi$	4.532 GHz	$\omega_w^g/2\pi$	5.7725 GHz	$\omega_b^g/2\pi$	5.4952 GHz
T_1	8-9 μs	$\kappa_{w,\mathrm{ext}}/2\pi$	2.38 MHz	$\kappa_{b,\mathrm{ext}}/2\pi$	0.890 MHz
T_2^*	10 μs	$\kappa_{w,\mathrm{int}}/2\pi$	< 100 kHz	$\kappa_{b,\mathrm{int}}/2\pi$	80 MHz
$\chi_{qq}/2\pi$	146 MHz	$\chi_{qw}/2\pi$	2.73 MHz	$\chi_{qb}/2\pi$	2.73 MHz

7.3 SMPD operation cycle

The SMPD operation follows the general steps of a quantum sensing protocol consisting of repetitively preparing the qubit in an initial state, making it evolve interacting with the quantity under measurement, and readout the final state.[15] Indeed, the SMPD operates by continously repeating a detection cycle with a period $\tau_{\mathrm{SMPD}} \approx 15\,\mu$s. As shown in Figure 36, the cycle is divided in the following three steps

- R: The qubit is reset to the ground state by applying a coherent tone to the waste resonator.
- D: The detector is exposed for a certain time window to itinerant photons coming from the buffer line.
- M: The qubit state is measured with a dispersive readout to determine if a photon has excited the qubit.

Each cycle gives as output a boolean variable corresponding to the presence or absence of a photon during the cycle.

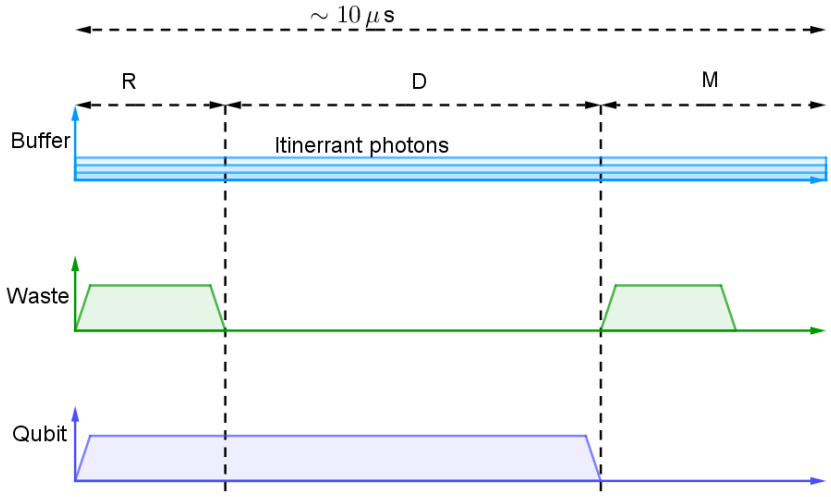

Figure 36: SMPD detection cycle. In the reset step (R) a coherent tone is applied to the waste resonator to bring the qubit to the ground state. In the detection step (D) the SMPD is sensitive to itinerant photons that can trigger the nonlinear qubit excitation process. In the measurement step (M) the qubit state is measured determining whether a photon was collected during the detection time. During continuous operation, this cycle is repeated in a loop.

7.4 Setup

The SMPD operates in a dilution fridge with a 10 mK base temperature. Figure 37 shows the scheme of the low-temperature stage of the setup used for the experimental tests reported in section 8, which is similar to the one that will be used in the haloscope experiment. The signals injected into the buffer line (blue) are routed toward a resonant cavity containing currently hosting Erbium-doped crystal used for running fluorescence measurements [60]. This cavity will be substituted by the NbTi cavity described in

section 3 for the pilot haloscope experiment. Signals originated in the cavity or reflected at its input port are directed to the SMPD buffer via a circulator. The buffer line includes an output port that allows for measuring the spectrum of signals reflected on the cavity on the buffer. The qubit line (purple) is used to apply the pump tone and control pulses to the qubit. The flux line (red) brings the dc current that sets the magnetic flux value through the buffer SQUID. The waste line (green) constitutes the dissipation channel of the waste mode. This line is also used to send reset pulses and for the qubit dispersive readout. The readout signal has to be weak enough not to perturb the qubit, thus the reflected signal needs to be amplified before the heterodyne measurement. This is accomplished using a TWPA as the first amplification stage. The TWPA pump is provided via another line (yellow) that is coupled with a directional coupler to the waste line downstream to the SMPD. All the lines are provided with attenuators and infrared-blocking filters to reduce noise coming from higher temperature stages.

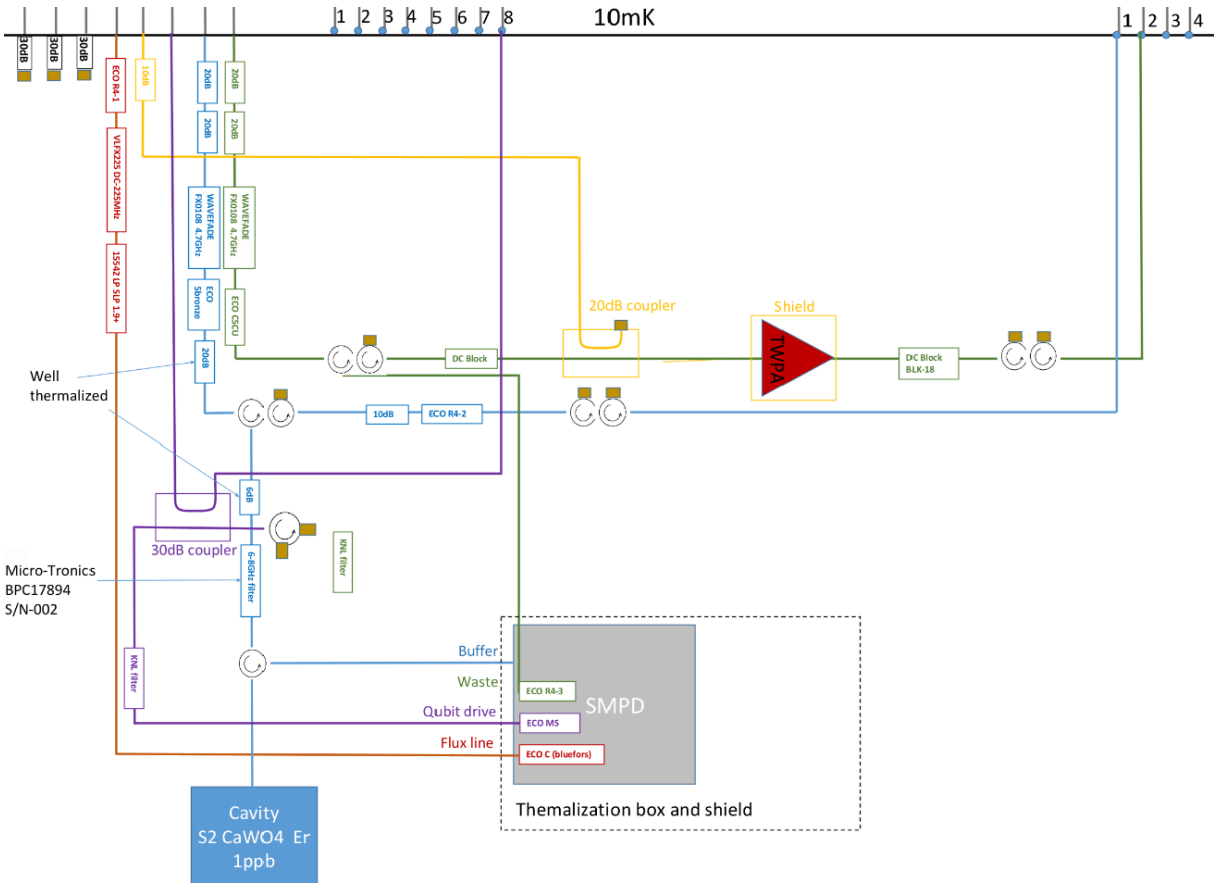

Figure 37: scheme of the low-temperature apparatus. The buffer line brings external signals to the cavity and connects the cavity to the buffer. The qubit line (purple) sends the pump tone and control pulses to the qubit. The flux line (red) provides the magnetic flux to the buffer SQUID. The waste line (green) is used as the dissipation channel of the waste mode, to send reset pulses and for the qubit dispersive readout. The readout signal is amplified with a TWPA feed via a TWPA pump line (yellow).

Figure 38 shows main elements present in the room-temperature electronics. The SMPD is operated via a Field Programmable Gate Array (FPGA)-based control developed by Quantum Machines [61]. This module incorporates three Arbitrary Waveform Generator (AWG) whose output rf signals are mixed to GHz-frequency LOs to produce all the pulses needed for SMPD operation. The QM also implements the acquisition and analysis of the demodulated output readout signal to determine the qubit state. The output data provided by the QM is a time stamp sequence corresponding to the times at which the qubit was found in the excited state. The signals sent on the buffer line are split and measured with a SA to monitor their power (see subsubsection 8.3.2). A dc voltage generator sets the magnetic flux in the buffer SQUID. A signal generator provides the TWPA pump tone.

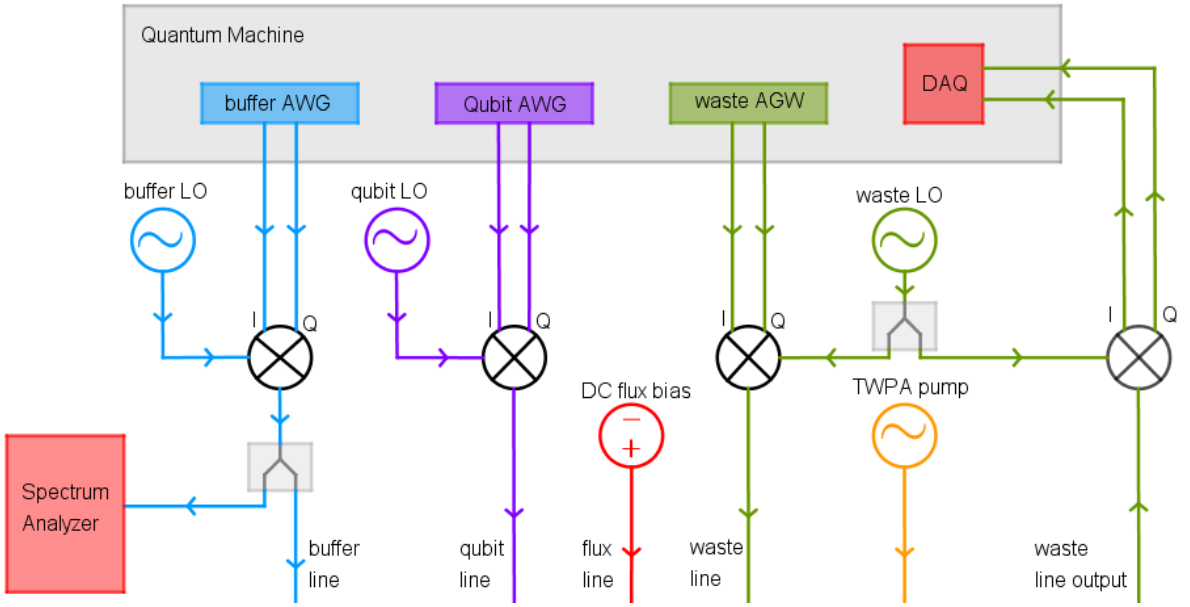

Figure 38: Principal elements of the room temperature part of the apparatus. A control module (Quantum machine) generates the envelope signals that are mixed to GHz LO and provides the pulses needed for SMPD operation. This module acquires the readout signal determining the qubit state. A dc voltage generator sets the magnetic flux in the buffer SQUID. A signal generator provides the TWPA pump tone. A SA is used to monitor the power of the signals sent on the buffer line.

7.5 Detector tunability

The SMPD allows for detection of photons in a ∼100 MHz-width frequency range centered around 7.33 GHz. The detector bandwidth is set by the buffer resonator linewidth $\Delta\nu_b \approx 1$ MHz. The buffer frequency can be tuned across the working range by applying a magnetic flux to an embedded SQUID (see subsection 2.4).

The magnetic flux is regulated by a dc voltage generator. When we set the generator for the first time to a new bias voltage we need to identify the new pump frequency that satisfies the frequency matching condition Equation 7.2. As shown in Figure 39 (c) (d) this can be accomplished by scanning the pump frequency and recording the number of clicks. During the scan a signal can also be injected on the buffer line to provide the photons to detect, whose frequency an be adjusted to match the new buffer frequency. The number of clicks is maximum when the signal frequency matches the the new buffer frequency ω_b^g with the qubit in ground state. Keeping a fixed pump frequency and scanning the signal one, the SMPD efficiency profile can be recorded as shown in Figure 40. The width of the recorded curve is related to the buffer resonance linewidth, $\Delta\nu_b \approx 1$ MHz.

7.6 Efficiency measurement

The SMPD efficiency can be measured by sending a well known signal on the buffer line and measuring the corresponding click rate. The photon flux at the buffer input is calibrated by performing a Ramsey interometry while applying the signal to the buffer. Due to dispersive coupling, the presence of photons in the buffer resonator induces a qubit frequency shift. The photon number fluctuations lead to fluctuations of the frequency shift increasing the qubit dephasing rate. If $\epsilon_{\rm rf}$ is the signal field amplitude, and $\delta_r = \omega_b - \omega_{\rm rf}$ is the detuning between the buffer aand the signal frequency [4], the qubit frequency shift is given by [62]

$$\delta\omega_q = \chi_{qb}(\overline{n}_+ + \overline{n}_-) - \chi_{qb}D_s \tag{7.4}$$

[4] Here ω_b the bare buffer frequency i.e. the one corresponding to ω_r in Equation 6.16 that do not incorporate the qubit state dependent shift.

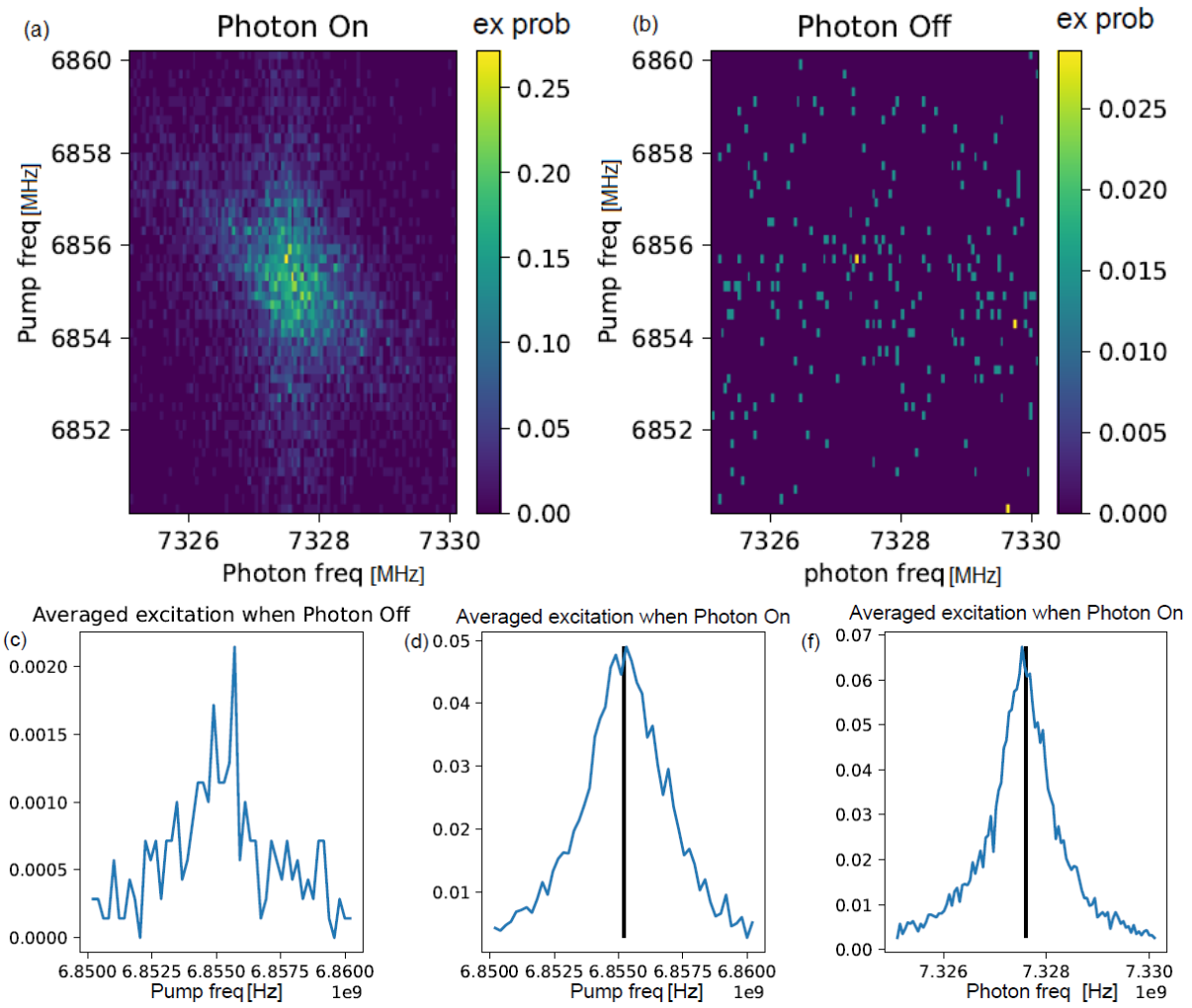

Figure 39: Pump frequency calibration. The pump frequency is scanned looking for the value that maximise the efficiency of the nonlinear detection process and thus the probability of measuring the quibit in the excited state. The plots shows the excitation probability when (a) a signal is applied to the buffer line and its frequency is scanned around the buffer frequency. (b) no signal is applied and only dark counts are collected. (c),(d) and (e) shows the marginal distributions obtained from the (a) and (b) plots. The black vertical line in (d) indicates the chosen pump frequency, and in (e) the frequency of the signals that will be injected on the buffer line (see subsection 8.3)

with χ_{qb} the buffer-qubit dispersive coupling coefficient

$$\begin{aligned} \overline{n}_{\pm} &= \frac{\epsilon_{\mathrm{rf}}^2}{\kappa_b^2/4 + (\delta_r \pm \chi_{qb})^2} \\ D_s &= \frac{2(\overline{n}_+ + \overline{n}_-)\chi_{qb}^2}{\kappa_b^2/4 + \chi_{qb}^2 + \delta_r^2} \end{aligned} \tag{7.5}$$

The added dephasing rate is

$$\Gamma_m = \frac{(\overline{n}_+ + \overline{n}_-)\kappa_b \chi_{qb}^2}{\kappa_b^2/4 + \chi_{qb}^2 + \delta_r^2} \tag{7.6}$$

For calibration, the signal frequency is scanned around the buffer one while keeping a constant amplitude. Detuning and dephasing rate are measured with Ramsey interferometry, they are then fitted as function of δ_r according to Equation 7.4 and Equation 7.6 with k_b χ_{qb} and ϵ_{rf}^2 as fitting parameters.Figure 41 shows the profile of these curves. The value of ϵ_{rf}^2 gives a measure of the photon flux at the buffer input.

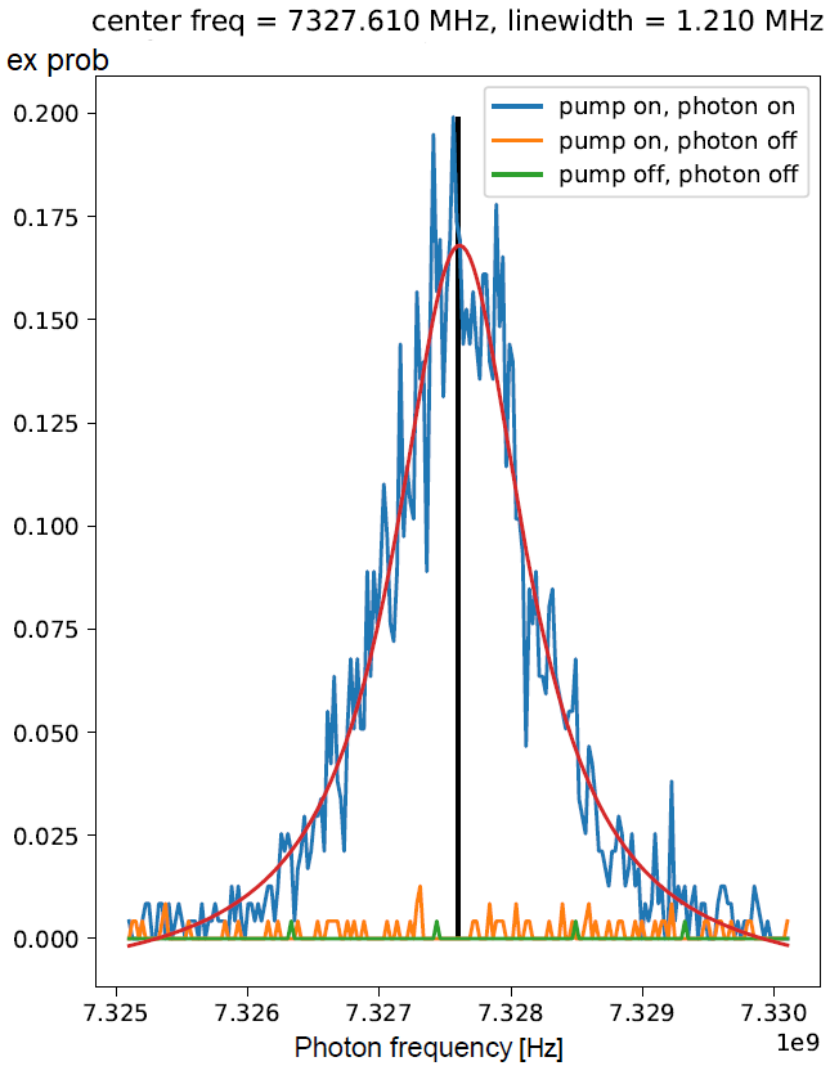

Figure 40: Qubit excitation probability when vs signal frequency. The profile is related to the one of the buffer resonance.

This photon counting method gives good results for a sufficiently high photon flux $\sim 10^3$ photons/s, but it is not reliable for measuring low power signals. The SMPD efficiency η is finally calculated as the ratio of SMPD click rate over the photon flux calculated from calibration. The efficiency measured with this protocol is referred to photons at the buffer input. We measured $\eta \approx 0.4$ as shown in Figure 54.

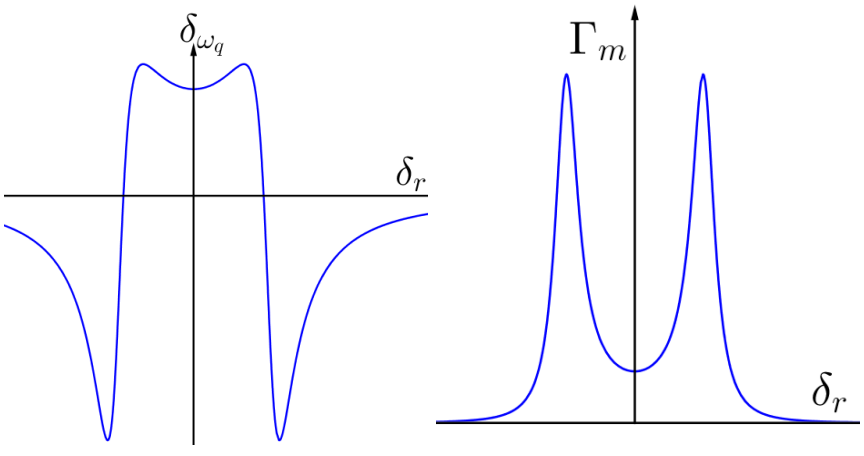

Figure 41: Profiles of detuning (left) and dephasing (right).

The performance of the SMPD that will be used in the pilot haloscope experiment are reported in Table 8

Table 8: Summary of the performance of the SMPD that will be used in the pilot haloscope experiment.

Detector bandwidth	$\approx 1\,\mathrm{MHz}$
Detector tunability range	$[7.28; 7.38]\,\mathrm{GHz}$
Dark count rate (Γ_{dc})	$\approx 100\,\mathrm{Hz}$
Efficiency (η)	≈ 0.4
Operating temperature	$10\,\mathrm{mK}$

8 Darkcount and preliminary tests analysis

8.1 Dark counts rate

When no signal is applied, the SMPD has a residual detection rate referred to as dark count rate Γ_{dc}. In previous measurements, it has been observed that this rate depends on the system temperature and the data reported in the following refers to an operation in the optimal case in which the system is thermalized at the dilution refrigerator base temperature of 10 mK. Figure 42 shows a typical sequence of dark count clicks and the dark count rate measured in an 8-hour-long acquisition. Γ_{dc} is about 100 Hz and clearly not stationary.

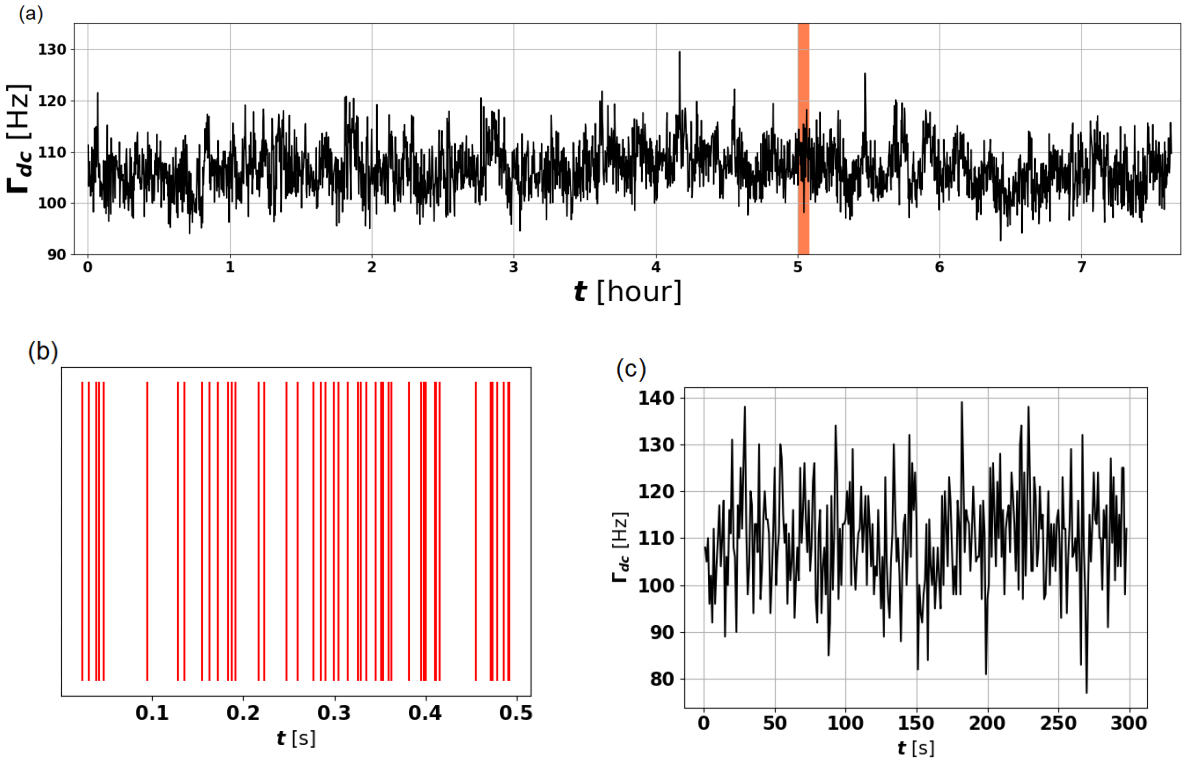

Figure 42: (a) Time series of the dark count rate Γ_{dc} measured in 10 s-duration intervals in an almost 8-hour-long acquisition. (b) A typical sequence of clicks collected in 0.5 s. (c) dark counts rate computed on 1 s-duration intervals for the 300 s time window highlighted in (a).

As shown in Figure 39 (c),when the pump frequency is detuned from the frequency matching condition (Equation 7.2) the dark count rate decreases. This shows that the counts are related to the presence of photons in the buffer resonator. These photons come from noise coupled to the buffer line and from the thermal excitation of the cavity, of the transmission line and of the buffer resonator.
To define an equivalent noise temperature of the buffer line we can consider the scheme in Figure 43. A load at the equivalent temperature T_{sys} emits itinerant photons on the buffer line. The cavity is represented as a lossless cavity coupled to a load at the cavity temperature. In this model we assume a dark count free SMPD.
The noise spectrum can be written as

$$S^N(\nu) = h\nu \left[T(\nu)\overline{n}(T_{cav}) + R(\nu)\overline{n}(T_{sys})\right] \tag{8.1}$$

with $T = |S_{21}|^2$, $R = |S_{22}|^2$ the cavity transmission and reflection coefficients, and $\overline{n}$ is the average occupation number at a given temperature.

$$\overline{n}(T) = \frac{1}{e^{h\nu/k_BT} - 1} \underset{k_BT \ll h\nu}{\sim} e^{-\frac{h\nu}{k_BT}} \tag{8.2}$$

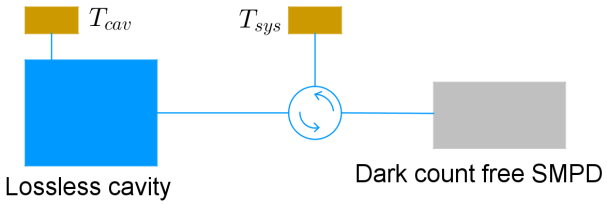

Figure 43: Noise equivalent system. A load at the equivalent temperature T_{sys} emits itinerant photons on the buffer line. The cavity is represented as a lossless cavity coupled to a load at the cavity temperature, and is readout by a dark count free SMPD.

The efficiency of the SMPD has a Lorentzian profile centered at the buffer frequency ν_b with a linewidth $\Delta\nu_b$ and a peak value η_0.

$$\eta(\nu) = \frac{\eta_0}{4\frac{(\nu-\nu_b)^2}{\Delta\nu_b^2} + 1} \tag{8.3}$$

The dark count rate is then calculated as

$$\Gamma_{\mathrm{dc}} = \int \frac{S^N(\nu)}{h\nu}\eta(\nu)d\nu \tag{8.4}$$

When the buffer is sufficiently detuned from the cavity resonance frequency $R(\nu_b) = 1$ $T(\nu_b) = 0$. So the dark count rate is

$$\Gamma_{\mathrm{dc}} = \frac{\pi}{2}\Delta\nu_b\eta_0\overline{n}(T_{sys}) \tag{8.5}$$

We measure a dark count rate $\Gamma_{\mathrm{dc}} \approx 100$ Hz, a buffer linewidth $\Delta\nu_b \approx 1$ MHz and a peak efficiency $\eta \approx 0.4$. This gives an equivalent line temperature $T_{sys} \approx 40\,\mathrm{mK}$, exceeding the base temperature of the dilution fridge (10 mK). This indicates that noise coupled from higher temperature stages is non-negligible.

A cavity thermalized at $T_{cav} < T_{sys}$ at $\nu = \nu_c$ should absorb rather than emit photons. This effect influences the dark count rate as shown in the plot of Figure 44 which was obtained from Equation 8.4 with $T_{sys} = 40\,\mathrm{mK}$, $T_{cav} = 10\,\mathrm{mK}$, $\Delta\nu_b = 1\,\mathrm{MHz}$, $Q_L = 2 \times 10^5$, $\nu_{cav} = 7.3\,\mathrm{GHz}$ and a detuning $\delta\nu = \nu_c - \nu_b$ between the cavity frequency and the buffer frequency.

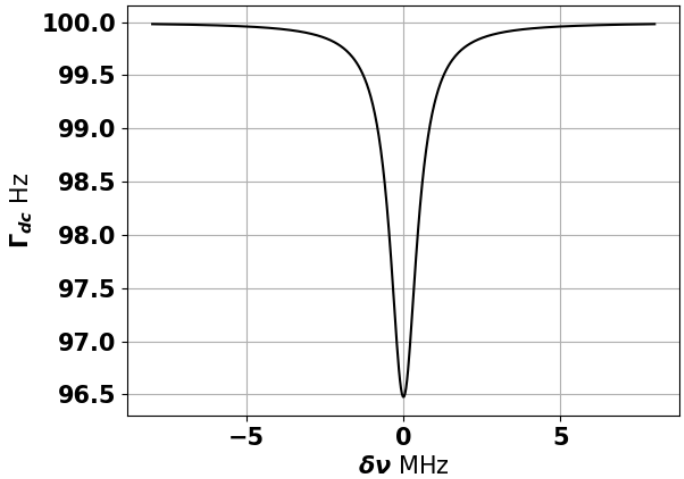

Figure 44: Expected dark count rate when the cavity is thermalized at T_{cav} below the system equivalent temperature T_{sys} evaluated from Equation 8.4 for different values of the detuning $\delta\nu$ between cavity and buffer resonant frequency.

8.2 Inhomogeneous Poisson process

As shown in Figure 42 dark counts have not stationary increments. In this subsection, I present some tests we performed to verify that the dark counts process can be described as an inhomogeneous Poisson process[63]. An inhomogeneous Poisson process is a counting process: $\{N(t), t \geq 0\}$, so that N has integer values that never decrease over time, but jump up at random times, and that satisfies the following conditions:

i $N(0) = 0$

ii increments are independent (Markov) but not stationary

iii $P(N(t+h) - N(t) = 1) = \lambda(t)h + o(h)$

iv $P(N(t+h) - N(t) > 1) = o(h)$

Where $\lambda(t)$ is a function of time called rate or intensity of the process. The number of counts N_{12} collected in the time interval $[t_1, t_2]$ is a random variable with Poissonian distribution

$$P(N_{12} = n) = \frac{\left(\int_{t_1}^{t_2} \lambda(t)dt\right)^n}{n!} \exp\left\{-\int_{t_1}^{t_2} \lambda(t)dt\right\} \tag{8.6}$$

As in the ordinary Poisson process average and the variance of the distribution are equal

$$E(N_{12}) = Var(N_{12}) = \int_{t_1}^{t_2} \lambda(t)dt \tag{8.7}$$

8.2.1 Waiting time distribution

In an inhomegeneous Poisson process, when a click is detected at time t the probability density function (pdf) for the waiting time τ before the next event is given by

$$p(\tau|t) = \lambda(t+\tau) \exp\left\{-\int_t^{t+\tau} \lambda(t')dt'\right\} \approx \lambda(t)e^{-\lambda(t)\tau} \tag{8.8}$$

Where the last approximation when the time scale on which the function λ varies is much longer than the delay between increments.
Given an observation of the process on the time interval $[0, T]$ the pdf of the waiting time between the events can be written as

$$p(\tau) = \int_0^T p(\tau|t)p(t)dt \tag{8.9}$$

with $p(t)$ the pdf of having a click at time t. We can estimate the probability that a click occoured before time time t as the ratio of the average number of counts before time t over the total expected counts

$$P(t_{click} < t) \approx \frac{\int_0^t \lambda(t')dt'}{\int_0^T \lambda(t')dt'} \quad \Rightarrow \quad p(t) = \frac{dP(t_{click} < t)}{dt} = \frac{\lambda(t)}{T\overline{\lambda}} \tag{8.10}$$

with $\overline{\lambda}$ the average of $\lambda(t)$ in the interval $[0, T]$. Assuming that the variations of λ are small compared to its average value, we can write a Fourier series

$$\lambda(t) = \overline{\lambda} + \sum_n \delta_n \cos(2\pi\nu_n t + \phi_n) \qquad \frac{\delta_n}{\overline{\lambda}} \sim \delta_n \tau \ll 1 \quad \forall n \tag{8.11}$$

Equation 8.9 then gives

$$
\begin{aligned}
p(\tau) &= \int_0^T \frac{\lambda(t)^2}{T\overline{\lambda}} e^{-\lambda(t)\tau} dt \\
&\approx \frac{\overline{\lambda} e^{-\overline{\lambda}\tau}}{T} \int_0^T \left[1 + \sum_n \frac{\delta_n}{\overline{\lambda}} \cos(2\pi\nu_n t + \phi_n) + O\left(\frac{\delta^2}{\overline{\lambda}^2}\right) \right] dt \\
&\approx \overline{\lambda} e^{-\overline{\lambda}\tau} + O\left(\frac{\delta^2}{\overline{\lambda}^2}\right)
\end{aligned}
\tag{8.12}
$$

Where the last approximation holds if T is long compared to the time over which $\lambda(t)$ oscillate. As shown in Figure 45 the distribution of the delay time τ between consecutive clicks has an exponential behavior with a rate equal to the averaged intensity. The average rate obtained from the exponential fit is $\overline{\lambda}_{fit} = 106.57 \pm 0.05$ Hz, the one computed as the total number of counts over the total acquisition time is $\overline{\lambda}_{count} = 106.70 \pm 0.06$. Note that the residuals from the fit show an excess in the first bin of the histogram. This excess can be ascribed to the finite fidelity of the qubit reset. If p is the probability that in an SMPD cycle a photon is detected and p_{err} the probability of an error in the reset, the probability of waiting for n cycles between two detections can be written as

$$
P(n) \approx (1-p)^{n-1} p + p_{err}\delta_{1,n} \approx p + p_{err}\delta_{1,n} \quad n \sim 1 \tag{8.13}
$$

Estimating p as the ratio of the total number of counts over the total number of cycles gives $p \approx 1.6 \times 10^{-3}$. The binning of the histogram in Figure 46 is chosen such that each bin corresponds to an integer number of SMPD cycles. The excess of probability is concentrated in the first two bins and the bins corresponding to $n > 3$ have probability $p \approx 1.5 \times 10^{-3}$. So we can estimate the reset error probability to be $p_{err} \approx 2 \times 10^{-3}$ compatible with the reset fidelity reported in [18]. Estimating p_{err} from a separate fidelity we may compute a correction for the number of consecutive detections.

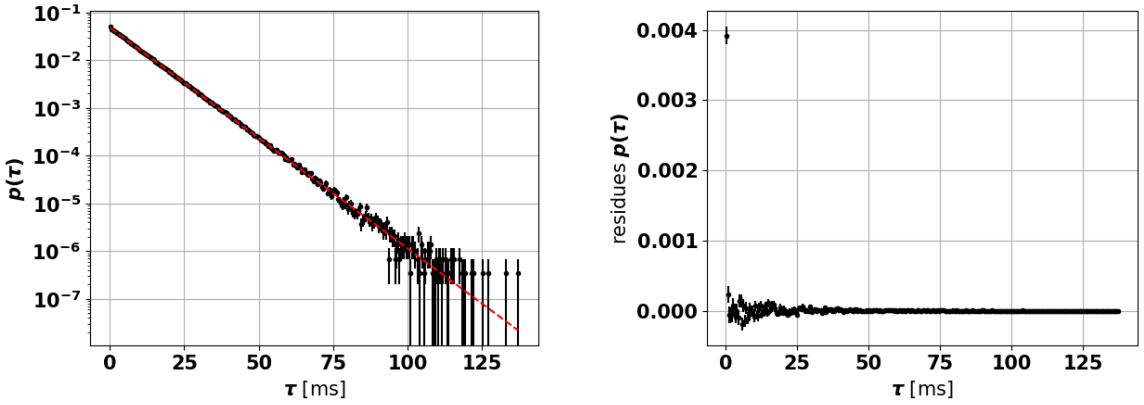

Figure 45: On the left: histogram of delay between detections. The distribution shows the expected exponential behaviour. On the right: residuals from the exponential fit, The first bin in the histogram shows an excess of counts.

8.2.2 Mean variance equality

A second test was aimed to verify that dark count data satisfy Equation 8.7. we can not rely on substituting the ensemble average with a time average because the variations in $\lambda(t)$ would increase the variance of the number of counts collected in equal size intervals spread across the whole data acquisition. However, we can exploit the fact that the drift in $\lambda(t)$ has a long time scale and treat it as locally constant. We divided the data into samples of duration Δt. For each sample we count the number of clicks collected in one second-duration intervals, and then compute the difference between the average number of counts

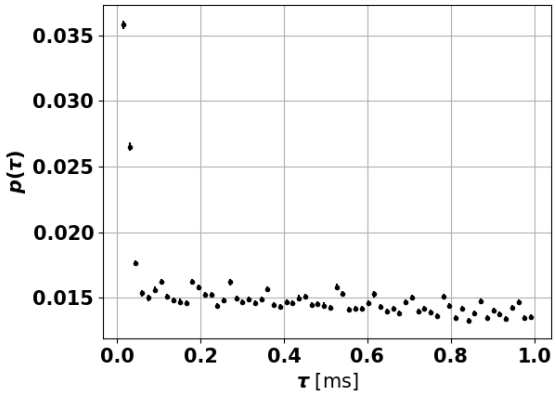

Figure 46: Histogram of delays shorter than 1 ms with bin size equal to the SMPD cycle.

and the variance.

$$\delta \equiv \frac{Var(n) - E(n)}{100} \tag{8.14}$$

Figure 47 shows the distribution of δ for the case $\Delta t = 30\,\mathrm{s}$ and $\Delta t = 300\,\mathrm{s}$. For comparison, we applied the same algorithm to a simulated Poisson process with a constant rate $\Gamma = 100\,\mathrm{Hz}$. The two distributions are well superimposed in the first case while in the second the effect of intensity drifts is evident.

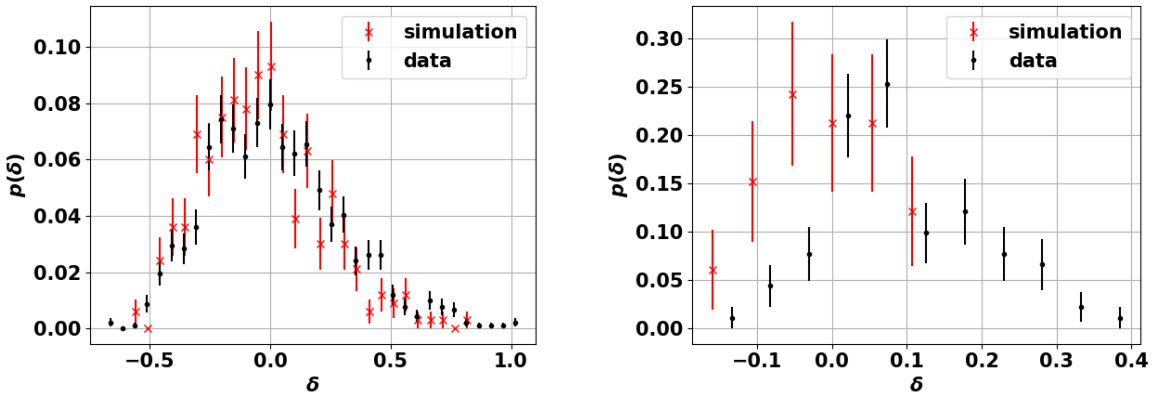

Figure 47: distribution of δ when calculated on 30 s (left) and 300 s (right) intervals.

8.2.3 Linear increase of detection probability for short intervals

The third test we performed is a verification of the conditions iii and iv requested for a Poisson process (subsection 8.2). We checked these conditions on the first 30 s of data so that we can neglect effects due to the intensity inhomogeneity. Figure 48 shows the linear increase of the one detection probability for short observation time h. Once again we compare the results from our data to the ones obtained from simulation. Table 9 reports the results of the fit. The rate estimated from the fit is lower than the one calculated from the total number of counts as is the case also int simulated data.

Table 9: Fit Results of $P(N(t+h) - N(t) = 1)$ vs h for $h < 1\,\mathrm{ms}$.

data	λ_{fit}	$P_{h=0}$	ρ	#count/30 s
	$99.1 \pm 0.9\,\mathrm{Hz}$	$(8 \pm 2) \times 10^{-4}$	0.9998	$107 \pm 2\,\mathrm{Hz}$
sim	λ_{fit}	$P_{h=0}$	ρ	#count/30 s
	$86.5 \pm 0.5\,\mathrm{Hz}$	$(1.5 \pm 0.2) \times 10^{-3}$	0.998	$97 \pm 2\,\mathrm{Hz}$

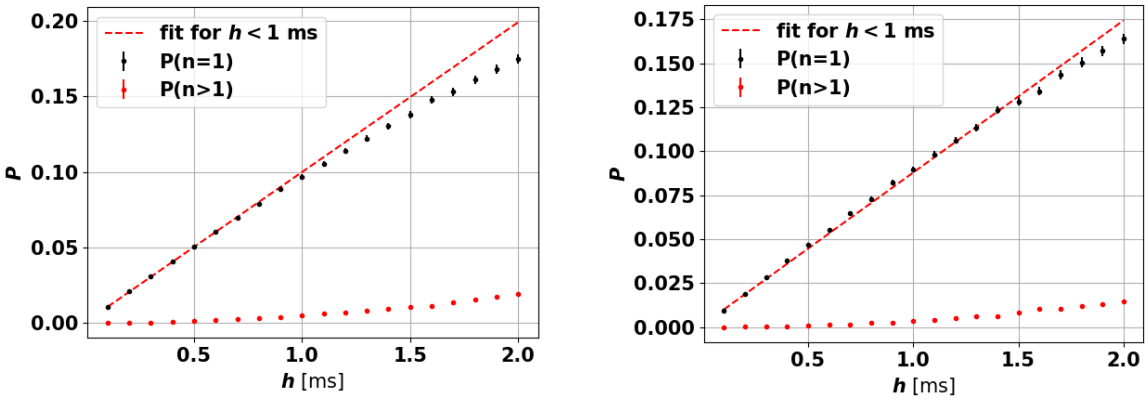

Figure 48: Probability of having one or more clicks in an time interval h observed in the data (left) and in a simulation (right).

8.3 On-off protocol

To use the SMPD for the detection of a small signal we need to reduce statistical fluctuations in the dark counts below the count increment due to the presence of the signal. The drifts in the dark count intensity exceeds than the intensity of the axion related signal we aim to detect. Our strategy to deal with these drifts exploits the SMPD tunability discussed in subsection 7.5. We set the non resonant value choose two reference buffer frequencies $\nu_{\rm on} = \nu_{cav}$ and $\nu_{\rm off} \neq \nu_{cav}$, one in resonance with the cavity, the other detuned by a few MHz, and switch the SMPD between these two frequencies every few seconds. The aim of this protocol is to use the dark counts measured at the detuned frequency $\nu_{\rm off}$ to infer on the intensity function $\lambda_{\rm on}(t)$ when counts at $\nu_{\rm on}$ are recorded. The minimum time required for switching from one frequency to another can be as low few μs.

8.3.1 Fixed frequency test by software and hardware signal injection

We first tested our strategy at a fixed buffer frequency, intermittently injecting a signal into the system, as shown in Figure 49. The dark counts during the whole acquisition should be generated by the same process.The test objective is to use the data collected when the signal is not applied (b-intervals) to set a threshold that allow to identify the presence of the signal.

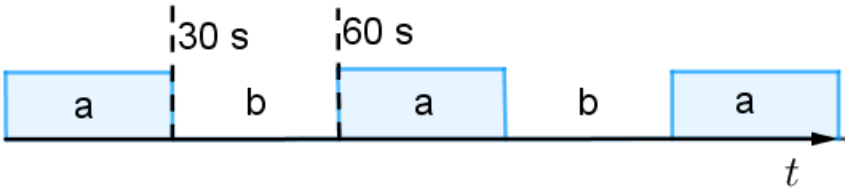

Figure 49: Sequence of signals sent on the buffer line. In each a-b cycle the signal is on for 30 s and then turned off for 30 s

The signal was injected both via software and hardware. For software injection, we added to the dark counts data some artificial counts generated according to a Poisson process with rate $\Gamma_{sig} = 3$ Hz. Assuming a detector efficiency $\eta = 0.4$ this value corresponds to a signal power $P_{sig}/h\nu = 7.5$ Hz. The reason for the choice of this value will be clarified in the following.
The data were divided into groups of 5 on-off cycles each, so that each group has a total of $\tau = 150$ s dark count/signal acquisition. To discriminate the presence of a signal we consider the counts difference $N_{\rm a} - N_{\rm b}$ normalized to the standard deviation expected for a process with 100 Hz rate

$$\Delta N \equiv \frac{N_{\rm a} - N_{\rm b}}{\sqrt{100\tau}} \tag{8.15}$$

Similarly, we applied the discrimination strategy based on the Kumar-Caroll index computing $\langle \Delta t \rangle_1$ on data during a-periods and $\langle \Delta t \rangle_0$ during b-periods.
To evaluate false positive rate we applied the same analysis to the dark count data without injecting any signal. Figure 50 shows the ROC curve we obtained for the detection of the injected signal. A degradation with respect to Equation 4.34 can be expected due to the 50% duty cycle introduced with the on-off protocol and to the fact that the dark count rate is not a priori known but is inferred from data. However, the curve is still above the limit calculated for a linear amplifier at the SQL. Hardware injection is performed by sending directly a pure tone at the buffer frequency. Since a bolometric measurement can not reconstruct the signal spectrum, we expect this tone to give the same results that would be obtained from a signal with a more elaborated spectrum within the buffer bandwidth $\Delta\nu_b \approx 1\,\mathrm{MHz}$ and the same average power. We collected data for about 60 hours. Figure 51 shows the evolution of the count rate measured on every 30 s interval when the injected signal is on (a) or off (b). The signal gives a net increase in the count rate of $3.00 \pm 0.04\,\mathrm{Hz}$. The data were analyzed as described for the software injection to extract the ROC curve shown in Figure 50. Also the hardware test present a ROC curve beyond the SQL. Figure 52 shows the distributions of ΔN and d_{kc} in presence or absence of the injected signal. ΔN and d_{kc} are highly correlated so the two criteria gives equivalent ROC curves.

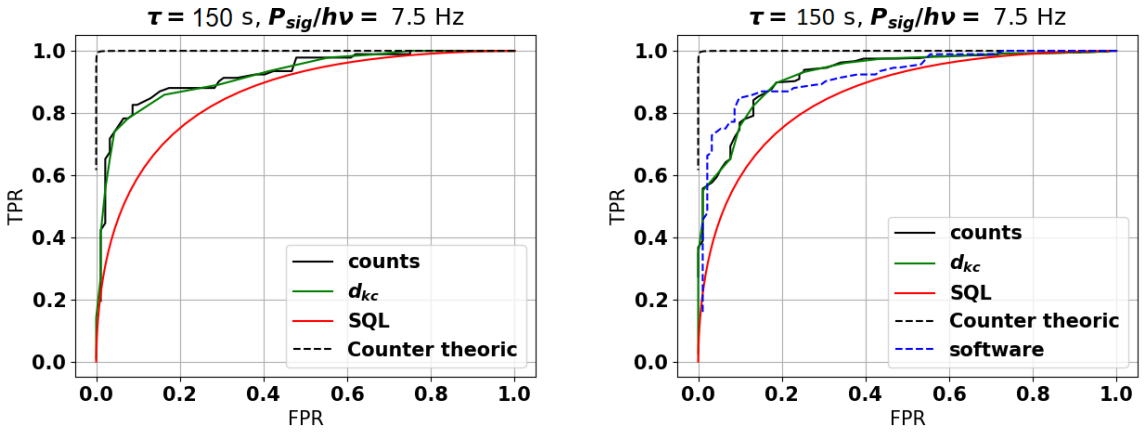

Figure 50: On the left: ROC curve estimated with software injection of a signal in dark count data. The artificial data are injected with rate $\Gamma_{sig} = 3\,\mathrm{Hz}$. For an SMPD efficiency $\eta = 0.4$ this is equivalent to a signal with power $P_{sig}/h\nu = 7.5\,\mathrm{Hz}$. Using as discriminant the number of counts or the Kumar-Caroll index gives similar ROCs. The limit ROC for an amplifier at SQL and the one ideally expected from a counter are evaluated for an acquisition time of 2τ because we take into account that the on-off protocol introduces a 50% duty cycle. On the right: ROC curve evaluated sending to the SMPD a signal that gives a net increase in clicks rate of 3 Hz. Also in the hardware test the ROC result beyond the SQL. The blue dashed line is the ROC obtained with software injection reported for comparison.

8.3.2 Correlation analysis

In the previously described on-off protocol, we need to use the data collected at the frequency ν_{off} to make an inference on the dark count intensity at the frequency ν_{on}. The observed drifts in dark count rate may also be correlated with variations in SMPD efficiency η. Frequency dependence of the efficiency may also explain systematic differences in the dark count rate. Thus we acquired data to study the correlations between these quantities.
The measurement sequence follows the scheme shown in Figure 53 repeated in loop. The first cycle step is a 30 s-duration dark counts acquisition at frequency ν_{on}. The efficiency is then evaluated by sending for 5 s a calibrated pulse of about 2×10^3 photon/s at frequency ν_{off} and counting the corresponding clicks. These two steps are then repeated at frequency ν_{off}.
The signal used for the efficiency measurement is obtained by mixing the signal from an AWG with the constant tone of a LO. As the mixer can affect the signal power due to temperature instabilities, we spilt the signal and send a fraction of it to a SA to monitor its power (Figure 38).

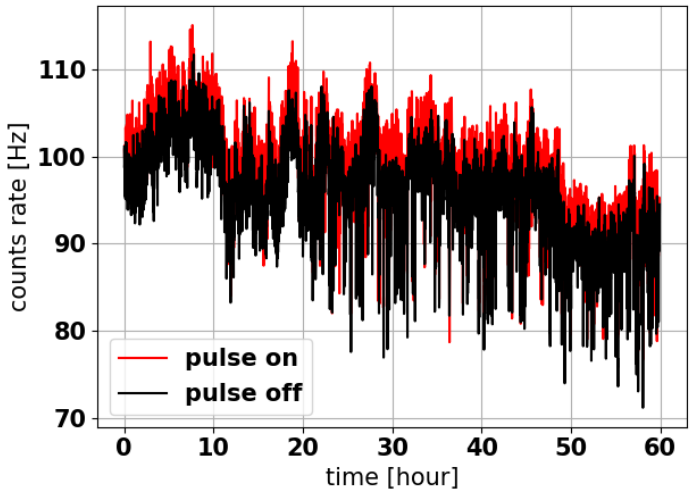

Figure 51: Clicks rate evaluated on 30 s intervals with and without hardware injected signal.

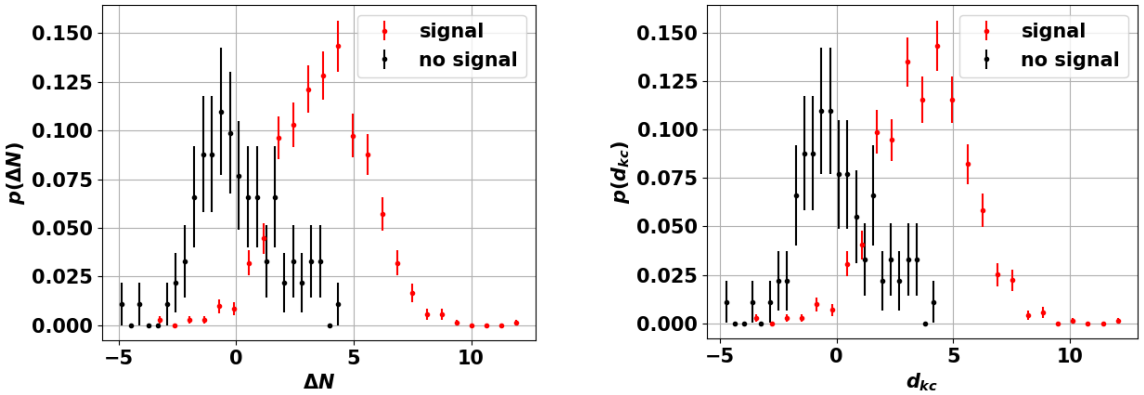

Figure 52: Distributions of ΔN and d_{kc} with and without applied signal. The distributions in presence of the signal are calculated on the sample with the hardware injected signal, the distributions in absence of the signal are calculated on the dark count sample.

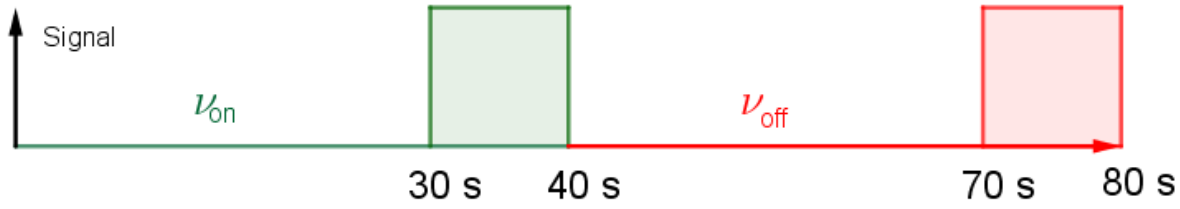

Figure 53: Measurement cycle used to study the evolution of dark count at two frequencies. Dark counts are acquired for 30 s at ν_{on}, a tone at frequency ν_{on} is applied for 10 s to the buffer line to measure the SMPD efficiency, the same measurements are performed at frequency ν_{off}. The cycle is repeated in loop.

In this test set $\nu_{\text{off}-\nu_{\text{on}}} = (7.3442 - 7.3406)\,\text{GHz} = 3.6\,\text{MHz}$. Both frequencies are detuned from the resonant frequency of the spin cavity present in the setup during of the measurement. Figure 54 shows the time series of the measured quantities. Table 10 reports the linear correlation coefficients between the measured quantities. The dark count rates at the two frequencies differ by about 15 Hz but they share common drifts. The efficiency fluctuations are instead rather similar at both frequencies. They are not correlated with drifts in dark count rate nor can they be ascribed to signal instabilities, as measured efficiency has a low correlation with the signal power monitored by the SA. The systematic difference in the efficiency measured at the two frequencies may instead be the result of the small power difference

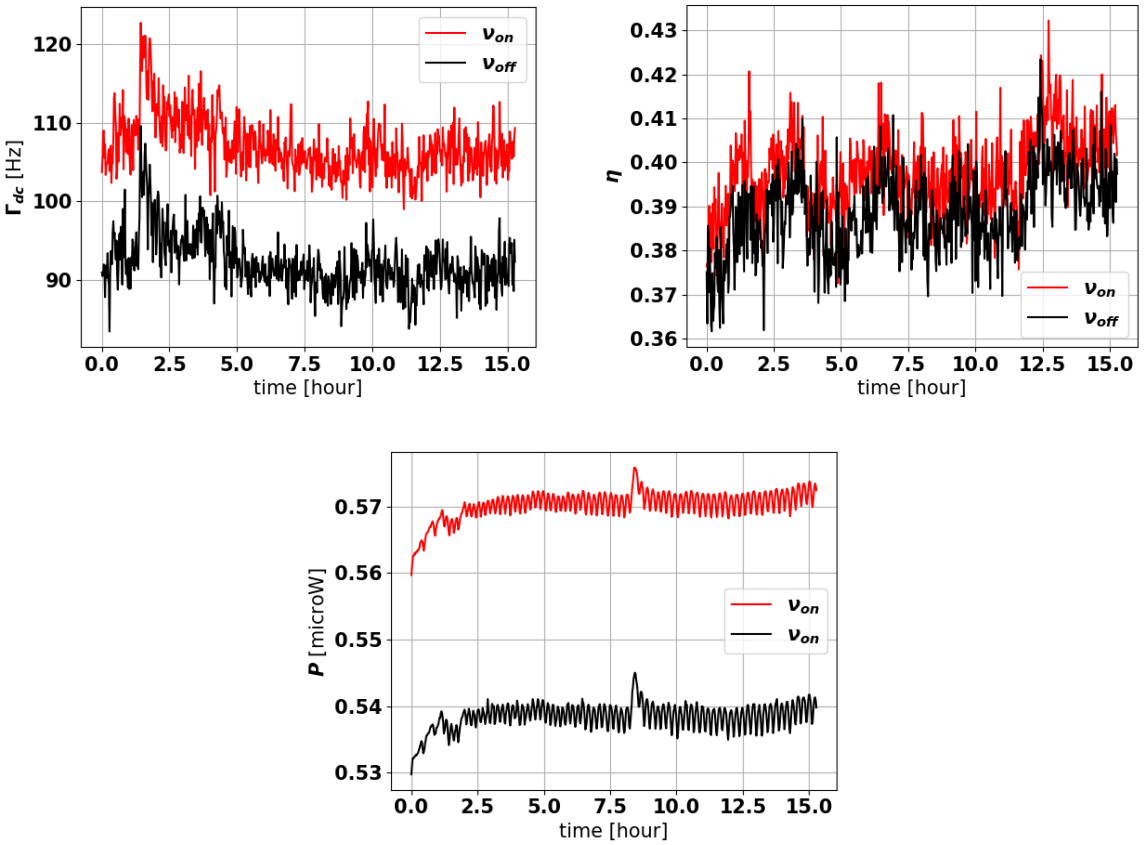

Figure 54: Evolution in time of Dark count rate $\Gamma_{\rm dc}$, efficiency η and power P measured by the SA.

between the signals used at the two frequencies, indeed the average ratio between the efficiencies is $\frac{\eta_{\rm on}}{\eta_{\rm off}} \approx 1.02$ while the one between the powers is $\frac{P_{\rm on}}{P_{\rm off}} \approx 1.05$.

Table 10: Linear correlation coefficients of the measured quantities.

	$\Gamma_{\rm dc,on}$	$\Gamma_{\rm dc,on}$	$\eta_{\rm on}$	$\eta_{\rm off}$	$P_{\rm on}$	$P_{\rm off}$
$\Gamma_{\rm dc,on}$	1					
$\Gamma_{\rm dc,on}$	0.7	1				
$\eta_{\rm on}$	0.07	0.04	1			
$\eta_{\rm off}$	0.02	0.03	0.6	1		
$P_{\rm on}$	-0.4	-0.3	0.2	0.3	1	
$P_{\rm off}$	-0.3	-0.3	0.1	0.2	0.9	1

Despite the presence of a systematic difference, the dark counts measured at $\nu_{\rm off}$ can be used to make an inference of the dark count intensity at $\nu_{\rm on}$. Indeed the fluctuations in the difference between the two rates are in a good approximation δ-correlated. Figure 55 shows the difference in dark count between the two frequencies. The spectrum of this time series is flat as expected for white noise.
The Allan variance is a statistical tool generally used to evaluate clock stability[64] that can be calculated as

$$\sigma_y^2(\tau) = \frac{1}{2}\langle(\overline{y}_{n+1} - \overline{y}_n)^2\rangle \tag{8.16}$$

where the data are divided into N samples of duration τ, $\overline{y}_n$ is the average frequency measured in the n-th sample, and $\langle\rangle$ denotes the average over all samples. For frequency white noise $\sigma_y^2(\tau) \propto \tau^{-1}$. Figure 56 (a) shows the Allan variance of the dark count rate at frequency $\nu_{\rm on}$ and the one of the difference between the two dark count rates in a log-log plot. Fitting the Allan variance of the rate difference we get a slope $m = -1.07 \pm 0.02$. Figure 56 (b) shows that of the dark count rate difference $\Gamma_{\rm dc,on} - \Gamma_{\rm dc,on}$ is as in good

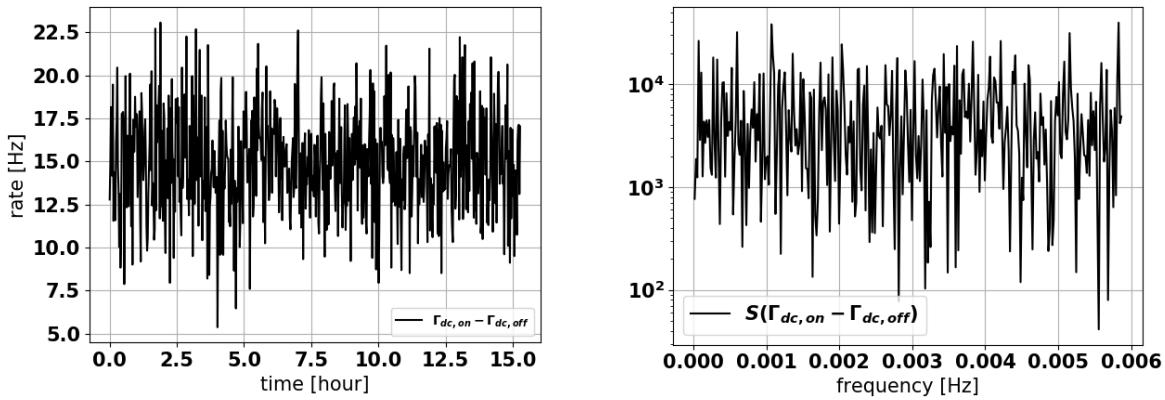

Figure 55: On the left: Dark count rate difference $\Gamma_{\mathrm{dc,on}} - \Gamma_{\mathrm{dc,on}}$. On the right: Spectrum of the dark count rate difference.

approximation a Gaussian distribution around an offset value of 15 Hz.
The strategy to deal with systematic differences will rely on the fact that for axion search data will be acquired by tuning the cavity at different frequencies to match the axion mass. If a high-Q cavity is available, some sets can be taken within the buffer bandwidth (~ 1) MHz. For instance, with a loaded quality factor $Q_L \approx 2 \times 10^5$, the cavity linewidth is bout $\Delta\nu_{\mathrm{cav}} \approx 36$ kHz and we may take about 5 measurements within a buffer linewidth. Indeed moving away by $2.5\Delta\nu_{\mathrm{cav}}$ from the buffer resonance peak reduces to about 0.992 the peak value. The variation in efficiency would then be smaller than the intrinsic fluctuations we observed (Figure 54). If any signal is present it will be measured only in one of the sets so the majority of them will be dark counts sample. We can consider at turn each of these sets as the one under test and use the others to characterize dark count rate offset $c = \Gamma_{\mathrm{dc,on}} - \Gamma_{\mathrm{dc,off}}$.

8.3.3 On-off with signal injection

We run a test to verify if we can efficiently evaluate the offset between the two darkcount rate with few measurements taken taken at different times. The sequence of acquisition for this test is the one schematized in Figure 57 repeated in loop. The (a) step is a 30 s-duration dark count acquisition at frequency ν_{on}, in the (b) step a weak signal at frequency ν_{on} is injected for 30 s. The buffer is then tuned to ν_{off}, in step (c) dark counts are acquired for 30 s, in step (d) dark counts are acquired for other 30 s at frequency ν_{off} the signal at frequency ν_{on} is injected.
The injected signal gives an average increase in count rate of 2.3 ± 0.1 Hz so the power of the signal is about $P_{sig}/h\nu \approx 5.7$ Hz. The two frequencies used in this test differ from those employed in the previous one. With these settings the offset in dark counts rate is smaller, and is of about 3 Hz. The average rate difference between the counts collected at ν_{off} in the steps (c) and (d) is 0.16 ± 0.13 Hz proving that the injected signal have no influence on the dark count rate at ν_{off}.
The detection test proceeds as follows: we start by separating the data into blocks of 5 cycles each. We have a total of these blocks $N_b = 128$. For each block, we evaluate three quantities

- $N_{\mathrm{on,dc}}$ total count number during (a) steps.
- $N_{\mathrm{on,sig}}$ total count number during (b) steps.
- $N_{\mathrm{off,dc}}$ total count number during (c) steps.

Each of these number of counts is collect in a time interval $\tau = 150$ s. The idea of the test is that each block ideally represents the result of a measurement set taken while scanning the cavity frequency within the buffer linewidth. So we create groups randomly selecting 5 blocks. There are $\binom{N_b}{5} \approx 2.6 \times 10^8$ possible combinations, in the test we create $N_g = 10^4$ groups so there is low probability of using the same group

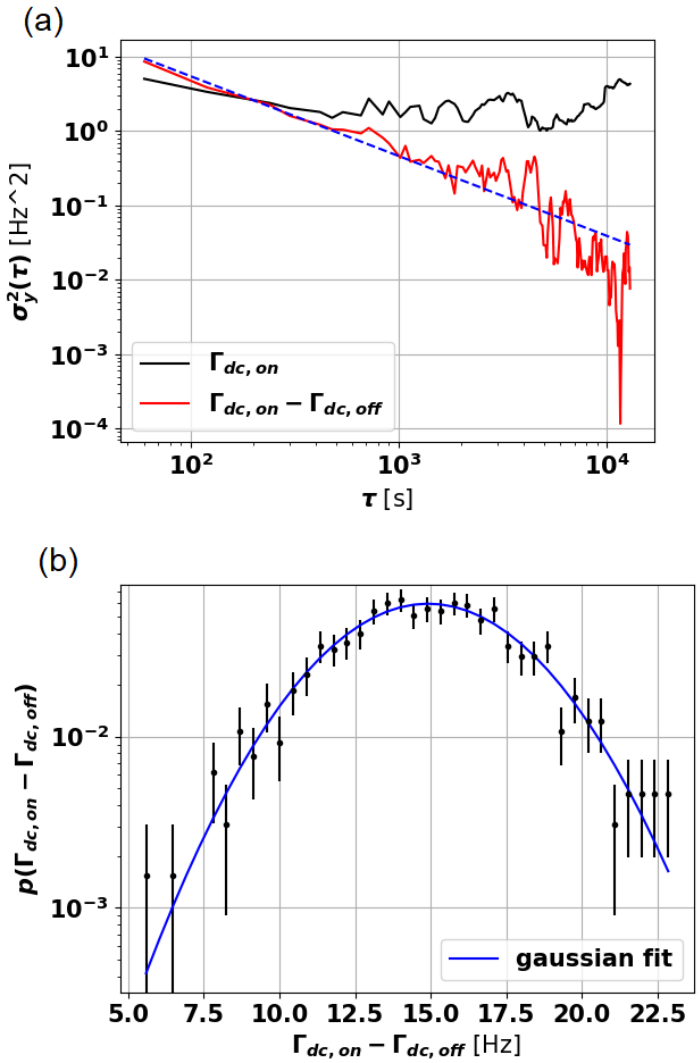

Figure 56: (a) Allan variance of the dark count rate $\Gamma_{\mathrm{dc,on}}$ and of the rate difference $\Gamma_{\mathrm{dc,on}} - \Gamma_{\mathrm{dc,off}}$. (b) Distribution of the dark count count rate difference $\Gamma_{\mathrm{dc,on}} - \Gamma_{\mathrm{dc,off}}$. The blue line is a Gaussian fit of the distribution.

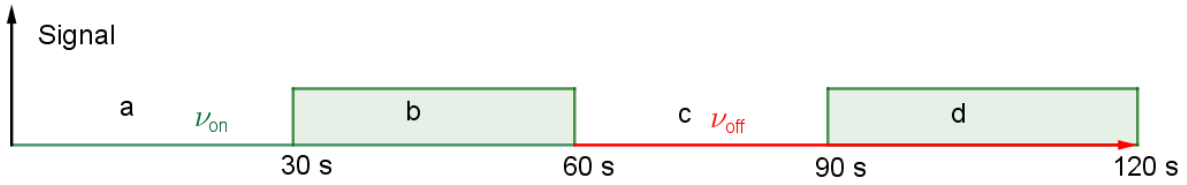

Figure 57: Acquisition sequence used for the test in **??**. Step a Dark count are acquired for 30 s at frequency ν_{on}. step b for 30 s a weak signal with frequency ν_{on} is injected in the buffer line and counts are acquired at frequency ν_{on}. Step c dark count are acquired for 30 s at frequency ν_{off}. Step d the weak signal at frequency ν_{on} is injected for 30 while the SMPD is still tuned at frequency ν_{off}. This cycle is repeated in loop.

more than one time. For each group, at turn each block is selected as the test set and the others are used as training sets. The dark count rate offset is estimated from the average rate different in the training sets

$$c = \frac{\langle N_{\mathrm{on,dc}} \rangle_{\mathrm{train}} - \langle N_{\mathrm{off,dc}} \rangle_{\mathrm{train}}}{\tau} \tag{8.17}$$

this value is then used in the test set to evaluate the rate difference used to discriminate the signal presence

$$\delta\Gamma = \frac{N^{\mathrm{test}}_{\mathrm{on,j}} - (N^{\mathrm{test}}_{\mathrm{off,dc}} + \tau c)}{\tau} \qquad j \in \{\mathrm{sig,dc}\} \tag{8.18}$$

Similarly we considered the case in which the on-off protocol is not adopted and so the the rate in the test sample is compared to the average of the train samples

$$\delta\Gamma = \frac{N^{\mathrm{test}}_{\mathrm{on,j}} - \langle N_{\mathrm{on,dc}} \rangle_{\mathrm{train}}}{\tau} \qquad j \in \{\mathrm{sig,dc}\} \tag{8.19}$$

Figure 58 shows the ROC curves evaluated in this test and the distributions of the residual rate difference $\delta\Gamma$ in the different scenarios. The ROC curve obtained applying the on-off protocol is better than the one expected for a linear amplifier at the SQL. Figure 58 compares the distributions of $\delta\Gamma$ when there is no applied signal obtained with the on-off protocol or using a single frequency. The standard deviation of the distribution is reduced by more than a factor 2. Figure 58 shows the same two distributions obtained by applying this test to the dark count data used in the correlation analysis of subsubsection 8.3.2. Remarkably, despite the wider offset, the distribution of the residual rate difference, obtained from on-off, is similar to the one obtained from the data presented in this section, showing that this is a reproducible result. In both cases, the distribution shows a deviation from a Gaussian distribution in the lower tail. From this distribution, we can see that by applying the on-off protocol for a total measurement time $2\tau = 300\,\mathrm{s}$ we may put an exclusion limit with a good confidence level for signals that gives a count rate increase higher than 5 Hz. This value is about 3 times the standard deviation of the distribution so we may compare this level to working with a SNR $\Sigma = 3$. Assuming an efficiency $\eta = 0.4$ the exclusion limit on the power of an external signal would be $P_{\mathrm{limit}}/h\nu \approx 12.5\,\mathrm{Hz}$. Comparing with the expected axion signal rate reported in Table 5 we can see that with the cavity for the pilot experiment axion signals rate is much lower than this limit, however, with a better performing cavity as the one foreseen for the QUAX haloscope this sensitivity approaches the one required to probe axion even in the more pessimistic models.

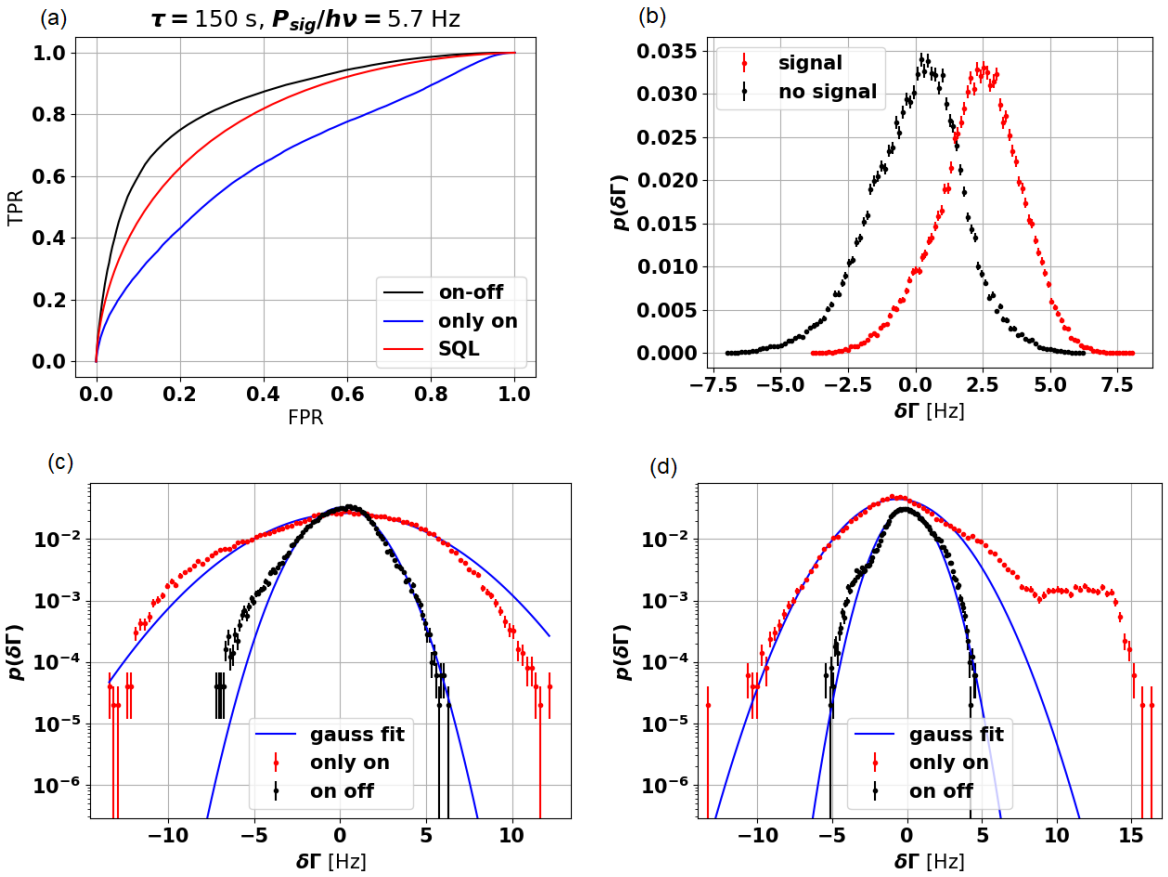

Figure 58: (a) ROC curve using on-off protocol (black), for a linear amplifier at SQL (red) and measuring only at frequency $\nu_{\rm on}$.(b) $\delta\Gamma$ distributions in presence (red) or absence (black) of the signal obtained by using the on-off protocol. (c) $\delta\Gamma$ distributions in absence of the signal evaluated with the on-off protocol (black) or using a single frequency (red). (d) $\delta\Gamma$ distribution computed from the data of the test reported in subsubsection 8.3.2.

9 Conclusions

An ideal photon counter can potentially give almost unlimited improvement to the haloscope scan rate for axion search at frequencies around 10 GHz at mK temperature. We have however to consider that real devices are affected by a dark count rate and have non unitary photodetection efficiency. The SMPD that will be employed in the pilot haloscope experiment works at 7.3 GHz, and is able to detect itinerant photons brought to the detector with a transmission line so that it can be shielded from the haloscope magnetic field. As shown in section 8 it has an approximately 100 Hz dark count rate and ∼0.4 efficiency. If the dark count process were stationary and with 100 Hz rate, these values would give about a factor 10 scan rate speed-up with respect to a linear amplifier at the SQL.

However, the experimental study described in this thesis shows that dark count rate drifts, increasing uncertainties in the average dark counts value. To deal with these drifts we devised an on-off protocol consisting of a frequent switch of the SMPD frequency between the one of interest $\nu_{\rm on}$ and a reference one $\nu_{\rm off}$ far from the cavity resonant frequency, and comparing the two counts rate. The tests have shown that the dark counts measured when the SMPD is tuned at the two different frequencies have different distributions. However, a good correlation between the two processes makes our protocol effective in removing long-term drifts. Indeed, the dark count rate difference between the two frequencies shows, in a good approximation, fluctuations from random white noise.

To characterize the remaining systematic dark counts offset we rely on data taken while scanning the cavity resonance frequency to match the axion mass. To implement this strategy it is crucial to have a narrow-linewidth cavity so that several sets can be taken within one buffer linewidth without changing the two working frequencies $\nu_{\rm on}$ and $\nu_{\rm off}$. Thanks to the high quality factor for the NbTi cavity under a 3 T, shown by the measurements reported in subsection 3.4, we could be able to take measurements at about 5 different cavity tuning steps within a buffer linewidth without significant changes in the detection efficiency. A test that mimics this strategy has shown that when comparing groups of 5 sets of measurements each taken over a total measurement time $2\tau = 300$ s the on-off protocol leads to a reduction of more than a factor 2 in the uncertainty on the estimation of dark rate compared to measurements that employ only a single working frequency.

The tuning of the resonant cavity frequency will be achieved with the insertion of three sapphire rods into the cavity that might impact the system thermal stability. In fact, non ideal thermalization of the rods could source unwanted blackbody photons in the cavity, and in addition the cryogenic motor can introduce heat in the system. The investigation of these possible thermal effects will be crucial in the pilot experiment.

In haloscope experiments signals can be injected in the cavity to test the detection efficiency[46]. In this thesis a hardware injection test has been presented showing an improvement in the detector ROC curve over the one expected for linear amplification at SQL. This could also be tested during the pilot experiment. The injection of a small signal on the buffer line gives an increment in the count rate when its frequency detuned from the cavity resonance, when the cavity frequency matches that of the injected signal we expect that the rate deceases due to absorption. Thus we can try to identify the signal as a count deficit while changing the cavity frequency.

If conditions to apply the on-off protocol holds, it will be possible to set a limit on the axion-photon coupling $g_{a\gamma\gamma}$. The preliminary test descibed in subsubsection 8.3.3 has shown that with an integration time $\tau = 150$ s corresponding to a total measurement time $2\tau = 300$ s we would have sensitivity to signals with a power higher than $P_{\rm sig}/h\nu \approx 13$ Hz. For the parameters of the NbTi cavity and the moderate field of 3 T this power is about 60 times higher than the axion signal power expected from the KSVZ model, corresponding to $g_{a\gamma\gamma} = 4 \times 10^{-12}\,\mathrm{Gev}^{-1}$.

If this SMPD is used for the readout of a cavity with a high quality factor $Q \sim Q_a \sim 10^6$ in a 14 T field as the one devised for the QUAX haloscope, then this sensitivity would allow to reach the limit of the more pessimistic DFSZ models.

The scan rate achieved by this measurement would then be

$$R_{\rm counter} \approx \frac{\nu}{Q_L 2\tau} = \frac{7\,{\rm GHz}}{2\times 10^5 \times 300\,{\rm s}} \approx 49{\rm Hz/s}. \tag{9.1}$$

For comparison, we can consider the scan rate for the same signal power achievable linear amplifier at SQL asking for an SNR $\Sigma = 3$ and for the same cavity linewidth

$$R_{\rm ampl} = \frac{Q_a}{Q_L}\left(\frac{P_{\rm sig}}{k_B T_{\rm SQL}}\right)^2 \frac{1}{\Sigma^2} \approx 2 \times \frac{(13\,{\rm Hz})^2}{9} \approx 38{\rm Hz/s} \tag{9.2}$$

From this analysis a clear advantage of the counter over a linear amplifier operated at SQL does not emerge. However, state-of-the-art broadband linear amplifiers have noise temperature about 3-4 times higher than the SQL as shown for the amplifier for the QUAX haloscope by the measurements reported in section 5. To work with high Q cavities and linear amplifiers require an absolute calibration of the noise power since the baseline power can not be inferred by exploiting the fact that the cavity resonance is much broader than the axion signal linewidth. Such an inconvenient wouldn't be encountered with a photon detector since the dark count can be characterized as we described also with high Q cavities. It is important to remark that contrary to SQL noise, the dark counts are a technical noise that can be reduced both in term of dark count rate and of long-term fluctuations with the development of the very recent technology of microwave photons counters.

Appendices

A SQL

A linear amplifier produces an output signal that depends linearly on the input, the amplifier is also phase-preserving if a phase shift of the input gives the same shift in the output. The amplifier is prepared in an operating state that is independent from the signal, so the joint system of the signal and amplifier is in a separable state. In the Heisenberg picture, the effect of a linear phase-preserving amplifier can by described as the evolution of the annihilation and creation operators from $\hat{a}$, $\hat{a}^\dagger$ before the amplification to $\hat{b}$, $\hat{b}^\dagger$ after the amplification, according to the relation [51]

$$\hat{b} = M\hat{a} + \hat{\mathcal{F}} \tag{A.1}$$

The amplifier power gain is given by $G = |M|^2$. The operator $\hat{\mathcal{F}}$ acts on the amplifier Hilbert space and therefore commutes with $\hat{a}$ and $\hat{a}^\dagger$. In general $\hat{\mathcal{F}}$ can be choose such that $\langle\hat{\mathcal{F}}\rangle = 0$ for the state of operation of the device. This operator is needed to grant that Equation A.1 describes a unitary evolution.In particular $\hat{b}$ and $\hat{b}^\dagger$ have to satisfy the commutation relation $[\hat{b}, \hat{b}^\dagger] = 1$. This requirement implies

$$1 = |M|^2 + [\mathcal{F}, \mathcal{F}^\dagger] \tag{A.2}$$

An arbitrary operator $\hat{R}$ can be written as a combination of two hermitian operators $\hat{R}_1$ and $\hat{R}_2$

$$\hat{R} = \hat{R}_1 + i\hat{R}_2 \qquad \hat{R}_1 = \frac{1}{2}(\hat{R} + \hat{R}^\dagger) \qquad \hat{R}_2 = \frac{1}{2i}(\hat{R} - \hat{R}^\dagger) \tag{A.3}$$

The Heisenberg's uncertainty principle sets a lower limit to the mean-square fluctuation of $\hat{R}$

$$\begin{aligned} \left|\Delta\hat{R}\right|^2 &\equiv \frac{1}{2}\langle\hat{R}\hat{R}^\dagger + \hat{R}^\dagger\hat{R}\rangle - \langle\hat{R}\rangle\langle\hat{R}^\dagger\rangle = \left|\Delta\hat{R}_1\right|^2 + \left|\Delta\hat{R}_2\right|^2 \\ &\geq 2\left|\Delta\hat{R}_1\right|\left|\Delta\hat{R}_2\right| \geq \left|\langle[\hat{R}_1, \hat{R}_2]\rangle\right| = \frac{1}{2}\left|\langle[\hat{R}, \hat{R}^\dagger]\rangle\right| \end{aligned} \tag{A.4}$$

After the amplification the two quadrature $\hat{X}_{1out}$ and $\hat{X}_{2out}$ are measured with heterodyne detection and summed in quadrature to compute the output power. Considering as input the vacuum state $\langle\hat{X}_{1out}\rangle = \langle\hat{X}_{2out}\rangle = 0$ and the power[5] measured in output is

$$\langle\hat{X}^2_{1out} + \hat{X}^2_{2out}\rangle = \left|\Delta\hat{X}_{1out}\right|^2 + \left|\Delta\hat{X}_{2out}\right|^2 = \left|\Delta\hat{b}\right|^2 = G|\Delta\hat{a}|^2 + \left|\Delta\hat{\mathcal{F}}\right|^2 \tag{A.5}$$

The term $\left|\Delta\hat{\mathcal{F}}\right|^2$ represents the noise power added by the amplifier. combining Equation A.2 and Equation A.4 one finds the lower limit

$$\left|\Delta\hat{\mathcal{F}}\right|^2 \geq \frac{1}{2}\left|\langle[\hat{\mathcal{F}}, \hat{\mathcal{F}}]\rangle\right| = \frac{1}{2}|1 - G| \tag{A.6}$$

So the lower limit on the measured output power is

$$\langle\hat{X}^2_{1out} + \hat{X}^2_{2out}\rangle \geq G\left(\frac{1}{2} + \frac{1}{2}\left|1 - G^{-1}\right|\right) \tag{A.7}$$

The first $\frac{1}{2}$ terms comes from the fluctuations of the signal quadrature in the vacuum state. The second term is the minimum added noise referred to the amplifier input, which means that the system is equivalent to a noiseless amplifier where the noise at the input is increased by $\left|\Delta\hat{\mathcal{F}}\right|^2/G$. Amplifiers have usually a high gain $G \gg 1$ so the limit correspond to 1/2 quanta of added noise.

[5]Here the power is given as a photon flux per unit bandwidth , the power in W is given by $P = h\nu\Delta\nu\langle\hat{X}^2_{1out} + \hat{X}^2_{2out}\rangle$

B Non linear optics

In this appendix I report the calculations needed to obtain the results of section 5. Equation 5.1 can be rewritten as

$$\frac{\partial^2 I}{\partial x^2} = L_0 C_l \frac{\partial^2 I}{\partial t^2} + \frac{L_0 C_l \epsilon}{2} \frac{\partial^2 I^2}{\partial t^2} \tag{B.1}$$

Where only the first order non linearity has been considered. Looking for a solution with the form of Equation 5.3 we can collect for instance all terms oscillating at ω_s. Considering that $\omega_s = \omega_p - \omega_i$ we find

$$\begin{aligned}
\left.\frac{\partial^2 I}{\partial x^2}\right|_{\omega_s} &= \frac{d^2 I_s}{dx^2} e^{i(k_s x - \omega_s t)} + 2ik_s \frac{dI_s}{dx} e^{i(k_s x - \omega_s t)} - k_s^2 I_s e^{i(k_s x - \omega_s t)} \\
\left.\frac{\partial^2 I}{\partial t^2}\right|_{\omega_s} &= -\omega_s^2 I_s e^{i(k_s x - \omega_s t)} \\
\left.\frac{\partial^2 I^2}{\partial t^2}\right|_{\omega_s} &= -2(\omega_p - \omega_i)^2 I_p I_i^* e^{i[(k_p - k_i)x - (\omega_p - \omega_i)t]}
\end{aligned} \tag{B.2}$$

Substituting in Equation B.1 and neglecting second order spatial derivatives for the slow variation approximation $\left|\frac{d^2 I_s}{dx^2}\right| \ll |\frac{dI_s}{dx}|$ gives

$$2ik_s \frac{dI_s}{dx} e^{i(k_s x - \omega_s t)} - k_s^2 I_s e^{i(k_s x - \omega_s t)} = -l_0 c \omega_s^2 I_s e^{i(k_s x - \omega_s t)} - l_0 c \epsilon \omega_s^2 I_p I_i^* e^{i[(k_p - k_i)x - \omega_s t]} \tag{B.3}$$

Using the dispersion relation $k_s = \sqrt{l_0(\omega_s) c(\omega_s)}\omega_s$ gives

$$\frac{dI_s}{dx} = \frac{i\epsilon k_s}{2} I_p I_i^* e^{i(k_p - k_i - k_s)x} \tag{B.4}$$

The other two relations in Equation 5.4 are similarly found.
The Manley-Rowe relation is found straightforwardly by evaluating

$$\begin{aligned}
\frac{d|I_s|^2}{dx} &= \frac{dI_s}{dx} I_s^* + I_s \frac{dI_s^*}{dx} = \frac{i\epsilon k_s}{2} e^{-i\Delta k x} I_p I_i^* I_s^* - \frac{i\epsilon k_s}{2} e^{i\Delta k x} I_p^* I_i I_s \\
\frac{d|I_i|^2}{dx} &= \frac{i\epsilon k_s}{2} e^{-i\Delta k x} I_p I_s^* I_i^* - \frac{i\epsilon k_s}{2} e^{i\Delta k x} I_p^* I_s I_i = \frac{d|I_s|^2}{dx} \\
\frac{d|I_p|^2}{dx} &= \frac{i\epsilon k_s}{2} e^{i\Delta k x} I_i I_s I_p^* - \frac{i\epsilon k_s}{2} e^{-i\Delta k x} I_i^* I_s^* I_p = -\frac{d|I_s|^2}{dx}
\end{aligned} \tag{B.5}$$

and using that $P_j \propto |I_j|^2$.
In the undepleted pump approximation, I_p is taken as a constant, and only the two equation for I_s and I_i are considered. For convenience we can use the normalization $\{I_s, I_i\} \to \{I_s/\sqrt{k_s}, I_i/\sqrt{k_i}$

$$\begin{aligned}
\frac{dI_s}{dx} &= K I_i^* e^{-i\Delta k x} \\
\frac{dI_i^*}{dx} &= K^* I_s e^{i\Delta k x}
\end{aligned} \tag{B.6}$$

where $K \equiv \frac{i\epsilon\sqrt{k_s k_i} I_p}{2}$. We can start by looking for a solution with in the form

$$
\begin{aligned}
I_s &= (Ae^{gx} + Be^{-gx})e^{-i\frac{\Delta k}{2}x} \\
I_i^* &= (Ce^{gx} + De^{-gx})e^{i\frac{\Delta k}{2}x}
\end{aligned}
\tag{B.7}
$$

Where $A\ B\ C\ D$ are complex constants. Substituting in the equation for I_s one finds

$$
(gAe^{gx} - gBe^{-gx})e^{-i\frac{\Delta k}{2}x} - \frac{i\Delta k}{2}(Ae^{gx} + Be^{-gx})e^{-i\frac{\Delta k}{2}x} = (KCe^{gx} + KDe^{-gx})e^{-i\frac{\Delta k}{2}x} \tag{B.8}
$$

The equality must hold separately for the terms with e^{+gx} and for the ones with e^{-gx}. This gives

$$
\begin{aligned}
\left(g - \frac{i\Delta k}{2}\right) A - KC = 0 \\
\left(g + \frac{i\Delta k}{2}\right) B + KD = 0
\end{aligned}
\tag{B.9}
$$

Similarly using the equation for I_i^* we find

$$
\begin{aligned}
-K^*A + \left(g + \frac{i\Delta k}{2}\right) C = 0 \\
-K^*B - \left(g - \frac{i\Delta k}{2}\right) D = 0
\end{aligned}
\tag{B.10}
$$

The two equations for A and C gives the system

$$
\begin{pmatrix} g - \frac{i\Delta k}{2} & -K \\ -K^* & g + \frac{i\Delta k}{2} \end{pmatrix} \begin{pmatrix} A \\ C \end{pmatrix} = \mathbf{0} \tag{B.11}
$$

The system admits non trivial solution if

$$
\begin{vmatrix} g - \frac{i\Delta k}{2} & -K \\ -K^* & g + \frac{i\Delta k}{2} \end{vmatrix} = g^2 + \frac{\Delta k^2}{4} - |K|^2 = 0 \tag{B.12}
$$

$$
g = \pm\sqrt{|K|^2 - \frac{\Delta k^2}{4}} \tag{B.13}
$$

We can limit to the positive solution since we are including in the solution both the term e^{gx} and e^{-gx}. Imposing the initial boundary conditions $I_s(0) = I_{s0}$ and $I_i(0) = 0$ we get 4 equation in the 4 unknown $A\ B\ C\ D$.

$$
\begin{aligned}
A + B &= I_{s0} \\
C + D &= 0 \\
\left(g - \frac{i\Delta k}{2}\right) A - KC &= 0 \\
\left(g + \frac{i\Delta k}{2}\right) B + KD &= 0
\end{aligned}
\tag{B.14}
$$

The solution of the system is

$$
\begin{aligned}
A &= \frac{g + \frac{i\Delta k}{2}}{2g} I_{s0} \\
B &= \frac{g - \frac{i\Delta k}{2}}{2g} I_{s0} \\
C &= \frac{K^*}{2g} I_{s0} \\
D &= -\frac{K^*}{2g} I_{s0}
\end{aligned}
\tag{B.15}
$$

So the solution of Equation B.6 is

$$
\begin{aligned}
I_s &= I_{s0} \left(\frac{g + \frac{i\Delta k}{2}}{2g} e^{gx} + \frac{g - \frac{i\Delta k}{2}}{2g} e^{-gx} \right) e^{-i\frac{i\Delta k}{2}x} \\
I_i^* &= \left(\frac{K^*}{2g} e^{gx} - \frac{K^*}{2g} e^{-gx} \right) e^{i\frac{i\Delta k}{2}x}
\end{aligned}
\tag{B.16}
$$

References

[1] F. Chadha-Day, J. Ellis, and D. J. E. Marsh, "Axion dark matter: What is it and why now?," *Science Advances*, vol. 8, no. 8, p. eabj3618, 2022.

[2] P. Sikivie, "Experimental tests of the "invisible" axion," *Phys. Rev. Lett.*, vol. 51, pp. 1415–1417, Oct 1983.

[3] G. T. Graham Batey, *Principles of dilution refrigeration.* Oxford Instruments NanoScience, 2015.

[4] C. Hagmann, P. Sikivie, N. S. Sullivan, and D. B. Tanner, "Results from a search for cosmic axions," *Phys. Rev. D*, vol. 42, pp. 1297–1300, Aug 1990.

[5] C. Hagmann, D. Kinion, W. Stoeffl, K. van Bibber, E. Daw, H. Peng, L. J. Rosenberg, J. LaVeigne, P. Sikivie, N. S. Sullivan, D. B. Tanner, F. Nezrick, M. S. Turner, D. of Astronomy Astrophysics, T. U. o. C. C. I. .-. Physics, Enrico Fermi Institute, D. M. Moltz, J. Powell, and N. A. Golubev, "Results from a high-sensitivity search for cosmic axions," *Physical Review Letters*, vol. 80, 3 1998.

[6] B. M. Brubaker, *First results from the HAYSTAC axion search.* PhD thesis, Yale University, 2017.

[7] Y. K. Semertzidis, J. E. Kim, S. W. Youn, J. Choi, W. Chung, S. Haciomeroglu, D.-H. Kim, J. Kim, B. R. Ko, O. Kwon, A. Matlashov, L. Miceli, H. Natori, S. Park, M. J. Lee, S. Lee, E. Sala, Y. Shin, T. Seong, S. Uchaykin, D. Ahn, S. Ahn, S. Chang, W. Cheong, H. Jeong, J. R. Joeng, D. O. Kim, J. Kim, O. Kim, Y. geun Kim, Çağlar Kutlu, D. Lee, Z. Omarov, C. K. Sung, B. Yeo, A. Yi, and M. Yıldız, "Axion dark matter research with ibs/capp," *arXiv: Instrumentation and Detectors*, 2019.

[8] C. Braggio, G. Cappelli, G. Carugno, N. Crescini, R. Di Vora, M. Esposito, A. Ortolan, L. Planat, A. Ranadive, N. Roch, *et al.*, "An haloscope amplification chain based on a travelling wave parametric amplifier," *arXiv preprint arXiv:2205.02053*, 2022.

[9] K.-S. Isleif, "The Any Light Particle Search experiment at DESY," 2 2022.

[10] R. Barbieri, C. Braggio, G. Carugno, C. Gallo, A. Lombardi, A. Ortolan, R. Pengo, G. Ruoso, and C. Speake, "Searching for galactic axions through magnetized media: The QUAX proposal," *Physics of the Dark Universe*, vol. 15, pp. 135–141, mar 2017.

[11] D. Budker, P. W. Graham, M. Ledbetter, S. Rajendran, and A. O. Sushkov, "Proposal for a cosmic axion spin precession experiment (casper)," *Phys. Rev. X*, vol. 4, p. 021030, May 2014.

[12] Y. K. Semertzidis and S. Youn, "Axion dark matter: How to see it?," *Science Advances*, vol. 8, no. 8, p. eabm9928, 2022.

[13] M. Malnou, D. A. Palken, B. M. Brubaker, L. R. Vale, G. C. Hilton, and K. W. Lehnert, "Squeezed vacuum used to accelerate the search for a weak classical signal," *Physical Review X*, 2019.

[14] S. Lamoreaux, K. Van Bibber, K. Lehnert, and G. Carosi, "Analysis of single-photon and linear amplifier detectors for microwave cavity dark matter axion searches," *Physical Review D*, vol. 88, no. 3, p. 035020, 2013.

[15] C. L. Degen, F. Reinhard, and P. Cappellaro, "Quantum sensing," *Reviews of modern physics*, vol. 89, no. 3, p. 035002, 2017.

[16] X. Gu, A. F. Kockum, A. Miranowicz, Y.-x. Liu, and F. Nori, "Microwave photonics with superconducting quantum circuits," *Physics Reports*, vol. 718, pp. 1–102, 2017.

[17] A. V. Dixit, S. Chakram, K. He, A. Agrawal, R. K. Naik, D. I. Schuster, and A. Chou, "Searching for dark matter with a superconducting qubit," *Physical Review Letters*, vol. 126, apr 2021.

[18] R. Lescanne, S. Deléglise, E. Albertinale, U. Réglade, T. Capelle, E. Ivanov, T. Jacqmin, Z. Leghtas, and E. Flurin, "Irreversible qubit-photon coupling for the detection of itinerant microwave photons," *Phys. Rev. X*, vol. 10, p. 021038, May 2020.

[19] H. Padamsee, *RF superconductivity: science, technology, and applications*. John Wiley & Sons, 2009.

[20] N. Kopnin, "Theory of superconductivity," *Helsinki University of Technology*, 2006.

[21] A. M. Zagoskin, *Quantum engineering: theory and design of quantum coherent structures*. Cambridge University Press, 2011.

[22] J. Eisenstein, "Superconducting elements," *Rev. Mod. Phys.*, vol. 26, pp. 277–291, Jul 1954.

[23] H. J. Muller, "The upper critical field of niobium-titanium," 1 1989.

[24] M. Göppl, A. Fragner, M. Baur, R. Bianchetti, S. Filipp, J. M. Fink, P. J. Leek, G. Puebla, L. Steffen, and A. Wallraff, "Coplanar waveguide resonators for circuit quantum electrodynamics," *Journal of Applied Physics*, vol. 104, no. 11, p. 113904, 2008.

[25] P. Krantz, M. Kjaergaard, F. Yan, T. P. Orlando, S. Gustavsson, and W. D. Oliver, "A quantum engineer's guide to superconducting qubits," *Applied Physics Reviews*, vol. 6, no. 2, p. 021318, 2019.

[26] I.-M. Svensson, *Tunable superconducting resonators*. PhD thesis, CHALMERS UNIVERSITY OF TECHNOLOGY, 2018.

[27] M. Sandberg, C. Wilson, F. Persson, G. Johansson, V. Shumeiko, T. Bauch, T. Duty, and P. Delsing, "Fast tuning of superconducting microwave cavities," in *AIP Conference Proceedings*, vol. 1074, pp. 12–21, American Institute of Physics, 2008.

[28] Ansys, "Ansys hfss."

[29] M. H. Awida, "Engineering of form factor in rotationally symmetric photonic cavities for faster axion searches," 2022.

[30] F. Caspers, "RF engineering basic concepts: S-parameters," in *CERN Accelerator School: Course on RF for Accelerators*, 1 2012.

[31] M. K. D. Han, Y. Kim, "Two port cavity q measurement using scattering parameters," *Review of Scientific Instruments*, 1996.

[32] D. Kim, J. Jeong, S. Youn, Y. Kim, and Y. K. Semertzidis, "Revisiting the detection rate for axion haloscopes," *Journal of Cosmology and Astroparticle Physics*, vol. 2020, pp. 066–066, mar 2020.

[33] A. Romanenko, A. Grassellino, A. C. Crawford, D. A. Sergatskov, and O. Melnychuk, "Ultra-high quality factors in superconducting niobium cavities in ambient magnetic fields up to 190 mG," *Applied Physics Letters*, vol. 105, p. 234103, dec 2014.

[34] S. Posen, M. Checchin, O. S. Melnychuk, T. Ring, and I. Gonin, "Measurement of high quality factor superconducting cavities in tesla-scale magnetic fields for dark matter searches," *TBD*, 1 2022.

[35] D. Ahn, O. Kwon, W. Chung, W. Jang, D. Lee, J. Lee, S. W. Youn, D. Youm, and Y. K. Semertzidis, "Maintaining high q-factor of superconducting $yba_2cu_3o_{7-x}$ microwave cavity in a high magnetic field," 2019.

[36] D. Alesini, C. Braggio, G. Carugno, N. Crescini, D. D'Agostino, D. D. Gioacchino, R. D. Vora, P. Falferi, S. Gallo, U. Gambardella, C. Gatti, G. Iannone, G. Lamanna, C. Ligi, A. Lombardi, R. Mezzena, A. Ortolan, R. Pengo, N. Pompeo, A. Rettaroli, G. Ruoso, E. Silva, C. Speake, L. Taffarello, and S. Tocci, "Galactic axions search with a superconducting resonant cavity," *Physical Review D*, vol. 99, may 2019.

[37] J. Kim, S. Youn, J. Jeong, W. Chung, O. Kwon, and Y. K. Semertzidis, "Exploiting higher-order resonant modes for axion haloscopes," *Journal of Physics G: Nuclear and Particle Physics*, vol. 47, p. 035203, feb 2020.

[38] B. T. McAllister, G. Flower, L. E. Tobar, and M. E. Tobar, "Tunable supermode dielectric resonators for axion dark-matter haloscopes," *Physical Review Applied*, vol. 9, jan 2018.

[39] M. Jones, "Microwave cavity simulation using ansys hfss," in *Microwave Cavities and Detectors for Axion Research*, pp. 1–7, Springer, 2020.

[40] Attocube, "Attocube nanopositioners."

[41] J. Krupka, K. Derzakowski, M. Tobar, J. Hartnett, and R. G. Geyer, "Complex permittivity of some ultralow loss dielectric crystals at cryogenic temperatures," *Measurement Science and Technology*, vol. 10, no. 5, p. 387, 1999.

[42] J. Carvill, "6 - engineering materials," in *Mechanical Engineer's Data Handbook* (J. Carvill, ed.), pp. 218–266, Oxford: Butterworth-Heinemann, 1993.

[43] E. Marquardt, J. Le, and R. Radebaugh, *Cryogenic Material Properties Database*, pp. 681–687. 01 2002.

[44] D. Aspnes, "Local-field effects and effective-medium theory: a microscopic perspective," *American Journal of Physics*, vol. 50, no. 8, pp. 704–709, 1982.

[45] C. Gaiser and B. Fellmuth, "Polarizability of helium, neon, and argon: New perspectives for gas metrology," *Phys. Rev. Lett.*, vol. 120, p. 123203, Mar 2018.

[46] C. Bartram, T. Braine, R. Cervantes, N. Crisosto, N. Du, G. Leum, L. Rosenberg, G. Rybka, J. Yang, D. Bowring, A. Chou, R. Khatiwada, A. Sonnenschein, W. Wester, G. Carosi, N. Woollett, L. Duffy, M. Goryachev, B. McAllister, M. Tobar, C. Boutan, M. Jones, B. LaRoque, N. Oblath, M. Taubman, J. Clarke, A. Dove, A. Eddins, S. O'Kelley, S. Nawaz, I. Siddiqi, N. Stevenson, A. Agrawal, A. Dixit, J. Gleason, S. Jois, P. Sikivie, J. Solomon, N. Sullivan, D. Tanner, E. Lentz, E. Daw, M. Perry, J. Buckley, P. Harrington, E. Henriksen, and K. M. and, "Axion dark matter experiment: Run 1b analysis details," *Physical Review D*, vol. 103, feb 2021.

[47] M. S. Turner, "Periodic signatures for the detection of cosmic axions," *Physical Review D*, vol. 42, no. 10, p. 3572, 1990.

[48] B. Brubaker, L. Zhong, S. Lamoreaux, K. Lehnert, and K. van Bibber, "Haystac axion search analysis procedure," *Physical Review D*, vol. 96, no. 12, p. 123008, 2017.

[49] Q. Yang, Y. Gao, and Z. Peng, "Quantum dual-path interferometry scheme for axion dark matter searches," *arXiv preprint arXiv:2201.08291*, 2022.

[50] D. M. Pozar, *Microwave engineering*. John wiley & sons, 2011.

[51] C. M. Caves, "Quantum limits on noise in linear amplifiers," *Phys. Rev. D*, vol. 26, pp. 1817–1839, Oct 1982.

[52] C. Guarcello, A. S. P. Komnang, C. Barone, A. Rettaroli, C. Gatti, S. Pagano, and G. Filatrella, "Josephson-based scheme for the detection of microwave photons," *Physical Review Applied*, vol. 16, nov 2021.

[53] J. Aumentado, "Superconducting parametric amplifiers: The state of the art in josephson parametric amplifiers," *IEEE Microwave magazine*, vol. 21, no. 8, pp. 45–59, 2020.

[54] A. Ranadive, M. Esposito, L. Planat, E. Bonet, C. Naud, O. Buisson, W. Guichard, and N. Roch, "Kerr reversal in josephson meta-material and traveling wave parametric amplification," *Nature communications*, vol. 13, no. 1, pp. 1–9, 2022.

[55] B. Ho Eom, P. K. Day, H. G. Leduc, and J. Zmuidzinas, "A wideband, low-noise superconducting amplifier with high dynamic range," *Nature Physics*, vol. 8, pp. 623–627, Aug. 2012.

[56] R. W. Boyd, *Nonlinear optics*. Academic press, 2020.

[57] Y. Y. Gao, M. A. Rol, S. Touzard, and C. Wang, "Practical guide for building superconducting quantum devices," *PRX Quantum*, vol. 2, no. 4, p. 040202, 2021.

[58] S. Kono, K. Koshino, Y. Tabuchi, A. Noguchi, and Y. Nakamura, "Quantum non-demolition detection of an itinerant microwave photon," *Nature Physics*, vol. 14, no. 6, pp. 546–549, 2018.

[59] M. Brune, F. Schmidt-Kaler, A. Maali, J. Dreyer, E. Hagley, J. M. Raimond, and S. Haroche, "Quantum rabi oscillation: A direct test of field quantization in a cavity," *Phys. Rev. Lett.*, vol. 76, pp. 1800–1803, Mar 1996.

[60] E. Albertinale, L. Balembois, E. Billaud, V. Ranjan, D. Flanigan, T. Schenkel, D. Estève, D. Vion, P. Bertet, and E. Flurin, "Detecting spins by their fluorescence with a microwave photon counter," *Nature*, vol. 600, pp. 434–438, 12 2021.

[61] QuantumMachines, "Quantum machines."

[62] J. Gambetta, A. Blais, D. I. Schuster, A. Wallraff, L. Frunzio, J. Majer, M. H. Devoret, S. M. Girvin, and R. J. Schoelkopf, "Qubit-photon interactions in a cavity: Measurement-induced dephasing and number splitting," *Physical Review A*, vol. 74, no. 4, p. 042318, 2006.

[63] S. P. A. Papoulis, *Probability, random Variables and stochastic processes.*

[64] D. W. Allan, "Statistics of atomic frequency standards," *Proceedings of the IEEE*, vol. 54, no. 2, pp. 221–230, 1966.